DUVAR

2025

INNOVATIVE PERSPECTIVES IN ENGINEERING SCIENCES

Editors
Prof. Dr. Arif UZUN
Assoc. Prof. Dr. İbrahim KARTERİ

INNOVATIVE PERSPECTIVES IN ENGINEERING SCIENCES

Editors

Prof. Dr. Arif UZUN

Assoc. Prof. Dr. İbrahim KARTERİ

Innovative Perspectives In Engineering Sciences
Editors: Prof. Dr. Arif UZUN, Assoc. Prof. Dr. İbrahim KARTERİ

Editor in chief: Berkan Balpetek
Cover and Page Design: Duvar Design
Printing: November-2025
Publisher Certificate No: 49837
ISBN: 978-625-8734-23-2

853 Sokak No:13 P.10 Kemeraltı-Konak/İzmir
Tel: 0 232 484 88 68
www.duvaryayinlari.com
duvarkitabevi@gmail.com

TABLE OF CONTENTS

Chapter 1

GEOPOLYMER FOAM CONCRETE COMPONENTS AND THEIR IMPACT ON SUSTAINABILITY: A LITERATURE REVIEW

Selçuk MEMİŞ[1], Hasbi YAPRAK[2], Emre KIVANÇ[3]

ABSTRACT

This study examines geopolymer foam concrete, one of the alternative binding systems in the construction industry, within the framework of sustainability. Based on a literature review, the use of fly ash, blast furnace slag, silica fume, bottom ash, and various industrial wastes as geopolymer binders was evaluated. Furthermore, different combinations of alkali activators, foaming agents, and aggregates were considered, and key engineering properties such as compressive strength, density, and thermal conductivity were discussed. The findings indicate that geopolymer foam concrete offers both environmental benefits (low embodied energy, carbon emission reduction, waste management) and technical advantages (thermal insulation, light weight, structural strength). However, research on the material's performance in various climatic and application conditions is limited. The study emphasizes that geopolymer foam concrete should be considered not only from a technical but also from an economic and social sustainability perspective and offers policy recommendations for the sector.

Keywords: Sustainability, Geopolymer Concrete, Foam Concrete, Embodied Energy, Industrial Waste

[1]Assoc. Prof. Dr..; Kastamonu University, Faculty of Engineering and Architecture, Email: smemis@kastamonu.edu.tr , ORCID: 0000-0002-2588-9227
[2]Prof. Dr.; Kastamonu University, Faculty of Engineering and Architecture, Email:hyaprak@kastamonu.edu.tr, ORCID: 0000-0003-1700-430X
[3]PhD; Kastamonu University, Graduate Education Institute, Department of Materials Science and Engineering, Email: emre_kivanc71@hotmail.com, ORCID: 0000-0002-9403-7802

1. INTRODUCTION

Sustainability is a multidimensional concept with environmental, economic and social dimensions that is intensely discussed both in academic circles and in industry today [1]. In general terms, it can be defined as the ability of individuals and institutions to meet today's needs without jeopardizing the needs of future generations by protecting natural resources. In this respect, sustainability is not merely an environmental concern; it is a holistic approach that addresses social justice, economic balance, and ecological stability. However, a review of the literature reveals significant differences between the practical implications of these three (Figure 1) components [2].

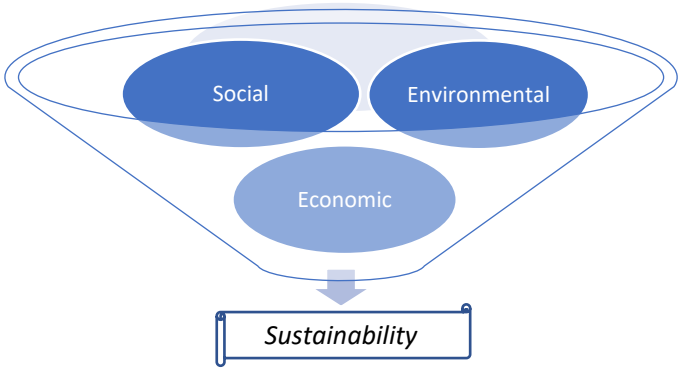

Figure 1. Three components of sustainability

While environmental awareness and practices are increasing, social sustainability is often overlooked due to conceptual ambiguities and lack of measurability [3], while economic sustainability is often limited to short-term growth targets. However, sustainable development requires the simultaneous achievement of social welfare, economic stability, and environmental protection. From this perspective, social sustainability aims to ensure the unhindered existence of individuals in terms of health, equality, and quality of life [4], [5], while economic sustainability is based on resource efficiency and long-term planning in production and consumption processes. Environmental sustainability, on the other hand, focuses on the protection of natural resources, the continuity of ecosystems, and the recycling of waste.

Environmental sustainability and low-carbon policies have become increasingly important, particularly from the construction sector's perspective. Reusing industrial waste and reducing energy consumption in production processes are key criteria for determining the environmental performance of building materials. The total energy consumed by building materials throughout

their life cycle is expressed as "embodied energy" (Figure 2), and considering this parameter is crucial in sustainability assessments. In other words, assessing the environmental impact of building materials requires considering not only the usage process but also the total amount of energy consumed throughout their life cycle. Furthermore, the total energy consumed throughout the entire process, from the initial extraction of a material to its recycling or disposal, is also considered within the concept of sustainability [6].

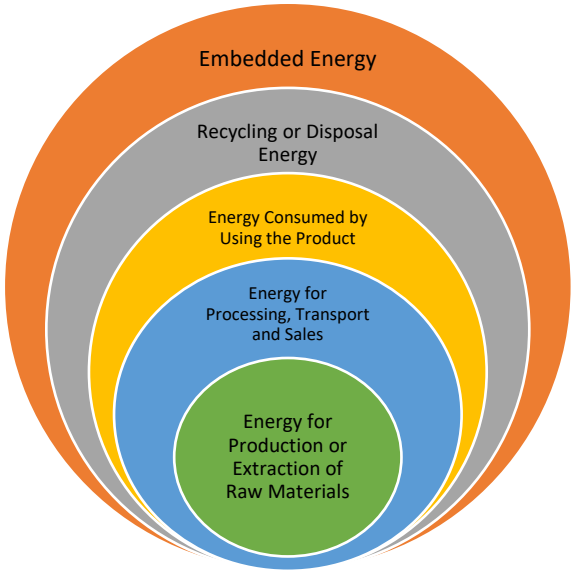

Figure 1. Embodied energy, which encompasses all energy from the extraction of raw materials to their recycling or disposal

This process, which includes steps such as raw material mining, transportation, production, processing, installation, maintenance, and disposal, poses sustainability challenges for materials that may initially appear to have low energy consumption, but may actually have high embodied energy due to the high energy consumed in their production processes. This necessitates a focus on the entire life cycle, not just end-use performance, when assessing the environmental impact of building materials.

Commonly used materials in the construction industry, such as concrete, steel, and aluminum, have high embodied energy values. The production of these materials consumes a significant amount of energy, thereby increasing their carbon footprint. Therefore, achieving sustainability goals in building materials necessitates the development of low-embodied energy alternatives. In this respect, geopolymer concretes stand out as potential materials with lower

embodied energy as an alternative to traditional Portland cement. This is primarily because these types of binding systems can be produced using industrial waste and consume significantly less energy than traditional cement production processes.

The use of geopolymer binders, derived from the alkali activation of industrial byproducts (e.g., fly ash and blast furnace slag), instead of Portland cement, which requires high energy and carbon emissions compared to traditional materials, offers a significant environmental and economic advantage. Geopolymer foam concretes, in particular, have emerged as innovative systems in the field of sustainable building materials thanks to their low density, high insulation capacity, and waste-based production capabilities. Therefore, based on data obtained in the literature, geopolymer foam concrete technologies are considered an environmentally friendly building material alternative that simultaneously supports the three key components of sustainability, has low embodied energy, and is considered an environmentally friendly alternative.

In this study, focusing on the application areas of the sustainability concept in engineering disciplines, geopolymer foam concrete technology developed in the context of building materials was examined; the potential of environmental impact reduction, industrial waste utilization and alternative binding systems in terms of sustainability were discussed.

2. SUSTAINABILITY IN ENGINEERING

Engineering is one of the most profound and transformative professions in human history. All of the infrastructure systems, technological devices, and structures we possess today have been developed thanks to engineering knowledge. However, over time, these developments have had to be evaluated alongside their environmental impacts; global challenges such as climate change, energy consumption, and resource depletion, in particular, have made the principle of sustainability essential in engineering practice. When engineering practices are examined within this context, it becomes clear that sustainability is viewed not only from an environmental perspective but also as an integral part of engineering designs, and institutions are developing various strategies to minimize the environmental impacts of their engineering activities [7]. Sustainability is an approach in engineering practices that operates in accordance with the principles of preserving the ecological balance, optimizing resource use, and generating social benefit throughout the design, production, operation, and usage processes. This understanding has manifested itself in many engineering fields, and its inclusion within the concept of sustainability

has become inevitable in various forms, such as developing online solutions to reduce physical material consumption in computer and software engineering, leading to reduced paper consumption [8], [9] or developing electric vehicles to reduce CO_2 emissions in mechanical and automotive engineering [10]. These and similar engineering examples demonstrate that sustainability has become a key engineering design criterion. However, this transformation is not limited to technology development; it also encompasses areas such as material selection, energy efficiency, and life cycle assessment.

2.1. Sustainability in Civil Engineering

Civil engineering is one of the most critical areas for implementing sustainability principles in terms of natural resource use and environmental impact. The construction sector is responsible for approximately 36% of global energy consumption and 39% of carbon emissions [11]. Therefore, every decision made in civil engineering, including design, material selection, and application methods, directly impacts sustainability.

2.1.1. Material-Based Impact

A significant portion of the environmental impact of buildings stems from the production processes of the building materials used. Traditional binding materials, such as Portland cement, steel, and aluminum, in particular, have high embodied energy values. The fossil fuels used in the production processes of these materials are a major source of greenhouse gas emissions [12]. In this regard, one of the primary goals of sustainable construction practices has been to choose renewable, local, and low-energy materials. Furthermore, utilizing waste materials as secondary raw materials both reduces environmental impacts and offers economic advantages.

2.1.2. Life Cycle Approach

In modern civil engineering, sustainability is no longer just about building "green buildings"; it is a process that must consider the entire life cycle of a building, from its design to its demolition. Throughout this process:

- Material transportation distances,
- Amount of waste generated during construction,
- Energy consumption performance of the building,
- Frequency of maintenance and repair,
- Recyclability potential,

Determine the total environmental footprint of buildings. Therefore, life cycle analyses and carbon footprint calculations have become integral parts of the sustainable design process [13].

2.1.3. Alternative Material Technologies

In sustainable civil engineering applications, geopolymer binder systems (Figure 3) are emerging as a prominent alternative to cement-based materials. These materials, derived from industrial wastes such as fly ash, blast furnace slag, and silica fume, both reduce carbon emissions and contribute to waste management. Furthermore, the advanced engineering properties of geopolymer materials, such as thermal insulation, fire resistance, and durability, make these systems not only environmentally but also structurally sustainable [14].

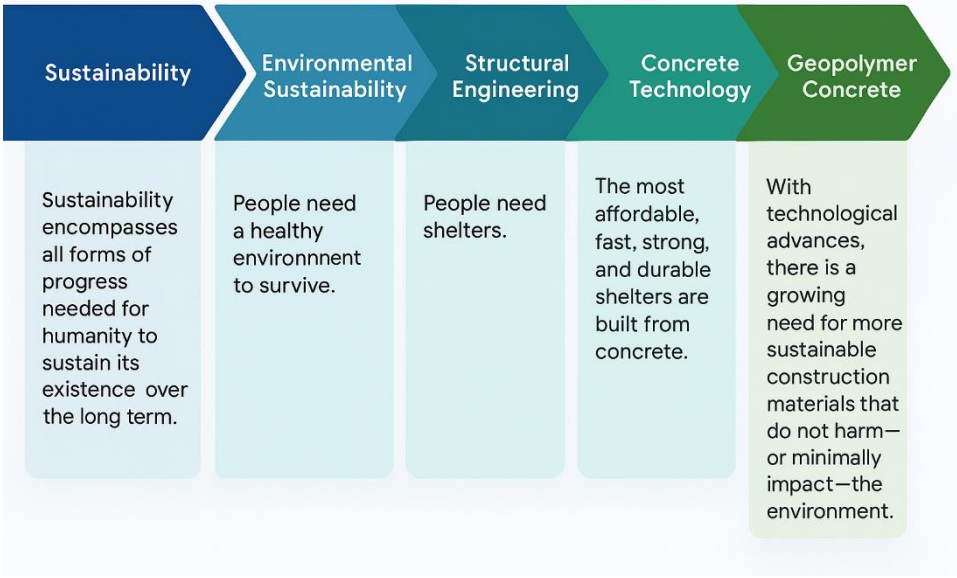

Figure 2. From sustainability to geopolymer concrete technology, what people need and what is done.

2.2. Binding Materials in the Context of Sustainability in Civil Engineering

Initially, three-dimensional silico-aluminate structures with amorphous or semi-crystalline structures were called "geopolymers" of the poly(sialate) or poly(sialate-siloxo) type [15]. The prefix "geo" here refers to materials of geological or industrial origin, such as fly ash and blast furnace slag, while the suffix "polymer" represents a molecular chain composed of the same unit [16]. With this definition, the concept of geopolymer emerged.

As mentioned above, geopolymer concrete is an important method for both reducing CO_2 emissions from Portland cement and enabling the utilization of industrial byproducts as binding materials. In such systems, aluminosilicate-based binding materials, such as fly ash or blast furnace slag, react with alkaline activators such as potassium hydroxide, sodium hydroxide, or water-soluble sodium silicate/carbonates to polymerize, thus creating an alternative binding system [17].

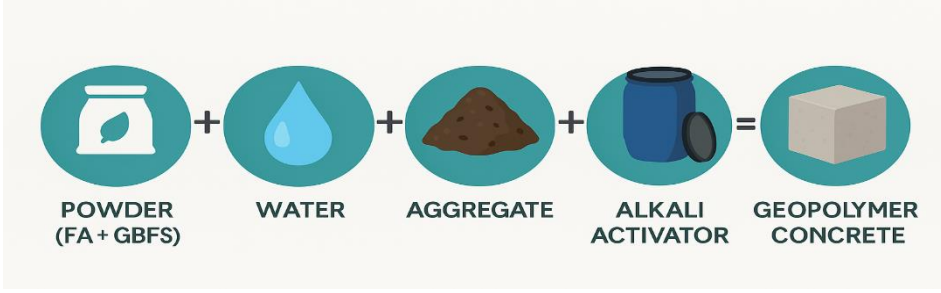

Figure 3. Geopolymer concrete production process

Geopolymer concretes, formed through polymerization, stand out as a sustainable alternative to traditional Portland cement, offering advantages such as high temperature resistance, a low carbon footprint, and the reuse of industrial waste. However, the density and thermal conductivity of these systems require further optimization, particularly in fire-resistant or insulating applications. Foam geopolymers, which reduce density by creating controlled air pockets within the matrix, have emerged as an advanced derivative of conventional geopolymer concretes. In foam geopolymer production, porosity is increased through the addition of physical or chemical foaming agents to the mixture phase, significantly reducing the material's unit weight, thus reducing thermal conductivity and maintaining specific strength. Therefore, foam geopolymers, combining low density, high insulation, and sustainable production principles, are considered potential future building materials for green building applications and lightweight structural elements requiring fire safety.

3. Geopolymer Foam Concrete

After the development of geopolymers, a more advanced solution was needed for both sustainability and the concrete industry. While geopolymer concrete was a good alternative to traditional Portland cement, it was not a sufficient insulation material. Therefore, researchers added another ingredient to the concrete paste: foam agents.

Foam concrete was first patented in 1914, followed by 1923, but has only become widely used in the last few decades [18]. Considered a lightweight concrete, foam concrete is a cement paste or mortar-like material produced in various density ranges (1600-400 kg/m³). It is characterized by high fluidity, low unit weight, less aggregate usage, controlled low strength, and good thermal insulation properties. Foam concrete (Figure 5) is primarily produced by entrapping air voids within the foaming agent [19], [20].

Figure 4. A foam concrete cube and an example of its surface

3.1. Components of Geopolymer Foam Concrete

Geopolymer foam concrete can be said to consist of five main components (Figure 6). These are:

- Binder materials
- Aggregate
- Alkaline activator
- Foam agent
- Water

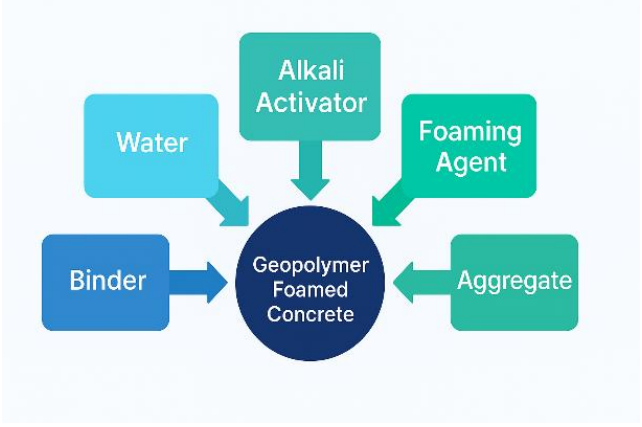

Figure 5. Main components of geopolymer foam concrete.

3.1.1. Binder Materials

In the production of geopolymer foam concrete, the binder type and ratio play a decisive role in the reaction kinetics, pore structure, and the nature of the gel phases formed. The most commonly used binders in the literature (Table 2) are classified as fly ash (FA), blast furnace slag (GGBS), metakaolin (MK), silica fume (SD), rice husk ash (RHA), palm oil ash (POFA), and cement-based hybrid systems.

In single-component systems, especially FA-based mixtures, low density (600~1200 kg/m³), low thermal conductivity (0.15~0.35 W/m.K), and limited compressive strength (1~6 MPa) are observed [21]–[23]. It has been reported that amorphous Al-Si phases are dominant in these systems, but calcium deficiency limits the formation of C-A-S-H type gels.

In geopolymer foam concretes made with the addition of slag (GGBS), the chemical structure of the binder system changed, and the geopolymerization rate and gel density increased with increasing calcium content. Thus, higher strengths in the range of 20 to 45 MPa were achieved [24]–[26]. Furthermore, binders containing GGBS were observed to have high early-age strength and low long-term shrinkage.

Metakaolin-added systems (FA/MK = 0.2~0.5) provided homogeneity in the pore structure and reached a compressive strength of approximately 16 MPa with optimum H_2O_2 [27], [28]. In hybrid binder systems (FA + POFA, FA + GGBS), thanks to the complementary silica and calcium additives of the components, density was observed in the range of 1200~1400 kg/m³, strength in the range of 6~25 MPa, and thermal conductivity in the range of 0.18~0.47 W/m.K [25], [29]–[32]. On the other hand, it has been found that slag replacement at 20~30% levels increases the strength from 7.5 MPa to 12.6 MPa, but pore stability deteriorates at higher rates [33]. The general trend shows that multi-component binders with an optimum Ca/Si ratio provide more balanced results than single-component systems in terms of both mechanical and thermal performance.

The use of these binder combinations allows the evaluation of a high proportion of industrial waste, reduces the carbon footprint with low clinker content and makes a significant contribution to sustainable material design [23]–[26], [34].

3.1.2. Alkaline Activators

Effective activation of the binder system in geopolymer foam concrete is achieved through high-pH alkaline activator solutions. The most commonly used activator systems in the literature (Table 2) are sodium hydroxide (NaOH)

and sodium silicate (Na_2SiO_3), followed by potassium hydroxide (KOH), potassium silicate (K_2SiO_3), calcium hydroxide ($Ca(OH)_2$), and sodium bicarbonate ($NaHCO_3$).

The modulus ratio (SiO_2/Na_2O) between the mixture obtained by mixing Na_2SiO_3 and NaOH components in certain proportions directly affects the structure of the geopolymer gel, the ratio of the C-A-S-H or N-A-S-H phases formed, and consequently, both mechanical and physical properties. Studies have shown that the Na_2SiO_3/NaOH ratio in the range of 1.0~2.5 provides optimum results [25], [26], [29]–[31]. At low modulus values (≤ 1.0), compressive strength decreases due to poor gel formation [35], nd at high modulus values, the viscosity of the mixture increases, negatively affecting pore stability [33].

One-part systems have also been tested in some studies; low-energy and more environmentally friendly activation strategies have been developed by dissolving solid sodium silicate with water [36], [37]. On the other hand, it has been stated that carbonate-based activators (Na_2CO_3) can be used as an alternative to classical NaOH/Na_2SiO_3 systems, and stand out with their lower alkali risk and CO_2 capture potential [34]. In addition, activator concentration is a determining parameter in the reaction rate. For example, in NaOH solutions used in the 6~14 M range, early-age strength increased as molarity increased, but mixture stability decreased with increasing heat deficit [23], [30], [31], [38]. However, it has been reported that the ratio of Na_2SiO_3:NaOH = 2:1 gives optimum results in most systems and is the most suitable combination in terms of both strength-density balance and thermal conductivity [23], [26], [33]–[35], [38].

In conclusion, the composition, molarity, and modulus of the alkali activator are the primary determinants of the microstructure and durability of geopolymer foam concrete. When used in appropriate proportions, geopolymerization efficiency increases and enables the development of sustainable binder systems with a low carbon footprint [23], [26], [33]–[35], [38].

3.1.3. Foaming Agent

Foaming agents used to achieve the porous structure in geopolymer foam concrete are among the most important components that directly determine the density, thermal conductivity, and strength properties of the material. In the literature, the foaming process (Table 2) is accomplished using two main methods: mechanical foaming and chemical foaming.

In the mechanical foaming method, air bubbles are physically trapped within the mixture using surfactants. The most commonly used agents for this purpose

are sodium dodecyl sulfate (SDS) and protein-based foams [22], [25], [32], [37], [39]–[42]. SDS directly affects the fluidity of the mixture and foam stability; The optimum dilution ratio is generally 1:60 water/solution, and the foam density varies between 40 and 100 kg/m³ [36], [37], [41]. Protein-based agents provide finer pore distribution and higher volume stability [22], [43], [44].

In the chemical foaming method, pores are generally created by gases released as a result of chemical reactions using hydrogen peroxide (H_2O_2) or aluminum powder (Al). Oxygen released by the decomposition of H_2O_2 creates homogeneous micropores within the mixture, while foaming with Al powder produces hydrogen gas, resulting in a larger porous structure [23], [26]–[28], [35]. As the H_2O_2 ratio increases, porosity increases, and density decreases accordingly; however, excessive use significantly reduces strength [26], [28].

Various stabilizers are also used to increase the stability of foams. These include calcium stearate, xanthan gum (XG), and herbal additives. These stabilizers prevent pore coalescence and improve microstructure homogeneity [28], [40], [42], [45]. Furthermore, in their study by Hajimohammadi et al. (2018), adding 0.45% xanthan gum to an SDS-modified H_2O_2 system resulted in over 30% increase in strength [40].

The foam type and ratio largely determine the final properties of geopolymer concrete. Density and strength increase at lower foam ratios, while higher foam volumes reduce thermal conductivity and improve material insulation performance [22], [26], [30], [31], [33]. Therefore, the optimum foaming strategy is determined by the type of application targeted (structural / insulation purposes).

Consequently, the type and amount of foaming agent, and the foaming method are key determinants of the microstructural homogeneity, density-strength balance, and thermal performance of geopolymer foam concrete. With appropriate selection, high-performance materials with low density and environmental sustainability can be achieved.

3.1.4. Water

As is well known, potable water must be used in concrete production. Untreated water or seawater, due to the various minerals, metals, and ions it contains, can negatively affect reactions with calcium, silicates, alkali activators, and even water itself.

Some geopolymer binder types (e.g. silica füme) require more water to ensure adequate workability. Therefore, some researchers have opted for water-reducing admixtures. Water-related admixtures are summarized in Table 1.

Table 1 – Water content and hydraulic property modifiers selected by researchers.

Contribution Type	Purpose of Use	References
Polycarboxylic ether based superplasticizer	To increase workability in mortars	[25], [30], [31], [46]
Naphthalene based superplasticizer	To increase workability	[43]
Water reducing additive (hydraulic property modifier)	Reducing the water requirement of the mortar	[47]

4. Some Studies on Geopolymer Foam Concrete

The primary mechanical properties targeted in concrete production are compressive strength and, in some cases, flexural strength and durability. High compressive strength increases the load-bearing capacity of structural elements, while good flexural strength provides ductility to the material, preventing sudden fractures. Therefore, researchers are conducting studies to optimize these mechanical properties of concrete.

Geopolymer foam concretes, unlike traditional concretes, are evaluated not only in terms of mechanical performance but also in terms of two important parameters such as thermal conductivity and density:

- **Thermal conductivity coefficient:** Low density and low material weight give geopolymer foam concrete good thermal insulation properties, making it suitable for insulating purposes.
- **Density:** Air voids created within the material during the foaming process reduce its unit weight, resulting in lower density. Thus, the same weight of material can occupy a larger volume.

Compressive strength in geopolymer foam concrete depends on the interaction of binder type, activator ratio, pore structure, aggregate characteristics, foaming method, admixtures, and curing conditions. Strength values reported in the literature range from 0.3 to 45 MPa, and this wide range is related to the material's microstructural density, degree of geopolymerization, and porosity [21], [22], [50]–[53], [25]–[29], [31], [48], [49].

Binder composition is the main determinant of strength. In systems containing only fly ash (FA) due to low reactivity, strengths remained in the range of 1~6 MPa [21]–[23], while 10~25 MPa levels were reached with the development of C-A-S-H type phases thanks to hybrid mixtures containing GGBS or MK [25], [27]–[29]. Increasing the slag ratio increased the reaction rate and binder density; in the studies

conducted by Pham et al. (2020), Pasupathy et al. (2020) and Xu et al. (2018), the 28-day strength increased to the range of 20~45 MPa. However, at slag ratios above 40%, pore stability decreased and strength decreased [33].

The alkali activator ratio also directly affects reactivity. Studies by Su et al. (2022) and Xu et al. (2018) indicated that the Na_2SiO_3/NaOH ratio in the range of 1.5~2.5 yielded optimum results, while microvoids increased with increasing viscosity at higher modulus ratios. In the study by Xu et al. (2018), a strength of 44.8 MPa was achieved under a H_2O_2 ratio of 2~3.5%, and the density-strength relationship was reported as $R^2 \approx 0.99$.

As the foaming rate increases, porosity increases, resulting in a significant decrease in strength. Studies by Liu et al. (2014), Liu et al. (2016), and Zhang et al. (2015) have reported that an increase in foam volume reduces strength by 50-80%. However, in systems with high foam stability, strength loss is limited [40], [42].

The use of additives, fibers, and biological agents is one of the most innovative strategies for enhancing mechanical performance in geopolymer foam concrete. For example, 2% PVA fiber reinforcement increased compressive strength by 54% by inhibiting microcrack propagation [45]. It has been reported that pore connectivity is reduced in composites produced using 30~40% Miscanthus × giganteus fibers and microcrack propagation is restricted despite high porosity [52]. It has been determined that *Sporosarcina pasteurii* and *Rhizopus oligosporus* microorganisms fill the micro-voids between the binder phases by promoting calcite ($CaCO_3$) precipitation and increase the strength by over 40%. [27], [54]. This biomineralization process improved microstructure integrity thanks to calcium carbonate bridges.

In the new generation single component systems (FA + GBFS + solid Na_2SiO_3), 17.5 MPa strength was achieved under room temperature curing conditions and the density remained constant at 978 kg/m³ [53]. In these systems, the binder-filler interaction is strong and offers high potential for sustainable production. Generally, optimum strength conditions are achieved within the following limits:

- Binder: FA + GGBS (%20~40 slag ratio)
- Activator: Na_2SiO_3/NaOH = 2,0~2,5 ve 6~12 M NaOH
- Foam ratio: %1~2 H_2O_2 or balanced SDS
- Density: 1.000~1.400 kg/m³

Systems designed with these parameters have a compressive strength of 20~45 MPa, high microstructure integrity and a low carbon footprint, thus achieving both structural adequacy and sustainability goals.

Table 2 – Some studies on foam studies and their defining characteristics.

Binder Type	Alkaline Activators	Foam agent	Aggregate / Filling Material	Compressive Strength (MPa)	Density (kg/m³)	Thermal Conductivity (W/m.K)	References
CEM II 42,5R + FA	—	Protein-based foaming agent	GGBS + Sand	1,00 – 1,62	926 – 1.132	0,208 – 0,264	[44]
HBSC + FA	—	Vegetable protein based agent	Dust materials	0,38 – 0,51	273 – 298	0,068 – 0,084	[43]
OPC + FA	—	H_2O_2	Desert sand + Diatomite	4,79 – 14,53	806 – 1.202	0,08 – 0,22	[47]
OPC + FA + ST-AOD GGBS	—	Protein-based foaming agent	—	1,8 – 3,3	573 – 579	—	[55]
PC + FA + SF	—	H_2O_2	—	0,47	154,7	0,0514	[46]
FA	Na_2CO_3 + Na_2SiO_3	Air trapping by mechanical mixing	—	5 – 30	1.150 – 1.850	0,30 – 0,35	[34]
GGBS	$Ca(OH)_2$, activator	Protein-based foaming agent	—	0 – 5,2	—	—	[56]
FA + Paval (Al waste)	K_2SiO_3 + KOH	Al waste	—	3.07 – 14.8	916 –1.610	—	[57]
GGBS	Na_2CO_3	Al powder	quartz sand	2,424 – 3,27	538 – 455	0,093 – 0,082	[58]
FA + GGBS	Na_2SiO_3	SDS	Fine sand + recycled glass powder	1,5 – 70	600 – 1.200	0,15 – 1,11	[36]
FA + GGBS	Na_2SiO_3	—	Cenosphere	17,5	978	0,28	[53]
FA + MK	Na_2SiO_3	Al powder	GGBS aggregate	0,9 – 16,2	600 – 1.200	0,49 – 1,22	[27]
FA	Na_2SiO_3	Foaming by microwave heating	—	0.30 - 2.45	270 – 670	0,10 – 0,25	[59]
FA + GGBS	Na_2SiO_3	SDS	Fine silica sand + RHA	1,25 – 1,79	820 – 840	0,27 – 0,36	[41]
FA + GGBS	Na_2SiO_3	Mechanical foam	Fine silica sand + PCM	1,2 – 2,4	650 – 675	—	[37]
GGBS + FA + $Ca(OH)_2$	Na_2SiO_3	SDS	—	0,27 – 0,42	410 – 330	—	[42]
FA	Na_2SiO_3 + NaOH	Protein-based foaming agent	Glass microfiber	2,9 – 9,2	900 – 1.350	0,20 – 0,32	[22]
FA	Na_2SiO_3 + NaOH	Sika Poro 40	Sand	8 – 36	700 – 1.550	—	[38]
FA	Na_2SiO_3 + H_2O	SDS	—	0,007 – 0,719	—	0,057 – 0,127	[52]
FA	Na_2SiO_3 + NaOH	H_2O_2	Silica aerogel	1,49 – 2,52	900 – 2.300	0,110 – 0,143	[21]
FA	Na_2SiO_3 + NaOH	Al powder	—	1,7 – 4,4	630 – 1.428	0,15 – 0,40	[23]

Binder Type	Alkaline Activators	Foam agent	Aggregate / Filling Material	Compressive Strength (MPa)	Density (kg/m³)	Thermal Conductivity (W/m.K)	References
FA	Na_2SiO_3 + NaOH	H_2O_2	Microsphere	1,9 – 3,4	401 – 640	0,0826 – 0,1273	[60]
FA	Na_2SiO_3 + NaOH	Al powder	—	6	400 – 800	0,145	[61]
FA + GGBS	Na_2SiO_3 + NaOH	DEWFOAM	Sand + Coarse aggregate	20 – 28	2.100 – 2.300	—	[62]
FA + GGBS	Na_2SiO_3 + NaOH	—	Natural aggregate + fine and coarse crumb rubber	15 – 56	—	—	[24]
FA + GGBS	Na_2SiO_3 + NaOH	SDS	Sand + Expanded Perlite	0,6 – 1,4	590 – 600	0,24 – 0,29	[25]
FA + GGBS	Na_2SiO_3 + NaOH	H_2O_2 + SDS	—	3,2 – 44,8	142 – 1.021	0,18 – 0,65	[26]
FA + GGBS	Na_2SiO_3 + NaOH	Surfactant	—	3 – 48	585 – 1.370	0,15 – 0,48	[33]
FA + GGBS	Na_2SiO_3 + NaOH	SDS + H_2O_2	—	1,5 – 2,4	640 – 780	0,23 – 0,27	[40]
FA + GGBS	Na_2SiO_3 + NaOH	SDS + Xanthan gum	—	—	1.713 – 1.871	—	[45]
FA + GGBS	Na_2SiO_3 + NaOH	H_2O_2	—	1,4 – 2,2	1.000 – 1.100	—	[35]
FA + GGBS + POFA	Na_2SiO_3 + NaOH	Protein-based foaming agent	River sand	27,3 – 39,0	1.689 – 1.776	—	[63]
FA + GGBS + OPC	Na_2SiO_3 + NaOH	Protein-based foaming agent	—	4,6 – 13,35	850 – 1.150	—	[64]
FA + MK	Na_2SiO_3 + NaOH	H_2O_2	EPS	2,0 – 5,5	331 – 615	0,122 – 0,195	[50]
FA + POFA	Na_2SiO_3 + NaOH	Sika AER 50/50	OPS + River sand	8,3 – 25,8	1.291 – 1.791	0,47 – 0,60	[30]
FA + POFA	Na_2SiO_3 + NaOH	Sika AER-50/50	OPS + River sand	8,3 – 72,7	1.291 – 1.840	—	[31]
FA + ZSM-5	Na_2SiO_3 + NaOH	ZSM-5	ZSM-5 waste	5,5 – 6,2	585,9 – 1.523	—	
GGBS	Na_2SiO_3 + NaOH	SDS	Quartz sand	2,6 – 3,9	470 – 730	0,18 – 0,27	[39]
GGBS + FA + CP	Na_2SiO_3 + NaOH	H_2O_2	Cenosphere	2,1 – 3,8	420 – 700	—	
MK + GGBS	Na_2SiO_3 + NaOH	H_2O_2	—	2,24 – 3,34	250 – 500	0,025 – 0,14	[49]
RHA + GGBS	Na_2SiO_3 + NaOH	H_2O_2	—	61 – 73	750 – 1.925	0,133 – 0,282	[65]
FA	Na_2SiO_3 + NaOH	—	Fine sand + glass grains	55 – 75	2,000 – 2,200	—	[66]
FA	Na_2SiO_3 + NaOH	Al powder	—	0,42 – 1,59	600 – 850	—	[67]
FA	Na_2SiO_3 + NaOH	Protein-based foaming agent	Fine aggregate + coarse aggregate	0,8 – 8,0	550 – 1.800	0,08 – 1,20	[68]
FA	Na_2SiO_3 + NaOH	—	Perlite + natural sand	0,5 – 6,5	510 – 1.070	—	[69]
FA	Na_2SiO_3 + NaOH	Al powder	Kum	0,9 – 3,9	500 – 1.900	—	[70]
FA	Na_2SiO_3 + NaOH	—	LECA + Fine sand	26,6 – 48,0	1.550 – 2.030	—	[51]
FA	Na_2SiO_3 + NaOH	H_2O_2 + Ca stearat (CSFS)	—	1,32 – 1,60	280 – 440	0,095 – 0,139	[71]

Binder Type	Alkaline Activators	Foam agent	Aggregate / Filling Material	Compressive Strength (MPa)	Density (kg/m³)	Thermal Conductivity (W/m.K)	References
FA	Na_2SiO_3 + NaOH	Al powder	—	1,4 – 2,2	566 – 940	—	[25]
FA	Na_2SiO_3 + NaOH	SDS	Fine River sand	18,8 – 55,4	1.440 – 1.690	0,133 – 0,621	[72]
FA + BA	Na_2SiO_3 + NaOH	Masterroc SLF-20	Microbial agent	16,44 – 23,53	—	—	[54]
FA + MK	Na_2SiO_3 + NaOH	H_2O_2	—	0,9 – 1,9	200 – 257	—	[28]
FA + POFA	Na_2SiO_3 + NaOH	Conplast F292	River sand	3,8 – 6,1	1.193 – 1.952	—	[29]
RHA + DFA	Na_2SiO_3 + NaOH	Chemical	—	0,5 – 1,7	644 – 718	0,131 – 0,157	
FA + GGBS	Na_2SiO_3 + NaOH + $Ca(OH)_2$	SDS	Fine sand	0,6 – 35	437– 463	—	[32]
FA	Na_2SiO_3 + NaOH + $NaHCO_3$	Active foaming agent	—	1,1 – 7,5	900 – 1.300	—	[73]
FA + SF	Na_2SiO_3 + NaOH + $NaHCO_3$	Na_2SiO_3	Lightweight aggregate waste	0,35 – 4,14	806 – 1.505	—	[74]
FA	NaOH	Al powder	—	20 – 33	1.600 – 1.750	—	[75]

5. 5. Conclusions and Recommendations

A detailed analysis of studies reported in the literature indicates that researchers are attempting to develop alternative binders for foam concrete, utilizing industrial waste for this purpose. The most common method in the search for alternative binders has been to use materials with pozzolanic properties, such as fly ash and blast furnace slag, as a partial substitute for traditional Portland cement. Some studies have also supported the search for alternative binders by using other binders, such as fly ash, bottom ash, silica fume, and palm oil ash, in conjunction with geopolymers. These findings demonstrate that geopolymer binders are an alternative to cementitious binders for the construction industry.

Geopolymer foam concrete, in particular, has demonstrated its potential in the thermal insulation sector as an alternative to traditional insulation materials such as stone wool, glass wool, and polystyrene foam, thanks to its low thermal conductivity. When examined in terms of compressive strength, geopolymer foam concrete sometimes exhibits low and sometimes high strength values. Therefore, while it can be used as a primary load-bearing concrete in some cases, it is more suitable for use in the production of lightweight structural elements. By combining both good compressive strength and effective thermal insulation, such elements can provide a sustainable alternative to traditional brick and stone wool production.

In short, changes to the binder, aggregate, and other components of geopolymer foam concrete have enabled the development of new concrete types with varying compressive strength, thermal properties, and density values. Most importantly, these studies have resulted in a sustainable building material. In conclusion, the research examined in this study demonstrates that the field of geopolymer foam concrete remains an area requiring intensive research and development.

Geopolymer foam concrete's structure, aligned with sustainability goals, offers significant opportunities both environmentally and economically. This material, which offers advantages in green building certification processes thanks to its low carbon emissions, waste recycling, and energy efficiency, has the potential to transform the construction industry when expanded across public and private projects. To ensure this transformation becomes permanent, field studies conducted under diverse climatic conditions within the framework of industry-university collaboration and increased political incentives are crucial.

REFERENCES

[1] J. L. Ramsey, "On Not Defining Sustainability," *J. Agric. Environ. Ethics*, vol. 28, no. 6, pp. 1075–1087, 2015, doi: 10.1007/s10806-015-9578-3.

[2] B. Purvis, Y. Mao, and D. Robinson, "Three pillars of sustainability: in search of conceptual origins," *Sustain. Sci.*, vol. 14, no. 3, pp. 681–695, 2019, doi: 10.1007/s11625-018-0627-5.

[3] R. H. W. Boyer, N. D. Peterson, P. Arora, and K. Caldwell, "Five approaches to social sustainability and an integratedway forward," *Sustain.*, vol. 8, no. 9, 2016, doi: 10.3390/su8090878.

[4] M. Missimer, K. H. Robèrt, and G. Broman, "A strategic approach to social sustainability - Part 2: a principle-based definition," *J. Clean. Prod.*, vol. 140, pp. 42–52, 2017, doi: 10.1016/j.jclepro.2016.04.059.

[5] M. Du and X. Zhang, "Urban greening: A new paradox of economic or social sustainability?," *Land use policy*, vol. 92, no. April 2019, p. 104487, 2020, doi: 10.1016/j.landusepol.2020.104487.

[6] R. Crawford and M. Hall, "Embodied Energy," 2020.

[7] V. Kumar *et al.*, "Infusing sustainability principles into manufacturing/mechanical engineering curricula," *J. Manuf. Syst.*, vol. 24, no. 3, pp. 215–225, 2005, doi: 10.1016/S0278-6125(06)80011-7.

[8] M. A. Villanthenkodath, M. A. Ansari, P. Kumar, and Y. N. Raju, "Effect of information and communication technology on the environmental sustainability: An empirical assessment for South Africa," *Telemat. Informatics Reports*, vol. 7, no. July, 2022, doi: 10.1016/j.teler.2022.100013.

[9] Z. Dehghan Shabani and R. Shahnazi, "Energy consumption, carbon dioxide emissions, information and communications technology, and gross domestic product in Iranian economic sectors: A panel causality analysis," *Energy*, vol. 169, pp. 1064–1078, 2019, doi: 10.1016/j.energy.2018.11.062.

[10] D. Zeng *et al.*, "Are the electric vehicles more sustainable than the conventional ones? Influences of the assumptions and modeling approaches in the case of typical cars in China," *Resour. Conserv. Recycl.*, vol. 167, no. September 2020, p. 105210, 2021, doi: 10.1016/j.resconrec.2020.105210.

[11] W. Chen, S. Yang, X. Zhang, N. D. Jordan, and J. Huang, "Embodied energy and carbon emissions of building materials in China," *Build. Environ.*, vol. 207, no. PA, p. 108434, 2022, doi: 10.1016/j.buildenv.2021.108434.

[12] S. A. Ishak and H. Hashim, “Effect of mitigation technologies on the total cost and carbon dioxide emissions of a cement plant under multi-objective mixed linear programming optimisation,” *Chem. Eng. Res. Des.*, vol. 186, pp. 326–349, 2022, doi: 10.1016/j.cherd.2022.07.048.

[13] H. Zhou *et al.*, “Towards sustainable coal industry: Turning coal bottom ash into wealth,” *Sci. Total Environ.*, vol. 804, p. 149985, 2022, doi: 10.1016/j.scitotenv.2021.149985.

[14] S. Das, P. Saha, S. Prajna Jena, and P. Panda, “Geopolymer concrete: Sustainable green concrete for reduced greenhouse gas emission – A review,” *Mater. Today Proc.*, vol. 60, pp. 62–71, 2022, doi: 10.1016/j.matpr.2021.11.588.

[15] J. Davidovits, “GEOPOLYMERS AND GEOPOLYMERIC MATERIAL$,” *J. Therm. Anal.*, vol. 35, no. 06, pp. 429–441, 1989.

[16] K. H. Younis, K. A. Salihi, and T. K. Ibrahim, “An overview of geo-polymer concrete including recycled aggregate,” *Int. J. Sci. Technol. Res.*, vol. 9, no. 3, pp. 6239–6245, 2020.

[17] B. Skariah Thomas *et al.*, “Geopolymer concrete incorporating recycled aggregates: A comprehensive review,” *Clean. Mater.*, vol. 3, no. January, p. 100056, 2022, doi: 10.1016/j.clema.2022.100056.

[18] Z. Zhang, J. L. Provis, A. Reid, and H. Wang, “Geopolymer foam concrete: An emerging material for sustainable construction,” *Constr. Build. Mater.*, vol. 56, pp. 113–127, 2014, doi: 10.1016/j.conbuildmat.2014.01.081.

[19] K. Ramamurthy, E. K. Kunhanandan Nambiar, and G. Indu Siva Ranjani, “A classification of studies on properties of foam concrete,” *Cem. Concr. Compos.*, vol. 31, no. 6, pp. 388–396, 2009, doi: 10.1016/j.cemconcomp.2009.04.006.

[20] S. N. Sarmin, “Lightweight Building Materials of Geopolymer Reinforced Wood Particles Aggregate – A Review,” *Appl. Mech. Mater.*, vol. 802, no. November, pp. 220–224, 2015, doi: 10.4028/www.scientific.net/amm.802.220.

[21] Y. X. Chen, K. M. Klima, H. J. H. Brouwers, and Q. Yu, “Effect of silica aerogel on thermal insulation and acoustic absorption of geopolymer foam composites: The role of aerogel particle size,” *Compos. Part B Eng.*, vol. 242, no. December 2021, p. 110048, 2022, doi: 10.1016/j.compositesb.2022.110048.

[22] J. Stolz, Y. Boluk, and V. Bindiganavile, “Mechanical, thermal and acoustic properties of cellular alkali activated fly ash concrete,” *Cem. Concr. Compos.*, vol. 94, no. August, pp. 24–32, 2018, doi:

10.1016/j.cemconcomp.2018.08.004.
[23] W. Wongkeo, S. Seekaew, and O. Kaewrahan, “Properties of high calcium fly ash geopolymer lightweight concrete,” in *Materials Today: Proceedings*, 2019, vol. 17, pp. 1423–1430. doi: 10.1016/j.matpr.2019.06.163.
[24] T. M. Pham *et al.*, “Dynamic compressive properties of lightweight rubberized geopolymer concrete,” *Constr. Build. Mater.*, vol. 265, p. 120753, 2020, doi: 10.1016/j.conbuildmat.2020.120753.
[25] K. Pasupathy, S. Ramakrishnan, and J. Sanjayan, “Enhancing the mechanical and thermal properties of aerated geopolymer concrete using porous lightweight aggregates,” *Constr. Build. Mater.*, vol. 264, p. 120713, 2020, doi: 10.1016/j.conbuildmat.2020.120713.
[26] F. Xu, G. Gu, W. Zhang, H. Wang, X. Huang, and J. Zhu, “Pore structure analysis and properties evaluations of fly ash-based geopolymer foams by chemical foaming method,” *Ceram. Int.*, vol. 44, no. 16, pp. 19989–19997, 2018, doi: 10.1016/j.ceramint.2018.07.267.
[27] R. Arellano Aguilar, O. Burciaga Díaz, and J. I. Escalante García, “Lightweight concretes of activated metakaolin-fly ash binders, with blast furnace slag aggregates,” *Constr. Build. Mater.*, vol. 24, no. 7, pp. 1166–1175, 2010, doi: 10.1016/j.conbuildmat.2009.12.024.
[28] J. Wu, Z. Zhang, Y. Zhang, and D. Li, “Preparation and characterization of ultra-lightweight foamed geopolymer (UFG) based on fly ash-metakaolin blends,” *Constr. Build. Mater.*, vol. 168, pp. 771–779, 2018, doi: 10.1016/j.conbuildmat.2018.02.097.
[29] A. M. Alnahhal, U. J. Alengaram, S. Yusoff, P. Darvish, K. Srinivas, and M. Sumesh, “Engineering performance of sustainable geopolymer foamed and non-foamed concretes,” *Constr. Build. Mater.*, vol. 316, no. November 2021, p. 125601, 2022, doi: 10.1016/j.conbuildmat.2021.125601.
[30] M. Y. J. Liu, U. J. Alengaram, M. Z. Jumaat, and K. H. Mo, “Evaluation of thermal conductivity, mechanical and transport properties of lightweight aggregate foamed geopolymer concrete,” *Energy Build.*, vol. 72, pp. 238–245, 2014, doi: 10.1016/j.enbuild.2013.12.029.
[31] M. Y. J. Liu, U. J. Alengaram, M. Santhanam, M. Z. Jumaat, and K. H. Mo, “Microstructural investigations of palm oil fuel ash and fly ash based binders in lightweight aggregate foamed geopolymer concrete,” *Constr. Build. Mater.*, vol. 120, pp. 112–122, 2016, doi: 10.1016/j.conbuildmat.2016.05.076.
[32] K. Dhasindrakrishna, K. Pasupathy, S. Ramakrishnan, and J. Sanjayan,

"Effect of yield stress development on the foam-stability of aerated geopolymer concrete," *Cem. Concr. Res.*, vol. 138, no. April, p. 106233, 2020, doi: 10.1016/j.cemconres.2020.106233.

[33] Z. Zhang, J. L. Provis, A. Reid, and H. Wang, "Mechanical, thermal insulation, thermal resistance and acoustic absorption properties of geopolymer foam concrete," *Cem. Concr. Compos.*, vol. 62, pp. 97–105, 2015, doi: 10.1016/j.cemconcomp.2015.03.013.

[34] H. Alghamdi and N. Neithalath, "Novel synthesis of lightweight geopolymer matrices from fly ash through carbonate-based activation," *Mater. Today Commun.*, vol. 17, no. August, pp. 266–277, 2018, doi: 10.1016/j.mtcomm.2018.09.014.

[35] L. Su, G. Fu, B. Liang, Q. Sun, and X. Zhang, "Mechanical properties and microstructure evaluation of fly ash - Slag geopolymer foaming materials," *Ceram. Int.*, vol. 48, no. 13, pp. 18224–18237, 2022, doi: 10.1016/j.ceramint.2022.03.081.

[36] A. Hajimohammadi, T. Ngo, and A. Kashani, "Sustainable one-part geopolymer foams with glass fines versus sand as aggregates," *Constr. Build. Mater.*, vol. 171, pp. 223–231, 2018, doi: 10.1016/j.conbuildmat.2018.03.120.

[37] S. Ramakrishnan, K. Pasupathy, and J. Sanjayan, "Synthesis and properties of thermally enhanced aerated geopolymer concrete using form-stable phase change composite," *J. Build. Eng.*, vol. 40, no. April, p. 102756, 2021, doi: 10.1016/j.jobe.2021.102756.

[38] P. Yoosuk, C. Suksiripattanapong, P. Sukontasukkul, and P. Chindaprasirt, "Properties of polypropylene fiber reinforced cellular lightweight high calcium fly ash geopolymer mortar," *Case Stud. Constr. Mater.*, vol. 15, no. July, p. e00730, 2021, doi: 10.1016/j.cscm.2021.e00730.

[39] A. Hajimohammadi, T. Ngo, P. Mendis, A. Kashani, and J. S. J. van Deventer, "Alkali activated slag foams: The effect of the alkali reaction on foam characteristics," *J. Clean. Prod.*, vol. 147, pp. 330–339, 2017, doi: 10.1016/j.jclepro.2017.01.134.

[40] A. Hajimohammadi, T. Ngo, and P. Mendis, "Enhancing the strength of pre-made foams for foam concrete applications," *Cem. Concr. Compos.*, vol. 87, pp. 164–171, 2018, doi: 10.1016/j.cemconcomp.2017.12.014.

[41] K. Pasupathy, S. Ramakrishnan, and J. Sanjayan, "Influence of recycled concrete aggregate on the foam stability of aerated geopolymer concrete," *Constr. Build. Mater.*, vol. 271, p. 121850, 2021, doi: 10.1016/j.conbuildmat.2020.121850.

[42] K. Dhasindrakrishna, K. Pasupathy, S. Ramakrishnan, and J. Sanjayan, "Rheology and elevated temperature performance of geopolymer foam concrete with varying PVA fibre dosage," *Mater. Lett.*, vol. 328, no. September, p. 133122, 2022, doi: 10.1016/j.matlet.2022.133122.

[43] C. Liu *et al.*, "Water-resistance properties of high-belite sulphoaluminate cement-based ultra-light foamed concrete treated with different water repellents," *Constr. Build. Mater.*, vol. 228, p. 116798, 2019, doi: 10.1016/j.conbuildmat.2019.116798.

[44] O. H. Oren, A. Gholampour, O. Gencel, and T. Ozbakkaloglu, "Physical and mechanical properties of foam concretes containing granulated blast furnace slag as fine aggregate," *Constr. Build. Mater.*, vol. 238, p. 117774, 2020, doi: 10.1016/j.conbuildmat.2019.117774.

[45] G. Gu, F. Xu, X. Huang, S. Ruan, C. Peng, and J. Lin, "Foamed geopolymer: The relationship between rheological properties of geopolymer paste and pore-formation mechanism," *J. Clean. Prod.*, vol. 277, p. 123238, 2020, doi: 10.1016/j.jclepro.2020.123238.

[46] J. Zhang, G. Pan, X. Zheng, and C. Chen, "Preparation and characterization of ultra-lightweight fly ash-based cement foams incorporating ethylene-vinyl acetate emulsion and waste-derived C-S-H seeds," *Constr. Build. Mater.*, vol. 274, p. 122027, 2021, doi: 10.1016/j.conbuildmat.2020.122027.

[47] X. Wang, W. Gao, S. Yan, M. Niu, G. Liu, and H. Hao, "Incorporation of sand-based breathing bricks with foamed concrete and humidity control materials," *Constr. Build. Mater.*, vol. 175, pp. 187–195, 2018, doi: 10.1016/j.conbuildmat.2018.04.186.

[48] K. Pasupathy, S. Ramakrishnan, and J. Sanjayan, "Enhancing the chemical foaming process using superplasticizer in aerated geopolymer concrete," *Constr. Build. Mater.*, vol. 324, no. January, p. 126535, 2022, doi: 10.1016/j.conbuildmat.2022.126535.

[49] G. Samson, M. Cyr, and X. X. Gao, "Thermomechanical performance of blended metakaolin-GGBS alkali-activated foam concrete," *Constr. Build. Mater.*, vol. 157, pp. 982–993, 2017, doi: 10.1016/j.conbuildmat.2017.09.146.

[50] J. Shi *et al.*, "Preparation and characterization of lightweight aggregate foamed geopolymer concretes aerated using hydrogen peroxide," *Constr. Build. Mater.*, vol. 256, p. 119442, 2020, doi: 10.1016/j.conbuildmat.2020.119442.

[51] M. Priyanka, M. Karthikeyan, and M. S. R. Chand, "Development of mix proportions of geopolymer lightweight aggregate concrete with LECA,"

Mater. Today Proc., vol. 27, pp. 958–962, 2020, doi: 10.1016/j.matpr.2020.01.271.

[52] K. Walbrück, L. Drewler, S. Witzleben, and D. Stephan, "Factors influencing thermal conductivity and compressive strength of natural fiber-reinforced geopolymer foams," *Open Ceram.*, vol. 5, no. January, p. 100065, 2021, doi: 10.1016/j.oceram.2021.100065.

[53] A. Hajimohammadi, T. Ngo, J. L. Provis, T. Kim, and J. Vongsvivut, "High strength/density ratio in a syntactic foam made from one-part mix geopolymer and cenospheres," *Compos. Part B Eng.*, vol. 173, no. May, p. 106908, 2019, doi: 10.1016/j.compositesb.2019.106908.

[54] K. D. Wulandari *et al.*, "Effect of microbes addition on the properties and surface morphology of fly ash-based geopolymer paste," *J. Build. Eng.*, vol. 33, no. May 2020, p. 101596, 2021, doi: 10.1016/j.jobe.2020.101596.

[55] B. Park and Y. C. Choi, "Investigation of carbon-capture property of foam concrete using stainless steel AOD slag," *J. Clean. Prod.*, vol. 288, p. 125621, 2021, doi: 10.1016/j.jclepro.2020.125621.

[56] H. Zhang *et al.*, "Statistical mixture design for carbide residue activated blast furnace slag foamed lightweight concrete," *Constr. Build. Mater.*, vol. 342, no. May, 2022, doi: 10.1016/j.conbuildmat.2022.127840.

[57] C. Leiva, Y. Luna-Galiano, C. Arenas, B. Alonso-Fariñas, and C. Fernández-Pereira, "A porous geopolymer based on aluminum-waste with acoustic properties," *Waste Manag.*, vol. 95, pp. 504–512, 2019, doi: 10.1016/j.wasman.2019.06.042.

[58] B. Yuan, C. Straub, S. Segers, Q. L. Yu, and H. J. H. Brouwers, "Sodium carbonate activated slag as cement replacement in autoclaved aerated concrete," *Ceram. Int.*, vol. 43, no. 8, pp. 6039–6047, 2017, doi: 10.1016/j.ceramint.2017.01.144.

[59] M. Rashid *et al.*, "Light weight low thermal conductive fly ash foams through microwave irradiation for insulative, agricultural and self-healing purposes," *Mater. Today Proc.*, vol. 47, pp. S38–S45, 2020, doi: 10.1016/j.matpr.2020.04.682.

[60] M. Łach, K. Korniejenko, and J. Mikuła, "Thermal Insulation and Thermally Resistant Materials Made of Geopolymer Foams," *Procedia Eng.*, vol. 151, pp. 410–416, 2016, doi: 10.1016/j.proeng.2016.07.350.

[61] P. Hlaváček, V. Šmilauer, F. Škvára, L. Kopecký, and R. Šulc, "Inorganic foams made from alkali-activated fly ash: Mechanical, chemical and physical properties," *J. Eur. Ceram. Soc.*, vol. 35, no. 2, pp. 703–709, 2015, doi: 10.1016/j.jeurceramsoc.2014.08.024.

[62] P. Mukkala, C. Venkatesh, and S. Habibunnisa, “Evaluation of mix ratios of light weight concrete using geopolymer as binder,” *Mater. Today Proc.*, vol. 52, pp. 2053–2056, 2022, doi: 10.1016/j.matpr.2021.12.140.

[63] A. M. Alnahhal, U. J. Alengaram, M. S. I. Ibrahim, S. Yusoff, H. S. C. Metselaar, and P. Gabriela Johnson, “Synthesis of ternary binders and sand-binder ratio on the mechanical and microstructural properties of geopolymer foamed concrete,” *Constr. Build. Mater.*, vol. 349, no. August, p. 128682, 2022, doi: 10.1016/j.conbuildmat.2022.128682.

[64] R. B. Kejkar and S. P. Wanjari, “Feasibility study of commercially viable sustainable aerated geopolymeric foam based block,” *Mater. Today Proc.*, vol. 45, pp. 4398–4404, 2021, doi: 10.1016/j.matpr.2020.11.916.

[65] G. Liang, T. Liu, H. Li, B. Dong, and T. Shi, “A novel synthesis of lightweight and high-strength green geopolymer foamed material by rice husk ash and ground-granulated blast-furnace slag,” *Resour. Conserv. Recycl.*, vol. 176, no. June 2021, p. 105922, 2022, doi: 10.1016/j.resconrec.2021.105922.

[66] A. Hajimohammadi, T. Ngo, and J. Vongsvivut, “Interfacial chemistry of a fly ash geopolymer and aggregates,” *J. Clean. Prod.*, vol. 231, pp. 980–989, 2019, doi: 10.1016/j.jclepro.2019.05.249.

[67] A. Hajimohammadi, T. Ngo, P. Mendis, and J. Sanjayan, “Regulating the chemical foaming reaction to control the porosity of geopolymer foams,” *Mater. Des.*, vol. 120, pp. 255–265, 2017, doi: 10.1016/j.matdes.2017.02.026.

[68] Y. Wang, T. Zheng, X. Zheng, Y. Liu, J. Darkwa, and G. Zhou, “Thermo-mechanical and moisture absorption properties of fly ash-based lightweight geopolymer concrete reinforced by polypropylene fibers,” *Constr. Build. Mater.*, vol. 251, p. 118960, 2020, doi: 10.1016/j.conbuildmat.2020.118960.

[69] M. Rezaei and V. Bindiganavile, “Alkali-activated fly ash foams for narrow-trench reinstatement,” *Cem. Concr. Compos.*, vol. 119, no. January, p. 103966, 2021, doi: 10.1016/j.cemconcomp.2021.103966.

[70] D. Wattanasiriwech, K. Yomthong, and S. Wattanasiriwech, “Characterisation and properties of class C-fly ash based geopolymer foams: Effects of foaming agent content, aggregates, and surfactant,” *Constr. Build. Mater.*, vol. 306, no. January, 2021, doi: 10.1016/j.conbuildmat.2021.124847.

[71] Y. Cui, D. Wang, J. Zhao, D. Li, S. Ng, and Y. Rui, “Effect of calcium stearate based foam stabilizer on pore characteristics and thermal conductivity of geopolymer foam material,” *J. Build. Eng.*, vol. 20, no.

June, pp. 21–29, 2018, doi: 10.1016/j.jobe.2018.06.002.

[72] P. Chindaprasirt, P. Jitsangiam, and U. Rattanasak, “Hydrophobicity and efflorescence of lightweight fly ash geopolymer incorporated with calcium stearate,” *J. Clean. Prod.*, vol. 364, no. May, p. 132449, 2022, doi: 10.1016/j.jclepro.2022.132449.

[73] F. K. Alqahtani, K. Rashid, I. Zafar, and M. Iqbal Khan, “Assessment of morphological characteristics and physico-mechanical properties of geopolymer green foam lightweight aggregate formulated by microwave irradiation,” *J. Build. Eng.*, vol. 35, no. August 2020, p. 102081, 2021, doi: 10.1016/j.jobe.2020.102081.

[74] I. Zafar, K. Rashid, and M. Ju, “Synthesis and characterization of lightweight aggregates through geopolymerization and microwave irradiation curing,” *J. Build. Eng.*, vol. 42, no. January, p. 102454, 2021, doi: 10.1016/j.jobe.2021.102454.

[75] A. Hajimohammadi, T. Ngo, and P. Mendis, “How does aluminium foaming agent impact the geopolymer formation mechanism?,” *Cem. Concr. Compos.*, vol. 80, pp. 277–286, 2017, doi: 10.1016/j.cemconcomp.2017.03.022.

Chapter 2

KNEE JOINT BIOMECHANICS

Sabri UZUNER[1]

1. INTRODUCTION

The human knee joint is a highly specialized structure that bears significant mechanical loads while allowing controlled movement essential for daily and athletic activities [1-5]. It connects the femur, tibia, and patella through a complex arrangement of articular cartilage, menisci, ligaments, tendons, and synovial components. This structural organization enables the knee to function as both a hinge and a pivot joint, providing stability under compression while permitting rotation and translation during locomotion. The menisci act as fibrocartilaginous cushions that distribute loads and enhance joint congruency, whereas the articular cartilage minimizes friction and supports pressure through its fluid-filled matrix. Together, these elements form an integrated biomechanical system capable of maintaining balance between flexibility and durability under varying mechanical demands.

However, the knee joint is also one of the most frequently injured and degenerated structures in the human body [6-8]. Mechanical or structural disruption in any of its components can result in altered load transmission and pathological conditions. Meniscectomy, for instance, reduces the joint's ability to distribute loads, leading to increased contact pressures and accelerated cartilage wear [9-11]. Similarly, anterior cruciate ligament (ACL) deficiency compromises anterior–posterior and rotational stability, inducing abnormal tibiofemoral kinematics and secondary damage to meniscal and cartilage tissues [6, 7, 12-14]. These alterations often trigger early degenerative changes and osteoarthritis, even after surgical intervention. Understanding the underlying mechanics of such pathological states is therefore essential for improving clinical outcomes and rehabilitation strategies.

To investigate these complex behaviors, numerous experimental approaches have been developed. Cadaveric testing [15-17], robotic simulators [18-20], and in vivo imaging methods such as MRI-based motion tracking and dual

[1] Assist. Prof. Dr., Department of Mechatronics Engineering/Faculty of Engineering, Duzce University, Turkey, sabriuzuner@duzce.edu.tr, (ORCID: 0000-0002-9099-1324)

fluoroscopy have been instrumental in quantifying joint forces, contact areas, and ligament strains under controlled conditions [21, 22]. These techniques have advanced our knowledge of knee mechanics but remain limited in scope. The inherent variability of biological tissues, difficulties in controlling boundary conditions, and the impossibility of measuring internal stresses or fluid pressures restrict the completeness of experimental data [23-27]. Such constraints have motivated the use of computational modeling, which offers a powerful complement by enabling virtual experiments that replicate physiological and pathological loading scenarios with controllable parameters.

Among computational techniques, finite element (FE) modeling has become the standard tool for simulating knee joint mechanics [28-30]. Early models represented cartilage and menisci as linear elastic materials, providing only static estimates of stress and deformation [31-34]. Later, biphasic and poroelastic formulations were introduced to capture the interaction between the solid matrix and interstitial fluid, accounting for time-dependent creep and relaxation behaviors [23, 25, 35, 36]. The most advanced of these approaches, fibril-reinforced poromechanical (FRP) models, integrate the orientation and mechanical contribution of collagen fibers with the flow of interstitial fluid [37-41]. These models reproduce the anisotropic and nonlinear characteristics of joint tissues, allowing realistic simulation of physiological loading, degeneration, and recovery. As a result, FRP modeling has become an indispensable tool for interpreting experimental findings and guiding clinical decisions related to cartilage and meniscal health.

Looking forward, the field of knee joint modeling is evolving toward greater automation, efficiency, and generalizability. Statistical Shape Modeling (SSM) enables the representation of anatomical variability across populations, providing geometric templates that improve model standardization and clinical relevance [42]. In parallel, artificial intelligence (AI) tools are increasingly used to automate segmentation, estimate tissue material properties, and predict joint responses without time-intensive simulations [43]. These developments enhance reproducibility and broaden access to advanced biomechanical analysis.

In conclusion, computational modeling, particularly poromechanical and fibril-reinforced approaches, has revolutionized our ability to analyze, predict, and interpret the mechanical behavior of the knee joint. By combining experimental validation with advanced numerical techniques, researchers can now study the interplay between structure, function, and pathology with unprecedented precision. This chapter aims to provide readers with a comprehensive understanding of the biomechanical principles, modeling methodologies, and analytical frameworks that underpin modern knee joint

analysis, emphasizing how these tools can inform both scientific exploration and clinical application.

2. ANATOMY AND BIOMECHANICAL FUNCTION OF THE KNEE JOINT

2.1 Anatomical Structure, Fiber Orientation, and Insertion Regions

The knee joint is one of the most complex synovial joints in the human body, capable of bearing high loads while maintaining a wide range of motion. Its main components include the femur, tibia, and patella, as well as the articular cartilage that covers the joint surfaces, the menisci that regulate tibiofemoral contact, and four principal ligaments: ACL, PCL, MCL, and LCL, which provide static stability (Figure 1). The coordinated interaction among these elements ensures both mechanical strength and dynamic balance of the joint.

The articular cartilage is a layer of hyaline cartilage covering the femoral condyles and tibial plateau, typically 2–4 mm thick [4, 44]. It consists of a dense collagen fibril network embedded in a proteoglycan-rich matrix. Near the surface, collagen fibrils are oriented parallel to the articular plane, reducing shear friction; in the deeper layers, they are oriented perpendicularly, improving resistance to compressive forces. This zonal organization allows the tissue to dissipate energy and limit deformation under loading. As the cartilage is avascular and aneural, it receives nutrients through diffusion from the synovial fluid; hence, mechanical loading plays a key role in regulating fluid movement and maintaining tissue homeostasis.

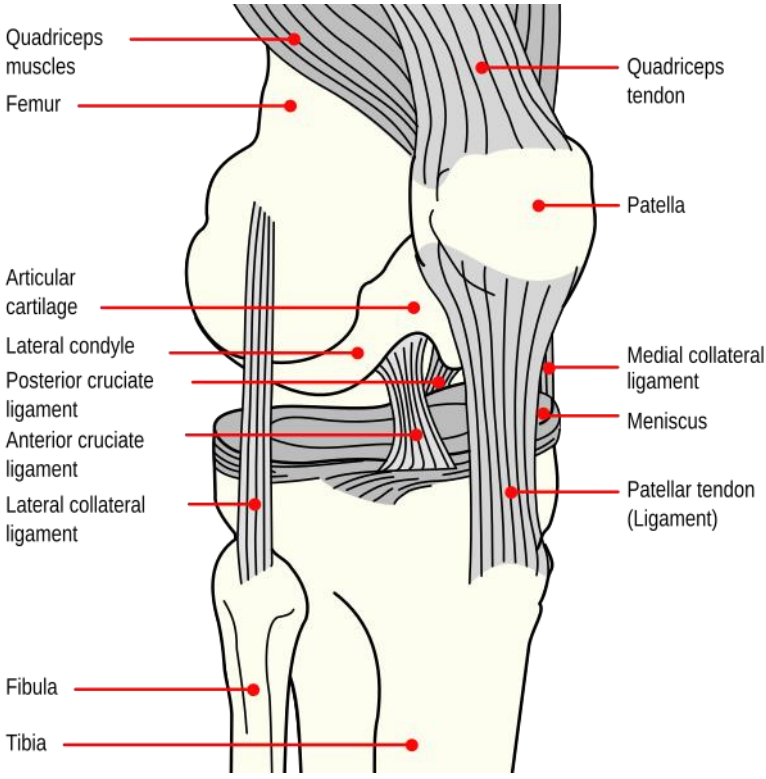

Figure 1 Knee Joint Anatomy with Labeled Stabilizing Structures (ACL, PCL, Collaterals, Menisci) [45]

The menisci are crescent-shaped fibrocartilaginous structures located between the femoral condyles and tibial plateau. The medial meniscus is C-shaped and more firmly attached to the tibia, while the lateral meniscus is more circular and mobile. Composed primarily of type I collagen, the meniscal fibril network exhibits circumferential orientation along the periphery and radial alignment toward the center. This architecture enables the menisci to withstand both circumferential tensile and compressive forces. The anterior and posterior horns of each meniscus are anchored to the tibial plateau, facilitating the transfer of loads from the femur to the tibia [46].

The PCL, MCL, and LCL complement the joint's passive stabilization. The PCL originates from the posterior intercondylar area of the tibia and inserts into the lateral surface of the medial femoral condyle, preventing posterior translation of the tibia [47]. The MCL extends from the medial epicondyle of the femur to the medial surface of the tibia, resisting valgus stresses, and also contributes to medial meniscal stability through partial attachments [48]. The LCL runs from the lateral epicondyle of the femur to the head of the fibula,

counteracting varus forces. Together, these ligaments reinforce the joint capsule and maintain medial-lateral stability [49].

The ACL is the central stabilizing ligament of the knee [12]. It originates from the anterior intercondylar area of the tibia and extends obliquely upward, backward, and laterally to attach to the medial surface of the femoral lateral condyle. The ligament consists of two principal bundles: the anteromedial (AM) and posterolateral (PL) bundles, which function synergistically at different flexion angles. Its collagen-rich microstructure, composed mainly of type I collagen with minor elastin content, provides high tensile strength with limited elasticity (Figure 2). The femoral and tibial insertion sites are asymmetrical, with the tibial attachment slightly larger, producing heterogeneous stress distribution along the ligament.

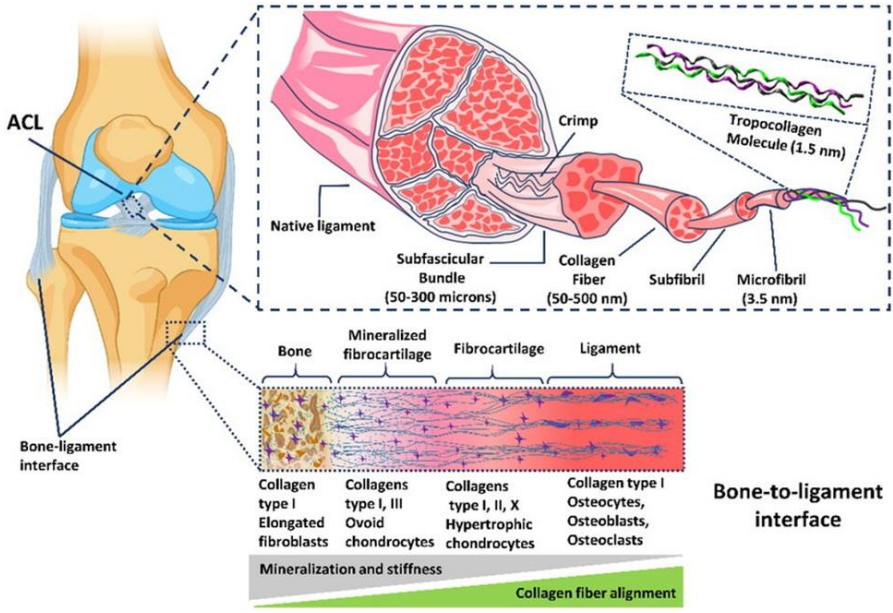

Figure 2 Collagen alignment in the ACL and insertion sites [50].

Overall, the structural integrity of the knee, defined by the organization of cartilage, menisci, and ligaments, forms the foundation of joint stability. The precise anatomical arrangement and fiber orientation of these components are crucial for understanding the mechanisms of load transfer and motion control, which will be discussed in the following section.

2.2 Knee Joint Load Bearing, Translation, and Rotation Control

The knee joint serves as a key biomechanical interface between the lower limb segments, transmitting substantial loads during standing, walking, and dynamic activities such as jumping or pivoting [51]. Load distribution across the joint is primarily managed by the geometry of the femoral condyles and tibial plateau, the viscoelastic behavior of the articular cartilage, and the presence of the menisci that expand the contact area under compression [52]. During a static stance, the joint typically supports forces equivalent to two to three times the body weight [53]. During activities such as stair climbing or squatting, this load can increase up to five to seven times the body weight. The menisci and cartilage deform in a complementary manner to disperse stresses and maintain joint congruency, ensuring both mechanical efficiency and protection of subchondral bone.

Anterior–posterior translation of the tibia relative to the femur is controlled by the cruciate ligaments, with the ACL limiting anterior motion and the PCL restraining posterior displacement. These ligaments act synergistically with the articular surfaces to maintain joint kinematics within a physiologic range. When the ACL is intact, it functions as a mechanical feedback element, providing tension that resists tibial sliding during weight bearing. In contrast, loss of ACL integrity increases anterior translation, alters load distribution across the tibiofemoral cartilage [6, 14], and can cause secondary adaptations in the menisci and collateral ligaments.

Rotational stability of the knee is governed by the orientation of the condyles, the shape of the tibial plateau, and the tension of the surrounding ligaments. Internal and external rotations occur around an instantaneous axis that shifts depending on flexion angle and ligament strain. The ACL and PCL, in conjunction with the medial and lateral collateral ligaments, regulate these coupled motions to prevent excessive torsional stress. The coordination among these structures allows the knee to combine flexibility with stability, a feature that distinguishes it from purely hinge-like joints.

2.3 Viscoelastic and Poroelastic Properties of the Knee Joint

The mechanical behavior of the knee joint is governed not only by its geometry and ligamentous constraints but also by the intrinsic time-dependent properties of its soft tissues. Articular cartilage, menisci, and ligaments exhibit viscoelastic and poroelastic characteristics that enable the joint to absorb shocks, distribute loads, and adapt to varying rates of deformation [52, 54]. In this section, the focus is on describing the knee joint's overall mechanical behavior rather than its mathematical representation, emphasizing how these

time-dependent properties contribute to joint function under physiological loading. Under rapid loading conditions, these tissues behave stiffly and store more elastic energy [31-34], whereas under sustained loading, they gradually deform due to fluid exudation and collagen network relaxation. This dual solid–fluid interaction (Figure 3) underlies the knee's time-dependent mechanical response [23].

Articular cartilage demonstrates a pronounced viscoelastic response due to its composite structure consisting of a dense collagen fibril network and a fluid-saturated proteoglycan matrix. When the tissue is compressed, interstitial fluid pressurization initially bears most of the load, reducing the effective stress on the solid matrix. Over time, the fluid gradually diffuses through the porous network, leading to stress relaxation and creep. The rate of this fluid redistribution depends on the tissue permeability and the stiffness of the collagen-proteoglycan matrix. Consequently, cartilage can maintain joint congruency under transient loads while minimizing wear and energy loss [25, 55, 56].

Similarly, the menisci show a combined viscoelastic and poroelastic behavior. The circumferential fiber architecture and hydrated extracellular matrix allow them to resist both compressive and tensile loads. During dynamic motion, internal fluid migration within the meniscus contributes to its damping capacity, enhancing energy dissipation and reducing peak contact pressures on the articular surfaces. Ligaments such as the ACL and PCL also exhibit time-dependent deformation known as "ligament creep," which reflects the gradual rearrangement of collagen fibrils and the movement of interstitial water under sustained tension [57, 58].

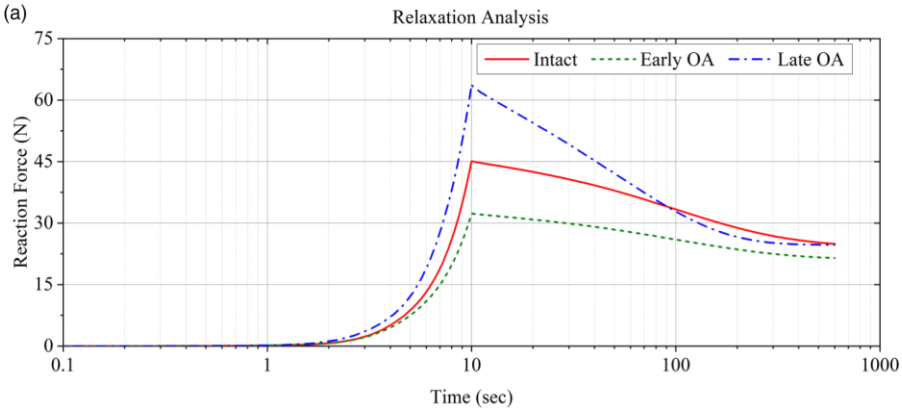

a)

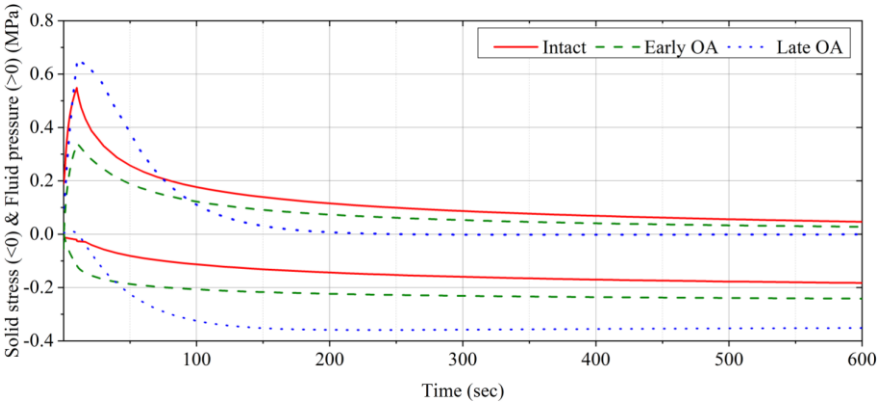

b)

Figure 3 a) Viscoelastic response of tibial cartilage under constant compressive displacement (0.3 mm) in intact, early osteoarthritis (OA), and late OA models — stress relaxation behavior, b) Poroelastic load-sharing behavior of tibial cartilage under sustained compressive force (50 N) — fluid–solid stress interaction during creep [27].

The interplay between viscoelasticity and poroelasticity is essential for joint durability. These mechanisms enable the knee to sustain millions of loading cycles throughout life without structural failure. Disturbances in this balance, such as reduced fluid pressurization or collagen network degradation, can lead to increased stress concentration and progressive degeneration, as seen in osteoarthritis. Understanding these coupled mechanical phenomena provides the foundation for developing realistic computational models. The fibril-reinforced poromechanical framework, discussed in the following section, integrates solid-matrix behavior and fluid dynamics to simulate the complex time-dependent response of the knee joint.

3. Poromechanical Framework for Knee Joint Modeling

3.1 Poromechanical Theory: Solid Matrix, Fluid Phase, and Fibril Contribution

The poromechanical theory describes biological tissues such as cartilage and ligaments as biphasic systems composed of a deformable solid matrix and an interstitial fluid phase. This framework acknowledges that soft tissues do not respond to mechanical loads instantaneously; instead, their deformation and stress evolution occur over time as fluid moves through the porous structure. The solid matrix, primarily composed of collagen fibers and proteoglycans, provides shape and stiffness, while the fluid phase supports compressive loads through hydrostatic pressure. When an external load is applied, a portion of the stress is initially carried by the fluid, preventing excessive deformation. Over time, as the fluid redistributes or exudes, the solid matrix gradually bears a greater load [56].

In the knee joint, this solid–fluid interaction is fundamental to its ability to sustain repetitive loading without permanent damage. Articular cartilage, for instance, acts as a natural shock absorber, where interstitial water pressurization accounts for more than 80% of the load during short-term impacts [59]. As the load persists, fluid flow and redistribution lead to phenomena such as creep and stress relaxation. This dynamic load transfer allows the joint to adapt to various motion conditions while minimizing energy dissipation and wear.

The fibrillar architecture within the solid matrix further adds complexity. Collagen fibrils act as reinforcement elements that resist tension and limit excessive swelling of the proteoglycan-rich matrix. Their orientation varies spatially: near the cartilage surface, fibrils run parallel to the articular plane, while in deeper layers they orient perpendicularly to the bone interface. This anisotropic configuration provides the tissue with direction-dependent stiffness, an essential property for joint stability under multidirectional forces. Thus, the poromechanical theory, enriched with fibril contribution, captures how cartilage and ligaments combine fluid pressurization and collagen tension to maintain functional integrity under physiological loading.

3.2 Fibril-Reinforced Poromechanical (FRP) Models

Fibril-reinforced poromechanical (FRP) models extend the biphasic theory by integrating collagen fibrils as explicit structural reinforcements within the solid matrix. These fibrils represent the primary load-bearing elements in tension, while the nonfibrillar matrix supports compressive stresses. The interstitial fluid governs hydraulic flow and pressure development, linking the mechanical and transport behaviors. In the knee joint, this tri-phasic system

provides a realistic representation of how cartilage, menisci, and ligaments interact during complex motion [60, 61].

In FRP models, fibrils are typically modeled as nonlinear elastic springs that stiffen under tension but buckle under compression, mimicking the behavior of collagen bundles observed experimentally [62]. The matrix is treated as an isotropic, compressible medium, and the fluid phase follows Darcy's law for flow through porous media. When the knee is loaded, the fibrillar network carries tensile forces along preferred directions, while the fluid resists short-term compression by building pressure. Over time, fluid redistribution and matrix deformation lead to time-dependent stress relaxation consistent with experimental data.

The advantage of FRP models lies in their ability to capture both the anisotropy and time-dependence of real tissue mechanics. For instance, in ACL loading simulations, FRP formulations have shown that altered collagen alignment or decreased permeability can significantly shift the balance between solid and fluid load support [63, 64]. Similarly, meniscal degeneration or cartilage fibrillation can be modeled as changes in fibril stiffness and density, allowing direct biomechanical interpretation of pathology [46]. In summary, FRP modeling bridges tissue-level microstructure and joint-level function, enabling mechanistic insights into both healthy and diseased states.

3.3 Comparison with Conventional Elastic Models

Traditional elastic models describe joint tissues as homogeneous materials that respond instantaneously to loading, neglecting the role of interstitial fluid and fibrillar architecture. While these models are computationally simpler and can approximate global joint kinematics, they fail to capture critical time-dependent and directional behaviors. In an elastic formulation, the applied stress is directly proportional to strain, implying that once the load is removed, the tissue instantly returns to its original shape. However, biological tissues such as cartilage undergo recovery and deformation over time due to fluid flow and collagen rearrangement.

Viscoelastic models partially improve this description by introducing time-dependent damping elements, but they remain limited in explaining fluid–solid coupling and permeability effects. In contrast, poromechanical and FRP models explicitly simulate the transient load-sharing between the fluid and solid phases, allowing realistic prediction of phenomena such as creep, stress relaxation, and pressure dissipation. These models can explain why the knee joint exhibits both immediate elastic recovery after low-intensity motion and delayed recovery under sustained compression.

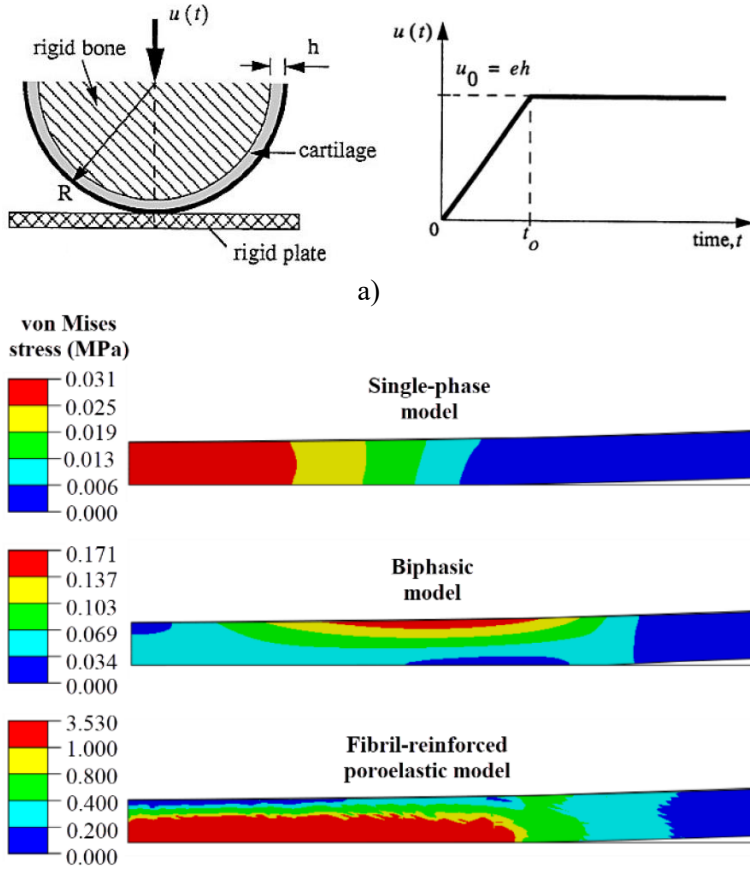

Figure 4 Comparative evaluation of cartilage FE formulations under identical loading. (a) Axisymmetric geometry and ramp–hold displacement. (b) Head-to-head comparison of predicted von Mises stress for single-phase (elastic), biphasic, and fibril-reinforced poromechanical (FRP) models at peak compression (0.08 mm, t = 100 s). [41]

From a physiological standpoint, poromechanical frameworks also provide superior predictive power for clinical conditions. For example, in osteoarthritis, the loss of proteoglycan content increases tissue permeability and alters fibril tension, which can be captured directly in FRP simulations. Elastic models, lacking this biphasic representation, cannot reproduce such degeneration-driven mechanical shifts. Therefore, while elastic models serve as a starting point for simplified analysis, FRP-based poromechanical models offer a more comprehensive and biologically relevant framework for studying knee joint mechanics under both healthy and pathological conditions.

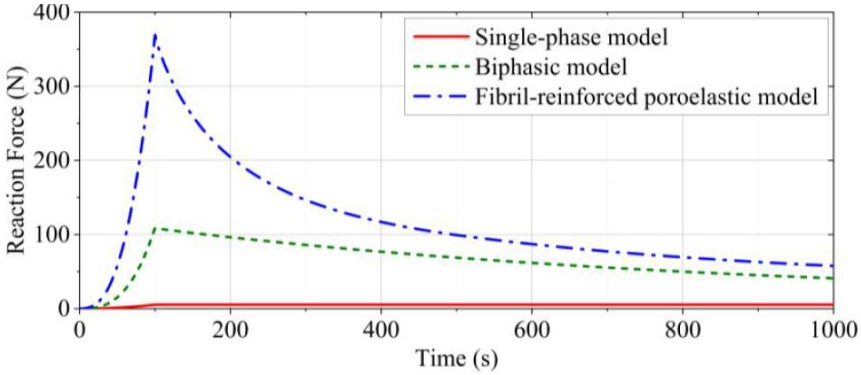

Figure 5 Comparison of reaction forces in single-phase (elastic), biphasic, and fibril-reinforced poroelastic cartilage models under compressive loading (8 % strain, 0.08 mm displacement) [65]. Finite element simulations were performed using an axisymmetric knee cartilage geometry, where the rigid bone was displaced vertically against a stationary plate to produce 8 % compression. The tibial surface was fixed, and frictional contact ($\mu = 0.02$) was defined between surfaces. The figure illustrates how each constitutive formulation responds differently: the single-phase model shows limited load support due to absence of fluid, the biphasic model displays increased reaction through fluid pressurization, and the fibril-reinforced model exhibits the highest reaction force ($\approx$ 369 N) due to combined fluid and collagen fibril effects.

4. Model Validation: Comparison with Literature and Experimental Data

Validation of finite element (FE) models of the knee joint is essential to confirm that simulated kinematics and load-transfer mechanisms accurately reflect physiological reality. Due to the knee's complex interaction between bones, cartilage, menisci, and ligaments, validation must address both local tissue behavior and global joint response [66].

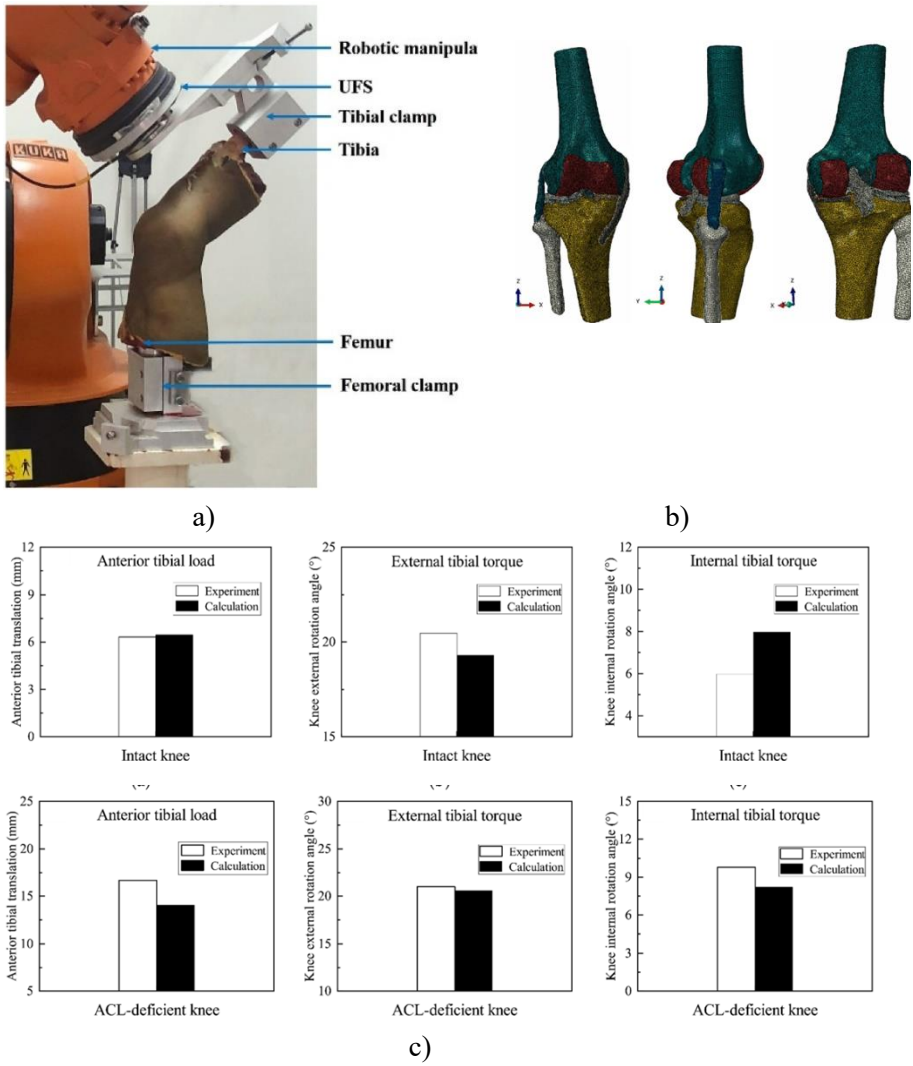

Figure 6 Experimental–computational framework for assessing knee joint laxity under tibial loading. (a) Robotic setup with a universal force/torque sensor used to apply anterior tibial load and axial torques to a cadaveric knee. (b) Subject-specific finite element knee models showing bones, cartilage and soft tissues. (c) Representative comparisons of experiment and model predictions for anterior tibial translation and tibial rotations in intact and ACL-deficient conditions. [19]

Experimental validation strategies generally fall into three main categories. In vitro studies use cadaveric specimens and instrumented setups to measure ligament strain, joint reaction forces, and contact pressures under controlled loading conditions [15-17]. In vivo techniques, such as dual-fluoroscopy and

MRI-based motion tracking, enable noninvasive quantification of cartilage deformation and ligament elongation during physiological movement [21, 22]. More recently, robotic simulators have been used to apply repeatable multi-axial loads and joint motions, providing benchmark datasets for validating both static and dynamic FE analyses [19, 20]. These complementary approaches ensure that computational models reproduce realistic knee mechanics and fluid–solid interactions within acceptable experimental margins. Collectively, they form the foundation for reliable simulation of both healthy and pathological knee conditions [30].

5. Clinical and Rehabilitation Applications of Knee Joint Analysis

Advances in computational modeling of the knee joint have provided powerful tools for translating biomechanical understanding into clinical and rehabilitation practice. FE simulations, musculoskeletal models, and image-based reconstructions allow clinicians and researchers to assess tissue loading, joint stability, and surgical outcomes with unprecedented detail. These approaches bridge the gap between experimental biomechanics and patient-specific care, providing a framework for predicting how structural or functional changes influence overall joint health [67].

Clinically, validated FE and multibody models are increasingly used to guide surgical decision-making and implant design. By simulating procedures such as total knee arthroplasty, ligament reconstruction, or meniscal transplantation, these models enable preoperative evaluation of stress distributions, contact mechanics, and alignment strategies tailored to individual anatomy [68-70]. For instance, subject-specific poromechanical models have been applied to assess postoperative cartilage loading and predict regions at risk for early degeneration, providing quantitative metrics that complement imaging-based diagnostics [71]. Similarly, computational analyses of meniscal function have clarified how resection depth and graft geometry affect tibiofemoral contact mechanics, informing meniscus-sparing surgical techniques and rehabilitation planning [26, 72].

In the context of rehabilitation, knee modeling supports the development of personalized exercise regimens and assistive technologies. Coupling FE models with musculoskeletal simulations enables estimation of muscle and ligament forces during dynamic tasks such as walking, squatting, or stair ascent—data that are difficult to obtain experimentally. Such insights facilitate the optimization of neuromuscular retraining protocols and the design of orthoses or robotic exoskeletons that restore physiological load sharing without overloading compromised tissues [73]. Moreover, poromechanical frameworks

have shed light on fluid pressurization and tissue recovery kinetics, helping to define safe loading limits and rest intervals during early rehabilitation following ligament or cartilage repair [71]

Ultimately, knee joint modeling serves as a digital extension of clinical reasoning, a “virtual laboratory” that integrates imaging, kinematics, and material behavior to enable predictive simulations [74]. As imaging resolution, computational power, and machine learning–based calibration techniques continue to advance, these models are expected to play an even greater role in precision orthopaedics, enabling clinicians to tailor surgical, preventive, and rehabilitative strategies to the biomechanical profile of each patient [75, 76].

6. Future Directions in Knee Joint Analysis

Recent developments in computational biomechanics have transformed knee joint analysis from purely mechanical modeling toward data-driven frameworks that capture anatomical variability and automate prediction. Among these, Statistical Shape Modeling (SSM) [77] and artificial intelligence (AI) [78] approaches have emerged as two of the most promising directions for improving the efficiency, reproducibility, and clinical relevance of knee joint simulations.

SSM provides a population-based representation of joint geometry by quantifying morphological variation across large imaging datasets. Unlike subject-specific FE models, which focus on individual anatomy, SSM generates statistical modes of variation that describe how bone and cartilage geometry differ across a cohort. This capability allows researchers to simulate mechanical responses not only for a single patient but for an entire population, enabling the identification of common biomechanical trends and risk factors. Clinically, this offers a more reliable and generalizable foundation for evaluating treatment outcomes, surgical techniques, or degenerative progression at the population level. Furthermore, SSM frameworks facilitate the semi-automated generation of FE meshes, reducing dependence on manual segmentation and minimizing operator variability [42, 79, 80].

In parallel, AI has begun to play an important role in accelerating knee joint analysis and improving predictive accuracy. Deep learning algorithms are increasingly used to automate cartilage and meniscus segmentation from MRI or CT images, substantially reducing preprocessing time. Moreover, machine learning models can approximate the outcomes of time-consuming FE simulations, providing rapid estimates of stress, strain, or load distribution under various physiological conditions [43]. AI-based regression and neural network methods have also been applied to infer tissue material properties

directly from limited experimental data, improving the personalization and calibration of poromechanical models. These data-driven techniques enable researchers to conduct large-scale parametric studies that would otherwise be computationally prohibitive using conventional numerical solvers.

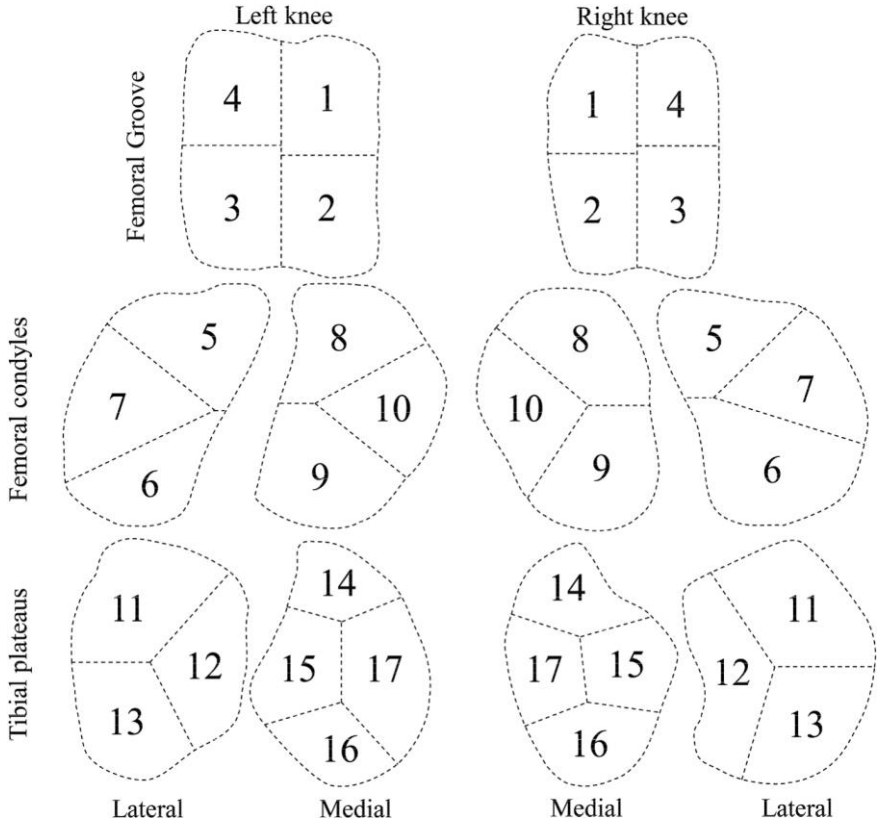

Figure 7 Machine learning–based clustering of articular cartilage regions for poromechanical characterization [43] Machine learning (hybrid K-means + differential evolution) was applied to indentation–relaxation and thickness data from porcine knee cartilage to segment the articular surfaces into 17 distinct regions with site-specific mechanical properties. This region-based mapping provides a framework for implementing tissue inhomogeneity in future poromechanical and FE models of the knee.

7. CONCLUSION

In summary, computational and poromechanical modeling of the knee joint has significantly advanced our understanding of how mechanical loads are distributed among cartilage, menisci, and ligaments. By capturing both solid–

fluid interactions and time-dependent tissue responses, these models provide a realistic representation of joint function under physiological and pathological conditions. Their integration into clinical and rehabilitation studies enables objective evaluation of joint stability, cartilage health, and treatment outcomes. Recent developments in statistical shape modeling and artificial intelligence further enhance this capability by improving computational efficiency and enabling population-level analyses. Collectively, these approaches establish a strong foundation for future research in knee biomechanics, bridging experimental evidence with predictive modeling to support more effective, data-driven orthopaedic decision-making.

REFERENCES

1. Mow, V.C. and R. Huiskes, *A brief history of science, and orthopaedic biomechanics.* Basic Orthopaedic Biomechanics and Mechanobiology. Philadelphia, Lippincot Williams and Wilkins, 2005: p. 1-28.
2. Athanasiou, K.A. and J. Sanchez-Adams, *Engineering the knee meniscus.* Synthesis Lectures on Tissue Engineering, 2009. 1(1): p. 1-97.
3. Günther, M. and R. Blickhan, *Joint stiffness of the ankle and the knee in running.* Journal of biomechanics, 2002. 35(11): p. 1459-1474.
4. Li, L. and S. Ahsanizadeh, *Computational modelling of articular cartilage*, in *Computational Modelling of Biomechanics and Biotribology in the Musculoskeletal System*. 2014, Elsevier. p. 205-243.
5. Uzuner, S., et al., *Dual fluoroscopic evaluation of human tibiofemoral joint kinematics during a prolonged standing: A pilot study.* Engineering science and technology, an international journal, 2019. 22(3): p. 794-800.
6. Uzuner, S. and L. Li, *Alteration in ACL loading after total and partial medial meniscectomy.* BMC Musculoskeletal Disorders, 2024. 25(1): p. 94.
7. Sanchis-Alfonso, V. and J.C. Monllau, *The ACL-deficient knee: A problem solving approach*. 2012: Springer Science & Business Media.
8. Andriacchi, T.P., et al., *Rotational changes at the knee after ACL injury cause cartilage thinning.* Clinical Orthopaedics and Related Research®, 2006. 442: p. 39-44.
9. Allen, A.A., G.L. Caldwell Jr, and F.H. Fu, *Anatomy and biomechanics of the meniscus.* Operative techniques in orthopaedics, 1995. 5(1): p. 2-9.
10. Bae, J.Y., et al., *Biomechanical analysis of the effects of medial meniscectomy on degenerative osteoarthritis.* Medical & biological engineering & computing, 2012. 50(1): p. 53-60.
11. Deng, R., S. Uzuner, and L. Li, *Impact of knee geometry on joint contact mechanics after meniscectomy.* Scientific Reports, 2024. 14(1): p. 28595.
12. Girgis, F.G., J.L. Marshall, and A.A.M. JEM, *The cruciate ligaments of the knee joint: anatomical. functional and experimental analysis.* Clinical Orthopaedics and Related Research®, 1975. 106: p. 216-231.
13. Kääb, M., et al., *The acute structural changes of loaded articular cartilage following meniscectomy or ACL-transection.* Osteoarthritis and cartilage, 2000. 8(6): p. 464-473.
14. Westermann, R.W., B.R. Wolf, and J.M. Elkins, *Effect of ACL reconstruction graft size on simulated Lachman testing: a finite element analysis.* The Iowa orthopaedic journal, 2013. 33: p. 70.

15. Maletsky, L., et al., *In vitro experimental testing of the human knee: a concise review.* The journal of knee surgery, 2016. 29(02): p. 138-148.
16. Johnson, C.I., D.J. Argyle, and D.N. Clements, *In vitro models for the study of osteoarthritis.* The Veterinary Journal, 2016. 209: p. 40-49.
17. Steinbrück, A., et al., *Influence of tibial rotation in total knee arthroplasty on knee kinematics and retropatellar pressure: an in vitro study.* Knee Surgery, Sports Traumatology, Arthroscopy, 2016. 24(8): p. 2395-2401.
18. Siciliano, B., et al., *Robotics: modelling, planning and control*. 2010: Springer Science & Business Media.
19. Ren, S., et al., *Finite element analysis and experimental validation of the anterior cruciate ligament and implications for the injury mechanism.* Bioengineering, 2022. 9(10): p. 590.
20. Branch, T., et al., *Assessment of knee laxity using a robotic testing device: a comparison to the manual clinical knee examination.* Knee Surgery, Sports Traumatology, Arthroscopy, 2017. 25(8): p. 2460-2467.
21. Uzuner, S., et al., *Creep behavior of human knee joint determined with high-speed biplanar video-radiography and finite element simulation.* Journal of the Mechanical Behavior of Biomedical Materials, 2022. 125: p. 104905.
22. Navacchia, A., et al., *Prediction of in vivo knee joint loads using a global probabilistic analysis.* Journal of biomechanical engineering, 2016. 138(3): p. 031002.
23. Mow, V.C., et al., *Biphasic creep and stress relaxation of articular cartilage in compression: theory and experiments.* Journal of biomechanical engineering, 1980. 102(1): p. 73-84.
24. Soulhat, J., M. Buschmann, and A. Shirazi-Adl, *A fibril-network-reinforced biphasic model of cartilage in unconfined compression.* J Biomech Eng., 1999. 121(3): p. 340-347.
25. Uzuner, S., et al. *Investigation of the Effect of Mesh Density and Element Type on Behavior of Biphasic Soft Tissues in Finite Element Analysis*. in *International Conference on Advanced Technologies, Computer Engineering and Science (ICATCES'18)*. 11.05.2018 - 13.06.2018. Karabuk.
26. Uzuner, S., et al., *Changes in Knee Joint Mechanics after Medial Meniscectomy Determined with a Poromechanical Model.* Journal of Biomechanical Engineering, 2020. 142(10): p. 101006.
27. Uzuner, S., *Numerical analysis of a poroelastic cartilage model: Investigating the influence of changing material properties in osteoarthritis.* Proceedings of the Institution of Mechanical Engineers,

Part E: Journal of Process Mechanical Engineering, 2024. 238(4): p. 1894-1902.
28. Engel, K., R. Herpers, and U. Hartmann, *Biomechanical Computer Models*. 2011: INTECH Open Access Publisher.
29. Peña, E., et al., *Computational modelling of diarthrodial joints. Physiological, pathological and pos-surgery simulations.* Archives of Computational Methods in Engineering, 2007. 14(1): p. 47-91.
30. Erdemir, A., et al., *Deciphering the "Art" in modeling and simulation of the knee joint: Overall strategy.* Journal of biomechanical engineering, 2019. 141(7).
31. Imran, A., *Cruciate Ligament Behaviour Analysed with Modelling and Simulation of the Human Knee*, in *Advances in Mechanical Engineering: Select Proceedings of CAMSE 2020*. 2021, Springer. p. 427-432.
32. Zielinska, B. and T.L.H. Donahue, *3D finite element model of meniscectomy: changes in joint contact behavior.* Journal of biomechanical engineering, 2006. 128(1): p. 115-123.
33. Vadher, S.P., et al. *Finite element modeling following partial meniscectomy: effect of various size of resection*. in *The 28th IEEE EMBS annual international conference*. 2006. New York City, USA: IEEE.
34. Verim, Ö., et al., *Anatomical comparison and evaluation of human proximal femurs modeling via different devices and FEM analysis.* The International Journal of Medical Robotics and Computer Assisted Surgery, 2013. 9(2): p. e19-e24.
35. Spilker, R.L., P.S. Donzelli, and V.C. Mow, *A transversely isotropic biphasic finite element model of the meniscus.* Journal of biomechanics, 1992. 25(9): p. 1027-1045.
36. Hosoda, N., et al. *Finite element analysis of articular cartilage model considering the configuration and biphasic property of the tissue*. in *13th International Conference on Biomedical Engineering*. 2009. Springer.
37. Wilson, W., et al., *Stresses in the local collagen network of articular cartilage: a poroviscoelastic fibril-reinforced finite element study.* Journal of biomechanics, 2004. 37(3): p. 357-366.
38. Julkunen, P., et al., *Uncertainties in indentation testing of articular cartilage: a fibril-reinforced poroviscoelastic study.* Medical engineering & physics, 2008. 30(4): p. 506-515.
39. Halonen, K., et al., *Optimal graft stiffness and pre-strain restore normal joint motion and cartilage responses in ACL reconstructed knee.* Journal of biomechanics, 2016. 49(13): p. 2566-2576.

40. Orozco, G.A., et al., *The effect of constitutive representations and structural constituents of ligaments on knee joint mechanics.* Scientific reports, 2018. 8(1): p. 2323.
41. Uzuner, S., *Exploring the Multifaceted Dynamics of Cartilage: A Comparative Modeling Study.* Duzce University Journal of Science and Technology, 2024. 12(2): p. 669-679.
42. Deng, R., et al., *Statistical Shape Modeling to Determine Poromechanics of the Human Knee Joint.* Annals of Biomedical Engineering, 2025. 53(3): p. 549-561.
43. Niasar, E.H.A. and L. Li, *Characterizing site-specific mechanical properties of knee cartilage with indentation-relaxation maps and machine learning.* Journal of the Mechanical Behavior of Biomedical Materials, 2023. 142: p. 105826.
44. Niasar, E.H.A., et al., *Region partitioning of articular cartilage with streaming-potential-based parameters and indentation maps.* Journal of the Mechanical Behavior of Biomedical Materials, 2024. 154: p. 106534.
45. Mysid. *Knee Diagram*. [cited 2025 September 18]; Available from: https://en.wikipedia.org/wiki/File:Knee_diagram.svg.
46. Petersen, W. and B. Tillmann, *Collagenous fibril texture of the human knee joint menisci.* Anatomy and embryology, 1998. 197(4): p. 317-324.
47. Logterman, S.L., F.B. Wydra, and R.M. Frank, *Posterior cruciate ligament: anatomy and biomechanics.* Current reviews in musculoskeletal medicine, 2018. 11(3): p. 510-514.
48. Memarzadeh, A. and J.T. Melton, *Medial collateral ligament of the knee: anatomy, management and surgical techniques for reconstruction.* Orthopaedics and trauma, 2019. 33(2): p. 91-99.
49. Grawe, B., et al., *Lateral collateral ligament injury about the knee: anatomy, evaluation, and management.* JAAOS-Journal of the American Academy of Orthopaedic Surgeons, 2018. 26(6): p. e120-e127.
50. Pashaki, P.V., et al., *Next generation nanocomposite biomaterials for ligament repair and regeneration.* Nanocomposites, 2024. 10(1): p. 373-404.
51. Andriacchi, T.P. and A. Mündermann, *The role of ambulatory mechanics in the initiation and progression of knee osteoarthritis.* Current opinion in rheumatology, 2006. 18(5): p. 514-518.
52. Kazemi, M. and L.P. Li, *A viscoelastic poromechanical model of the knee joint in large compression.* Medical engineering & physics, 2014. 36(8): p. 998-1006.

53. Morrison, J., *Bioengineering analysis of force actions transmitted by the knee joint.* Bio-Med, 1968. 3: p. 164-170.
54. Hamsayeh Abbasi Niasar, E. and L. Li, *Implication of region-dependent material properties of articular cartilage in the contact mechanics of porcine knee joint.* BMC Musculoskeletal Disorders, 2025. 26(1): p. 1-13.
55. Kazemi, M., Y. Dabiri, and L.P. Li, *Recent advances in computational mechanics of the human knee joint.* Computational and mathematical methods in medicine, 2013. 2013(Special Issue): p. 27.
56. Li, L., et al., *Nonlinear analysis of cartilage in unconfined ramp compression using a fibril reinforced poroelastic model.* Clinical Biomechanics, 1999. 14(9): p. 673-682.
57. Zhou, J., et al., *Tensile creep mechanical behavior of periodontal ligament: a hyper-viscoelastic constitutive model.* Computer Methods and Programs in Biomedicine, 2021. 207: p. 106224.
58. Myers, D., et al., *Artelon as a bio-scaffold to augment collateral ligament repair after knee dislocation.* Malaysian Orthopaedic Journal, 2022. 16(2): p. 110.
59. Abbot, A.E., W.N. Levine, and V.C. Mow, *Biomechanics of the Articular Cartilage.* The adult knee, 2003. 1: p. 81.
60. Dabiri, Y. and L.P. Li, *Influences of the depth-dependent material inhomogeneity of articular cartilage on the fluid pressurization in the human knee.* Medical engineering & physics, 2013. 35(11): p. 1591-1598.
61. Ebrahimi, M., et al., *Elastic, viscoelastic and fibril-reinforced poroelastic material properties of healthy and osteoarthritic human tibial cartilage.* Annals of biomedical engineering, 2019. 47(4): p. 953-966.
62. Sun, B., *The mechanics of fibrillar collagen extracellular matrix.* Cell Reports Physical Science, 2021. 2(8).
63. Li, L. and W. Herzog, *Strain-rate dependence of cartilage stiffness in unconfined compression: the role of fibril reinforcement versus tissue volume change in fluid pressurization.* Journal of biomechanics, 2004. 37(3): p. 375-382.
64. Li, L., M. Buschmann, and A. Shirazi-Adl, *A fibril reinforced nonhomogeneous poroelastic model for articular cartilage: inhomogeneous response in unconfined compression.* Journal of biomechanics, 2000. 33(12): p. 1533-1541.
65. Uzuner, S., *Exploring the Multifaceted Dynamics of Cartilage: A Comparative Modeling Study.* Düzce Üniversitesi Bilim ve Teknoloji Dergisi, 2024. 12(2): p. 669-679.

66. Bendjaballah, M., A. Shirazi-Adl, and D. Zukor, *Finite element analysis of human knee joint in varus-valgus.* Clinical biomechanics, 1997. 12(3): p. 139-148.
67. Erdemir, A., et al., *Considerations for reporting finite element analysis studies in biomechanics.* Journal of biomechanics, 2012. 45(4): p. 625-633.
68. Shirazi, R. and A. Shirazi-Adl, *Analysis of partial meniscectomy and ACL reconstruction in knee joint biomechanics under a combined loading.* Clinical biomechanics, 2009. 24(9): p. 755-761.
69. Li, L.P., J.T.M. Cheung, and W. Herzog, *Three-dimensional fibril-reinforced finite element model of articular cartilage.* Medical & biological engineering & computing, 2009. 47(6): p. 607.
70. Niasar, E.H.A. and L. Li, *Three-dimensional finite element modeling of human knee joint*, in *Cartilage Tissue and Knee Joint Biomechanics*. 2024, Elsevier. p. 243-264.
71. Mononen, M., et al., *Alterations in structure and properties of collagen network of osteoarthritic and repaired cartilage modify knee joint stresses.* Biomechanics and modeling in mechanobiology, 2011. 10(3): p. 357-369.
72. Peña, E., et al., *Finite element analysis of the effect of meniscal tears and meniscectomies on human knee biomechanics.* J Clinical Biomechanics, 2005. 20(5): p. 498-507.
73. Lloyd, D.G. and T.F. Besier, *An EMG-driven musculoskeletal model to estimate muscle forces and knee joint moments in vivo.* Journal of biomechanics, 2003. 36(6): p. 765-776.
74. Chao, E.Y. and J. Lim, *Virtual Interactive Musculoskeletal System (VIMS) in orthopaedic translational research.* Journal of Orthopaedic Translation, 2013. 1(1): p. 25-40.
75. Yadav, A.K., et al., *From Data to Precision: The Transformative Role of AI and Machine Learning in Modern Orthopaedic Practice.* Journal of Clinical Orthopaedics and Trauma, 2025: p. 103101.
76. Lalehzarian, S.P., A.K. Gowd, and J.N. Liu, *Machine learning in orthopaedic surgery.* World journal of orthopedics, 2021. 12(9): p. 685.
77. Chambers, T., *Assessing the Impact of Femur Morphological Variations on Pediatric Hip Joint Biomechanics Using Statistical Shape Modeling.* 2024.
78. Gurung, B., et al., *Artificial intelligence for image analysis in total hip and total knee arthroplasty: a scoping review.* The bone & joint journal, 2022. 104(8): p. 929-937.

79. Sarkalkan, N., H. Weinans, and A.A. Zadpoor, *Statistical shape and appearance models of bones.* Bone, 2014. 60: p. 129-140.
80. Van Dijck, C., et al., *Statistical shape model-based prediction of tibiofemoral cartilage.* Computer methods in biomechanics and biomedical engineering, 2018. 21(9): p. 568-578.

Chapter 3

A STATISTICAL APPROACH TO MACHINABILITY

Engin NAS[1]

1. INTRODUCTION

Machinability is an engineering concept that describes how easily or how difficult a workpiece material is to machine. Methods used to evaluate the optimal machining factors for this concept have gradually relied on statistical techniques. Statistical methods have become increasingly important in measuring variables such as tool life, cutting forces, surface roughness, and machining time, and comparing their interactions (Figure 1.). Evaluating the machining process using statistical indicators such as the Process Capability Index (Cp) and the True Process Capability Index (Cpk) is now part of quality control. Cp represents the overall variability of the process, that is, the ratio of the measured values to the tolerance range [1].

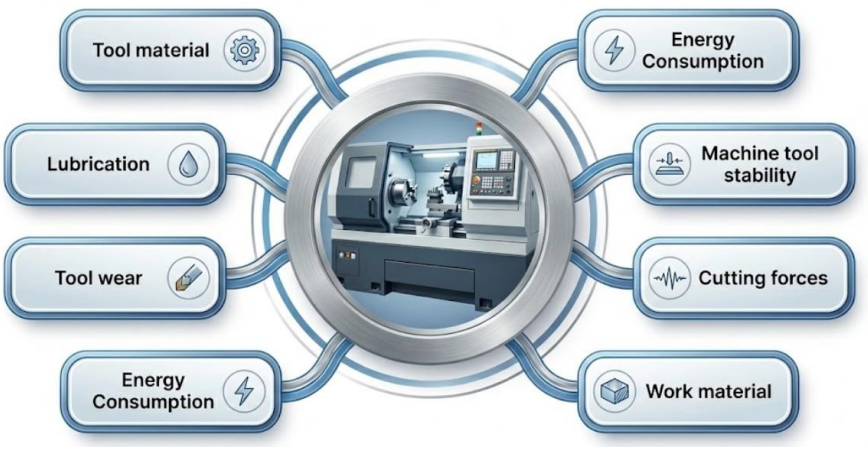

Figure 1. Components affecting machinability efficiency

[1]Associate. Prof. Dr., Dr. Engin PAK Cumayeri Vocational School, Duzce University, Turkey, enginnas@duzce.edu.tr, (ORCID: 0000-0002-4828-9240)

Parameters such as cutting speed, feed rate, and depth of cut, used to assess machinability, have been studied over time using statistical methods to determine surface quality in machined materials. Early studies on this were conducted by Frederick Winslow Taylor in the early 1900s, who conducted systematic experiments on tool geometry, materials, and cutting conditions to determine cutting speeds and feed rates [2]. Although not specifically for machinability, an important turning point in statistical control methods (e.g., control charts) for production processes was the development of control charts by Walter A. Shewhart in the 1920s [3]. Academic studies on the machinability of materials have increased significantly since the 1990s. In the late 1920s and 1930s, joint standardization efforts (AISI/SAE) were undertaken on steel naming/numbering systems, and this standardization laid the groundwork for future machinability comparisons between steel grades [4-6]. The idea of machinability ratings for various materials emerged in the late 1930s [7]. From the 1940s onwards, scientific (mechanically based) modelling and systematic experimental designs accelerated; the rise of "modern" statistical analyses (DOE/ANOVA/RSM) developed during this period. In the 1970s, correlation analyses, that is, parameter interactions, began to be compared experimentally and statistically in the context of machinability [8-10]. In the late 1980s and 1990s, Design of Experiment (DOE), ANOVA, Taguchi, and Response Surface (RSM) methods began to be applied across all areas of machinability. One of the earliest known papers was published by I. A. Choudhury in 1995 [11].

2. ADVANCED STATISTICAL TECHNIQUES AND EXPERIMENTAL DESIGNS

While RSM and Taguchi were early applications in milling/turning/drilling in the early 1990s, they became prominent in the 2000s (Taguchi/ANOVA wave between 2001 and 2007). Besides ANOVA–Taguchi–RSM, many statistical approaches are used in machinability [12-14]. Design of Experiments (DOE) alternatives include full/fractional factorial designs, Plackett–Burman (screening), Box–Behnken, D-optimal (constrained designs), and Latin hypercube sampling (for simulations). Robust design (Taguchi-independent): Multiple output optimization with desirability function [15]. For modeling and predictive maintenance: Multiple/polynomial regression, GLM (e.g., force/energy with log-link), ANCOVA (comparison with covariance). Kriging/Gaussian Process (surrogate model for surface roughness and force), Spline regression (nonlinear response). Bayesian hierarchical models (combining variations across batches/replicates). Bootstrap (confidence intervals/sensitivity), Monte Carlo (tolerance chain/capacity risk calculation)

[16]. For reliability and tool life, Weibull/lognormal life distributions, right-censored data analysis (test stopping). Accelerated life tests, Cox or parametric life models (relating tool life to speed–feed–depth) [17]. For multivariate methods, PCA (force–vibration–current sensors dimension reduction), PLS (multiple input → multiple output), MANOVA (comparing multiple responses simultaneously), Hotelling's T^2 and MEWMA (multivariate control) [18]. The most commonly used optimization methods and their relationships in the literature were visualized through keyword analysis using WoS (2020-2025) data (Figure 2). The bibliometric analysis map reveals that researchers still rely on classical DoE methods for data generation (Red zone), but are rapidly turning to AI techniques such as Artificial Neural Networks and Deep Learning for modelling and optimization (Orange/Green zone).

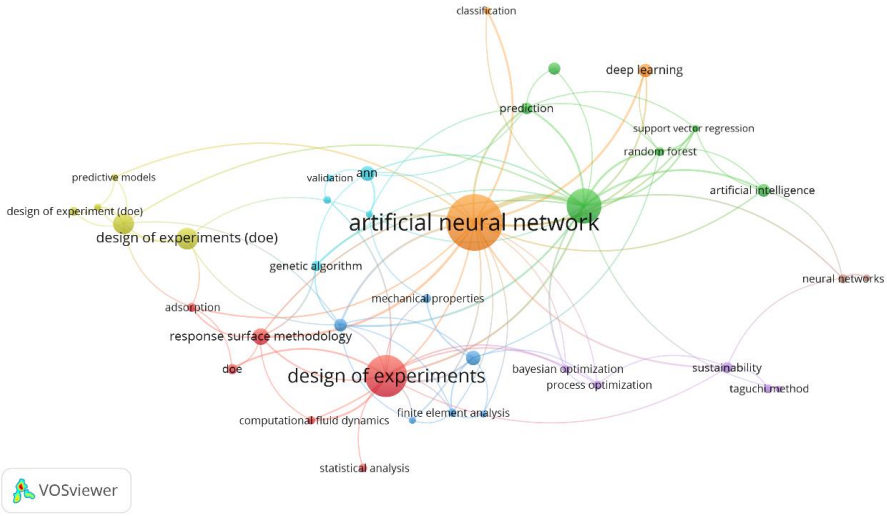

Figure 2. Visualization of optimization methods used in machinability research between 2020 and 2025.

For process monitoring and qualification, EWMA/CUSUM control charts (capture small drifts), Pp/Ppk (long-term qualification), and non-normal qualification (Johnson, Box–Cox). Gage R&R (surface roughness/measurement device repeatability & reproducibility). For comparison tests (outside the assumptions), Kruskal–Wallis, Mann–Whitney, Friedman (non-parametric), and permutation tests. For time series and process dynamics analysis, ARIMA/state-space (vibration/acoustic emission flows), spectrum/envelope analysis, and statistical feature extraction are preferred. For multi-objective decision-making/grey methods (with statistics), Grey Relational Analysis, TOPSIS, and

AHP (joint weighting + statistical verification) analysis methods are preferred [18-21].

3. GENERAL EVALUATION OF THE LITERATURE

As a result, studies conducted in the early 1900s were generally empirical and focused primarily on variables such as tool life and cutting speed. The term "statistical analysis" did not include methods such as "design of experiments (DOE) + ANOVA + Taguchi" in its current sense. As we approach the 20th century, studies using the modern term, i.e., "multivariate design of experiments + statistical analysis," appear to have largely begun in the 1990s and later. The literature systematically examining machinability in milling, turning, grinding, and drilling operations using statistical methods has increased since the 2000s, particularly on alloys and hard materials.

When evaluated overall, this research reveals the historical development of the concept of machinability and the critical role statistical methods have played in this field, particularly since the late 20th century. Empirical studies focusing on the relationship between tool life and cutting speed in the early 1900s gave way to multivariate experimental designs and modern statistical approaches such as ANOVA, Taguchi, and RSM from the 1990s onward. By the 2000s, statistical optimization techniques for modeling surface roughness, tool life, and cutting forces in difficult-to-machine materials had become widespread; process capability analyses, multi-output optimization, reliability, and multivariate assessments based on sensor data became important components of machinability research. Based on the information obtained, the following conclusions were drawn.

1. Expanded use of multivariate statistical models: In modern manufacturing processes, multiple outcomes such as surface roughness, energy consumption, and vibration should be evaluated together. PCA, PLS, MANOVA, and Gaussian Process models are suitable for this purpose.
2. Continuing DOE-based optimization: Designs such as Taguchi, Box–Behnken, D-optimal, and RSM should be used more systematically in future studies to understand material-tool-process interactions.
3. Expanding reliability and tool life analyses: Weibull distribution, accelerated life tests, and right-censored data analyses should be applied more widely, especially for hard materials.
4. Integration of sensor data: Real-time machinability prediction systems can be developed by combining sensor-based signals such as vibration,

acoustic emission, electrical current, and cutting force with statistical methods.

5. Shifting to machine learning and hybrid methods: In addition to traditional statistical models, regression trees, Gaussian Process, ANFIS, gray relational analysis, and multi-objective decision-making techniques, along with hybrid structures, can provide higher accuracy.
6. Routine process capability analyses: Cp, Cpk, Pp, Ppk, and Gage R&R analyses should be a standard part of processability assessments in production lines.

REFERENCES

1. Astakhov, V.P., *Machinability: existing and advanced concepts.* Machinability of advanced materials, 2014: p. 1-56.
2. Taylor, F.W., *On the art of metal cutting.* Trans. ASME, 1907. **28**: p. 31-35.
3. Deming, W.E., *Walter A. Shewhart, 1891-1967*. 1968, JSTOR.
4. Cobb, H.M., *The naming and numbering of stainless steels.* Advanced Materials Processes, 2007. **165**(9).
5. Jones, F.D., et al., *Machinery's handbook.* 2004.
6. Paul, E., J.T. Black, and A.K. Ronald, *Materials and Processes in Manufacturing. PrenticeHall*. 2003: PRENTICE-HALL, Incorporated.
7. Schneider, G.J.A.M., *Machinability of metals.* 2009.
8. Konig, W., et al., *A survey of the present state of high speed grinding.* 1971. **19**(2): p. 275-284.
9. Peklenik, J., *Modern methods of system analysis and production engineering research*. 1971.
10. Tlusty, J. and F.J.A.o.t.C. Koenigsberger, *New concepts of machine tool accuracy.* 1971. **19**(2): p. 261-273.
11. Choudhury, I.A., *Machinability studies of high strength materials and the development of a data base system*. 1995, Dublin City University.
12. E. Nas and S. Uzuner, "Optimization of Laser Cutting Parameters for Enhanced Surface Quality and Reduced Kerf Width in AISI 304 Stainless Steel," *Gazi J. Eng. Sci.*, vol. 9, no. 3, pp. 654–662, Jan. 2024, doi: 10.30855/gmbd.0705096.
13. E. Zurnacı, S. Uzuner, and E. Nas, "Comparison of Automation-Supported and Conventional Methods for Measuring Energy Consumption in Computer Numerical Control Machining," *Machines*, vol. 13, no. 2, p. 148, Feb. 2025, doi: 10.3390/machines13020148.
14. E. Zurnacı, "Optimization of 3D Printing Parameters to Mechanical Strength Improvement of Sustainable Printing Material Using RSM," *Int. J. 3D Print. Technol. Digit. Ind.*, vol. 7, no. 1, pp. 38–46, Apr. 2023, doi: 10.46519/ij3dptdi.1231076.
15. Montgomery, D.C., *Design and analysis of experiments*. 2017: John wiley & sons.
16. Myers, R.H. and D.C. Montgomery, *Response surface methodology*. 1996, Taylor & Francis.
17. Montgomery, D.C., *Introduction to statistical quality control*. 2020: John wiley & sons.

18. Durakovic, B.J.P.o.E. and N. Sciences, *Design of experiments application, concepts, examples: State of the art.* 2017. **5**(3): p. 421-439.
19. S. Jebarose Juliyana *et al.*, “Optimization of Wire EDM Process Parameters for Machining Hybrid Composites Using Grey Relational Analysis,” *Crystals*, vol. 13, no. 11, p. 1549, Oct. 2023, doi: 10.3390/cryst13111549.
20. B. Banerjee, K. Mondal, S. Adhikary, S. Nath Paul, S. Pramanik, and S. Chatterjee, “Optimization of process parameters in ultrasonic machining using integrated AHP-TOPSIS method,” *Mater. Today Proc.*, vol. 62, pp. 2857–2864, 2022, doi: 10.1016/j.matpr.2022.02.419.
21. A. T. Abbas, N. Sharma, Z. A. Alsuhaibani, A. Sharma, I. Farooq, and A. Elkaseer, “Multi-Objective Optimization of AISI P20 Mold Steel Machining in Dry Conditions Using Machine Learning—TOPSIS Approach,” *Machines*, vol. 11, no. 7, p. 748, Jul. 2023, doi: 10.3390/machines11070748.

Chapter 4

DEEP LEARNING APPROACHES IN BIOINFORMATICS FOR COMPUTER ENGINEERING: CONCEPTS, TOOLS, AND A CASE STUDY ON PROTEIN CLASSIFICATION

Ali Burak ÖNCÜL[1]

1. INTRODUCTION

The Human Genome Project and similar genome projects, along with supporting projects for the analysis and production of proteins, enzymes, and other genetic resources, as well as sequencing initiatives for various organisms and other protein sources, have generated biological data on an unprecedented scale. The intense need to analyze and interpret this vast data pool is being met by the rapidly developing field of bioinformatics. Bioinformatics refers to the use of computational methods and analytical tools in the acquisition, organization, and interpretation of biological data. While bioinformatics originates from biology and genetics in terms of its data source, it is an interdisciplinary field that combines computer science, mathematics, statistics, and biology. Today, bioinformatics has become an integral part of data management in modern biology and medicine [1]. Figure 1 illustrates the general structure and interdisciplinarity of bioinformatics.

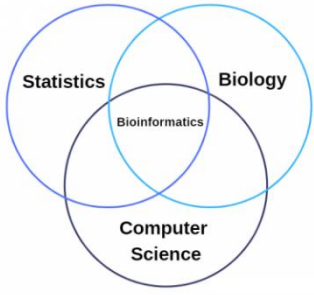

Figure 1. The multidisciplinary nature of bioinformatics and the disciplines it encompasses [2].

[1]Asst. Prof. Dr., Department of Computer Engineering/Faculty of Engineering and Architecture, Kastamonu University, Turkey, boncul@kastamonu.edu.tr, (ORCID: 0000-0001-9612-1787)

Considering a section of the field of bioinformatics, it is clear that numerous different amino acid sequences have been discovered in various databases and research studies. These sequences belong to different protein families, species, and even biological kingdoms. While some of these have been classified or labeled by experimental methods, despite the breadth of existing studies, a significant number remain unclassified or unlabeled [3]. The methods frequently used to analyze these structures can be broadly divided into two categories: biologically based and bioinformatics-based. The first and most traditional of these methods, biological experiments, involve studies conducted in a laboratory environment, with the primary directors and decision-makers being broadly competent in their fields, utilizing a variety of chemicals and solutions [4]. Traditional biological methods for classifying proteins based on amino acid sequences can tend to classify proteins into distinct classes that function with only minor variation in different organisms or species. However, detailed analysis at the sequence level reveals that many of these proteins are highly similar and share a large amount of structural commonality [3]. Bioinformatics, the second and most innovative of these methods, plays a significant role in solving these nuances and problems, and is an effort to achieve joint progress by combining various fields of biology, especially molecular biology, with the power of computer science [4]. These studies can be categorized as storing and utilizing data from biological experiments in databases, as well as utilizing general-purpose and sequence search tools, statistically based classifiers, and sequence alignment tools, including machine learning, artificial neural network, and deep learning-based artificial intelligence studies.

Just as humans communicate with each other verbally and in writing through languages, living organisms must use DNA, RNA, and proteins as communication tools for communication and organization within their bodies. Just as understanding the structure and rules of a language is necessary for effective communication, understanding the communication of organisms in plants, animals, and other kingdoms requires an understanding of the structures and types of these proteins. Biological experiments and studies were initially used to learn these structures. This allowed us to learn specific structures and functions, and classifications could be made based on this knowledge [3]. Of course, the methodology of these classifications was costly and relatively time-consuming. Furthermore, these human-made studies are prone to researcher-induced errors.

In addition, it is virtually impossible to classify these proteins obtained from biological studies solely by visually examining their lettered sequences. These

sequences attracted the attention of researchers working in the field of computer science and became the source and inspiration for statistically based studies. Additionally, some statistically based and artificial intelligence-based studies were carried out in the field [5].

Artificial intelligence (AI) refers to computational systems that can perform tasks that typically require human cognitive abilities, such as perception, reasoning, and decision-making [6]. Machine learning (ML), a fundamental subfield of artificial intelligence, focuses on algorithms that learn from data and improve their performance on a specific task without being explicitly programmed with hand-crafted rules [7]. Classical machine learning algorithms, including support vector machines, random forests, gradient boosting methods, and hidden Markov models, have been widely adopted in bioinformatics for tasks such as gene expression-based classification, protein family prediction, motif discovery, and disease subtype identification [8], [9], [10], [11]. These approaches often rely on hand-crafted features: domain experts automatically convert biological information into numerical descriptors with prepared preprocessing codes, which are then fed into learning algorithms. While effective in many settings, this pipeline can become a bottleneck when the underlying biological mechanisms are only partially understood or when the data dimensionality is extremely high.

Deep learning (DL) represents a more recent evolution within machine learning, based on multilayer neural networks that can automatically learn hierarchical feature representations from data [6], [7]. Figure 2 illustrates the relationship between artificial intelligence, machine learning, and deep learning.

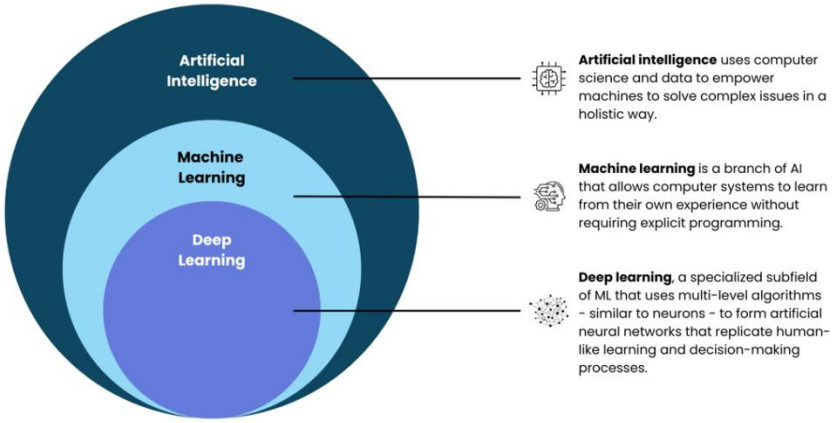

Figure 2. Artificial intelligence, machine learning and deep learning [12].

By stacking multiple nonlinear transformations, deep architectures can model complex, multi-scale relationships in biological sequences, structures, and networks. Convolutional neural networks (CNNs) have been successfully applied to DNA, RNA, and protein sequence data to detect regulatory motifs, binding sites, and functional regions directly from one-dimensional sequence representations [13], [14]. Recurrent neural networks (RNNs) and their variants, such as long short-term memory (LSTM) networks and gated recurrent units (GRUs), are particularly well-suited to capturing long-range dependencies in sequential biological data, which is critical for modeling splicing signals, RNA secondary structure, long-range protein interactions, and for classifying protein sequences [9], [15], [16]. Recently, attention mechanisms and transformer-based models, originally developed for natural language processing, have enabled the development of powerful "protein language models" that learn contextual placements of amino acid sequences and support downstream tasks ranging from secondary structure prediction to functional annotation [17]. CNN and GRU models were utilized in a study that identified vesicular transport proteins [18]. A bidirectional LSTM model was used in a study on remote protein homology detection, which plays a vital role in protein structure and function [19]. Deep Neural Networks (DNN), LSTM, and CNN networks were used on a high-capacity dataset such as Swiss-Prot, and these models have emerged in protein classification [20].

The impact of AI and DL on structural bioinformatics has been particularly striking. Deep residue- and transformer-based architectures have fundamentally improved protein structure prediction, residue-residue contact prediction, and interresidue distance modeling, resulting in highly accurate end-to-end systems such as AlphaFold [17]. These models combine evolutionary information, sequence profiles, and learned representations to approximate the complex mapping from amino acid sequence to three-dimensional structure, achieving accuracies previously unattainable by traditional physics-based or homology-based methods [17].

Representation learning techniques inspired by natural language processing (such as k-mer embeddings and biological Word2Vec-like models) allow mapping DNA and protein sequences onto continuous vector spaces and capture local and global context to improve subsequent classification tasks [16], [21]. These embedding-based approaches have been shown to improve performance in protein family classification, enzyme function prediction, antimicrobial peptide identification, and variant pathogenicity assessment compared to traditional one-hot or simple k-mer frequency encodings [11], [16], [21].

From a practical perspective, AI-driven methods in bioinformatics are expanding into a wide range of application areas. In genomics, ML and DL are used to identify promoters, enhancers, and other regulatory elements; to predict transcription factor binding; and to prioritize non-coding variants with potential pathogenic effects [13], [14]. In proteomics and protein informatics, sequence- and structure-based models support functional annotation, subcellular localization prediction, stability prediction, and interaction partner discovery [9], [10], [17]. In systems biology and precision medicine, AI models help stratify patients into clinically meaningful subgroups, predict treatment response, and discover biomarkers by uncovering hidden patterns in high-dimensional patient groups [8].

Despite their success, AI and DL methods in bioinformatics also present several challenges. Large and well-annotated datasets are often required to fully utilize high-throughput models; However, many biological problems suffer from limited labeled data and significant class imbalance [9]. Furthermore, issues such as overfitting, data leakage, batch effects, and distribution shifts can seriously compromise the generalizability of learned models if not carefully addressed [8], [9].

In summary, artificial intelligence, machine learning, and learning-teaching have become pillars of modern bioinformatics, enabling the extraction of biologically meaningful patterns from increasingly complex and large-scale datasets. These methods have reshaped how we approach problems in genomics, proteomics, structural biology, and systems biology by moving beyond hand-designed features and leveraging data-driven representation learning. In the remainder of this section, we build on this conceptual foundation to examine specific AI tools and models used in bioinformatics and present a comparative study of different sequence representation strategies, such as code dictionary and Word2Vec-based embeddings, in protein and DNA classification tasks.

2. EXPERIMENTAL STUDIES

In light of the challenges outlined in the literature and previous studies, deep learning models have demonstrated exceptional success in the field. When determining models and tools for future studies in the field, the structure of bioinformatics data must be taken into consideration. From this perspective, genetic and molecular communication mechanisms in living organisms can be likened to communication through language in human society; however, the "language" used here is an extremely complex biochemical dictionary composed of nucleic acids and proteins. For an organism to sustain its vital

processes, the information encoded in DNA sequences must be transmitted via RNA and ultimately become functional in the three-dimensional structures of proteins. Just as humans must know the syntax, semantics, and rules of a language to understand it, understanding all biological processes in plants, animals, and microorganisms requires a detailed understanding of the primary, secondary, and tertiary structures of proteins; amino acid sequence motifs; evolutionary conservation patterns; and functional domains [3].

However, such experimental approaches are both costly and time-consuming; Furthermore, human errors in sample preparation, measurement precision, and interpretation can be a significant source of variability. Furthermore, as biodiversity increases and the capacity of sequencing technologies grows exponentially, it has become practically impossible for experimental methods alone to characterize the entire protein universe comprehensively. Indeed, millions of proteins have been sequenced today, but a significant portion of them remain unclassified, and their structures and functions remain undetermined. Therefore, the use of computational methods, particularly artificial intelligence and deep learning-based models, alongside experimental biology, has become an essential requirement for understanding the structural and functional properties of proteins [22]. Therefore, the concepts of amino acids and proteins must first be clarified and the data used must be understood.

2.1. Amino Acid and Protein

Proteins are macromolecules composed of amino acids that play a crucial role in many functions in biological systems. Amino acids, the smallest building blocks of proteins, peptides, and enzymes, are small molecules with a carboxyl group at one end and an amino group at the other, and their side chains carry neutral, polar, or ionizable groups. Many amino acids and their derivatives serve various functions in metabolism in living organisms [23].

Amino acids are the smallest building blocks of proteins, peptides, and enzymes. They are small molecules with a carboxyl group at one end, and an amino group at the other, and their side chains carry neutral, polar, or ionizable groups. Many amino acids and their derivatives serve various functions in metabolism in living organisms. Proteins are macromolecules composed of amino acids arranged in specific and varying sequences [23]. A representative three-dimensional image of a protein is shown in Figure 3.

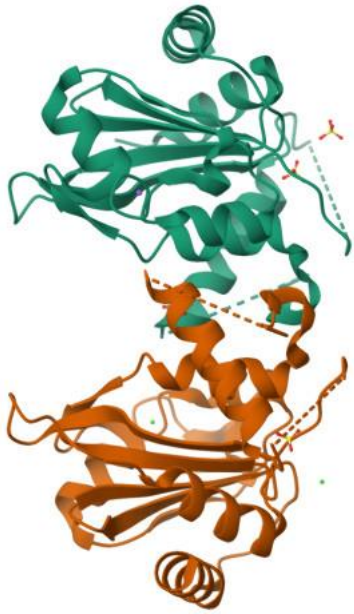

Figure 3. A sample three-dimensional protein image.

Although more than 300 amino acids exist in nature, only 20 of these are encoded by DNA and are found in the mammalian and plant kingdoms. Proteins, formed by the sequence of these amino acids linked by peptide bonds, are macromolecules responsible for carrying out essential vital functions in all organisms. Different sequences of these amino acids form different proteins, while similar sequences form the defining motifs of specific protein families [24].

The transcription factor proteins used in this section are specialized types of proteins that play a crucial role in the process from DNA to RNA and subsequently to protein production, controlling the flow of information throughout this process [25], [26]. The plant transcription factors data set used in this study was downloaded from the Plant Transcription Factor Database (PlantTFDB) [27].

2.2. Structure and Representation of Protein Sequences

Each unique amino acid combination in protein sequences represents a structurally and functionally distinct protein. These linear sequences contain the fundamental information that determines the three-dimensional conformations of proteins, allowing each protein to develop its own unique folding order and biological function [24]. While the uniqueness of each sequence implies that the

protein itself will also be unique, certain conserved regions within these sequences—motifs—are often the fundamental elements that characterize a given protein family or species. Just as words in natural languages are represented by letters, protein sequences are represented by single-letter amino acid codes for analysis and visualization. Despite their overall sequence differences, sequences containing the same motifs are often considered to belong to the same protein family or class [28].

Protein families a.k.a classes, are determined by the motifs within protein sequences. The number of amino acids within a motif and their sequences vary. Given that each amino acid position within a motif contains one or more amino acids, each motif contains a vast number of combinations, and each protein family has a different motif. This highlights the impossibility of predicting protein classes without the use of biological experiments or artificial intelligence applications. Statistical or neural network-based artificial intelligence applications utilize precisely this probability calculation for their analyses. Consequently, artificial intelligence methods offer advantages in terms of both time and speed. Figure 4 illustrates a protein representation in a dataset from PlantTFDB.

```
>KFK36254.1 Arabis alpina|G2-like|G2-like family protein
MYSAIRSLPVDGSMGEYSDGTNLPIEACLVLTTDPKPRLRWTTELHDRFVDAVTQLGGPD
KATPKTIMRTMGVKGLTLYHLKSHLQKFRLGRLPCKESTDNSKDVSSVAESQDTGSSTTS
SLRLAAQEQKESYQVTEALRAQMEVQRRLHEQLEVQQRLQLRIEAQGKYLQTILEKACKA
IEEQAVAFAGLEAAREELSELAIKVSNGCQSTFDTTKMTIPSLSELAVAIEHKNNCSAES
SLTSSTVGSPVSAAMMKKRHRGVFGNGDSVVVGHEAGWVMPSSSIG
>KFK25038.1 Arabis alpina|GeBP|GeBP family protein
MAPKHTDTIQNPPMPSSSSEEESASSGEDSDSSKKHNSASDSDPIKTKIVVTKPESSGSM
KTTTKSSVVVAEPESTTAKRPLKETEEDVEVKKKKMKTELVMKNQEPEEKVSGDETKKQL
MFQRLFSENDEIALLQGILDFTSTRGDPYEKMDVFCEYVKKLINFDANKSQLVTKIRRLK
KKFGNTIKNSLKKGKSEDEIVFSKDLDQKAFHLSRKVWGSNGVLASKSRKKLGENSKEII
KKEEKPKQNVVSVCRSSSEGGEIASFFKAENTTAFGLDEPTVAARWEMVSDVAKKREMEE
KLKKLKATQEELCLQRTGIVADTVKLIFNDNASSSSK
>KFK35037.1 Arabis alpina|bZIP|bZIP family protein
MTTTTTPHWPDFSSQKLPSIAATAAATAATAGQNQQNQNPSWMDEFLDFSATRRGTHRRS
ISDSIAFLEAPSSGVGNHHHHFDRFDDEQFMSMFNDDVHQNHNNHNNNHHHHHHNVGHTR
SSSNTSTPSDHNSLSDEDNNNNKEPLPSDHDHHMENNNVDNDKNNVAGNNYNESDEVQSQ
CKTEPQDGPSSANQNSGGSSGNRIHDPKRVKRILANRQSAQRSRVRKLQYISELERSVTS
LQTEVSVLSPRVAFLDHQRLLLNVDNSAIKQRIAALAQDKIFKDAHQEALKREIERLRQV
YHQQSLKKMENSNVSDQSPVDIKPSVEKEQLLNA
```

Figure 4. Protein representation form PlantTFDB dataset [27].

In Figure 4, each section, starting with the ">" character and continuing until the next ">" character, belongs to a protein sequence. The line starting with ">" in this section contains descriptive information, including the protein's class

information (the expression between two "|" characters), while the subsequent lines contain the character representation of the protein sequence. This dataset file contains information beyond the protein sequences and their classes. Since this study, prepared for classification purposes, aims to use only protein sequences and their classes, the necessary information must be extracted from the dataset file to obtain the final dataset file. To obtain the final dataset file, the Python programming language library Biopython [29], which is developed for analyzing specially formatted FASTA files, was used. Figure 5 shows the dataset file to be used.

```
family  sequence
G2-like MYSAIRSLPVDGSMGEYSDGTNLPIEACLVLTTDPKPRLRWTTELHDRFVDAVTQLGGPDKATPKTIMRTMG
VKGLTLYHLKSHLQKFRLGRLPCKESTDNSKDVSSVAESQDTGSSTTSSLRLAAQEQKESYQVTEALRAQMEVQRRLHEQ
LEVQQRLQLRIEAQGKYLQTILEKACKAIEEQAVAFAGLEAAREELSELAIKVSNGCQSTFDTTKMTIPSLSELAVAIEH
KNNCSAESSLTSSTVGSPVSAAMMKKRHRGVFGNGDSVVVGHEAGWVMPSSSIG
GeBP    MAPKHTDTIQNPPMPSSSSEEESASSGEDSDSSKKHNSASDSDPIKTKIVVTKPESSGSMKTTTKSSVVVAE
PESTTAKRPLKETEEDVEVKKKKMKTELVMKNQEPEEKVSGDETKKQLMFQRLFSENDEIALLQGILDFTSTRGDPYEKM
DVFCEYVKKLINFDANKSQLVTKIRRLKKKFGNTIKNSLKKGKSEDEIVFSKDLDQKAFHLSRKVWGSNGVLASKSRKKL
GENSKEIIKKEEKPKQNVVSVCRSSSEGGEIASFFKAENTTAFGLDEPTVAARWEMVSDVAKKREMEEKLKKLKATQEEL
CLQRTGIVADTVKLIFNDNASSSSK
bZIP    MTTTTTPHWPDFSSQKLPSIAATAAATAATAGQNQQNQNPSWMDEFLDFSATRRGTHRRSISDSIAFLEAPS
SGVGNHHHHFDRFDDEQFMSMFNDDVHQNHNNHNNNHHHHHHNVGHTRSSSNTSTPSDHNSLSDEDNNNNKEPLPSDHDH
HMENNNVDNDKNNVAGNNYNESDEVQSQCKTEPQDGPSSANQNSGGSSGNRIHDPKRVKRILANRQSAQRSRVRKLQYIS
ELERSVTSLQTEVSVLSPRVAFLDHQRLLLNVDNSAIKQRIAALAQDKIFKDAHQEALKREIERLRQVYHQQSLKKMENS
NVSDQSPVDIKPSVEKEQLLNA
ERF MEGERHDSTTSSSRKRSHEPAEERPASHVATMAFKEKPYRGIRMRKWGKWVAEIREPNKRSRLWLGSYTTAVAAAR
AYDTAVFYLRGPSARLNFPDLLVQEGDRRSAAAADMPAALIREKAAEVGARVDALLASADPAAHSSSLPVLVEKPDLNKI
PESGDI
```

Figure 5. A fragment of the prepared dataset file

An examination of the simplified dataset revealed 58 classes and 132330 different protein sequences. Before being subjected to a series of preprocessing methods, this dataset was randomly split into 70% training, 15% validation, and 15% test sets, to be used for model training, validation, and test [11], [16].

2.3. Data Preprocessing

Although the dataset has been simplified and contains only the desired data, it is not yet ready to be fed into a deep learning or any other artificial intelligence model. This is because deep learning and other models require digitized data to process the data and complete the training process. This study examines and compares two different preprocessing methods based on their structure, success, and efficiency.

The first of the preprocessing methods mentioned is the code dictionary method [22]. As mentioned in the previous section, 20 amino acids are commonly found in the plant kingdom. These two amino acids are represented by letters, as shown in Figures 4 and 5. If the dataset is to be digitized,

numerical equivalents must be used for the amino acids represented by these letters. In this process, assigning numerical equivalents from 1 to 20 to each amino acid is sufficient to digitize the sequences. This assignment digitizes the sequences, making them nearly ready to be fed to the deep learning model.

One of the key factors determining the success of deep learning models, particularly in the preprocessing phase, is that each input data set must be of equal size. However, because protein sequences have different structures, their lengths also vary. Equalizing the sizes of protein sequences of these varying lengths is only possible after certain analyses. One of the most important analyses is examining the distribution of sequences according to their size and then applying the size equalization method. The length distributions of the sequences in each part of the dataset, which was randomly divided into three parts for training, validation, and test of the model, are given in Figure 6.

Figure 6. Frequencies of sequences by length.

Examining the graphs, it was observed that the string lengths in all three parts of the dataset were concentrated at a maximum of approximately 450 characters. Therefore, the fixed string length was planned to be 450 characters. Shorter strings were then lengthened by adding zeros at the end, while longer strings were shortened at the end. With this process, the dataset was now ready to be fed to the model, meeting all the requirements.

The first of the preprocessing methods mentioned is the Word2Vec vector representation method, which has become increasingly popular following the code dictionary method. Word2Vec is a prediction-based unsupervised learning model that represents words in a vector space and performs proximity analysis. The Word2Vec model has two different architectures: Continuous Bag-of-Words (CBOW) and Continuous Skip-Gram. CBOW aims to predict the target word by examining the words before and after it according to the window size, whereas Skip-Gram, unlike CBOW, is based on the principle of predicting neighboring words based on the target word [30]. In this method, single-piece protein sequences should be divided into words (k-mers) in accordance with the Word2Vec model's design. Here, because the similarities between each word

and other words influence the vector representation, the aim is to achieve higher success compared to the previous code dictionary method by estimating the relationships between amino acids and thus capturing motif information. When separating the sequences into words, one character was skipped, resulting in three separate sequences from each sequence. This aimed to obtain as much information about the motifs as possible [21]. A visual representation of the k-mer generation process is given in Figure 7.

```
SEQUENCE:
MYSAIRSLPVDGSMGEYSDGTN...

K-MERS:
MYS, AIR, SLP, VDG, SMG, EYS, DGT, ...
YSA, IRS, LPV, DGS, MGE, YSD, GTN, ...
SAI, RSL, PVD, GSM, GEY, SDG, TNL, ...
```

Figure 7. Preparing k-mers from sequences

Wor2Vec's vector representations were used to digitize the prepared words. One aspect that distinguishes Word2Vec over the previous method is that, during model implementation, the weights of the Word2Vec model are assigned as initial weights to the deep learning model. The information in Figure 6 was used to determine the length of the data processed with Word2Vec. Given that the average length of the sequences is 450 and that each k-mer consists of three characters, the protein sequences divided into k-mers were determined to be 150 in length. The dimensionality equalization principles were implemented in the same manner as the previous method. The datasets, prepared using two different preprocessing methods, were ready to be fed to the prepared deep learning model.

2.4. Deep Learning Models

Recurrent Neural Networks (RNNs), used in sequential, long-term, one-dimensional tasks such as speech recognition and analysis, language processing, and translation, have experienced relatively low performance due to the vanishing gradient. Long Short-Term Memory (LSTM) network has become increasingly popular in bioinformatics data. These models, which have yielded very successful results in studies such as predicting the previous and next parts in time series and sequential data, were actively used in this study because they are also expected to yield successful results in bioinformatics data and the datasets in this study due to their structure [6].

2.4.1. Long Short-Term Memory (LSTM)

Because the vanishing or exploding gradients in classical RNNs make it difficult to learn long-term dependencies, the addition of a decision-making control mechanism to the architecture became necessary. Gate-based memory structures developed for this purpose allowed the preservation of long-term context information in sequences [31]. These gates provide a process similar to biological learning, ensuring that important information is retained and unimportant information is discarded [6].

The Long Short-Term Memory (LSTM) architecture, a direct result of this approach, defines input, forget, and output gates in addition to the RNN's tanh-based state update [31]. The addition of a forget gate in the LSTM was suggested by Gers et al. [32], [33] because it enables a more stable learning process by resetting the cell state when necessary. A sigmoid activation function is used to control the information flow in the 0–1 range at each gate [34]. Figure 8 illustrates the internal structure of an LSTM cell.

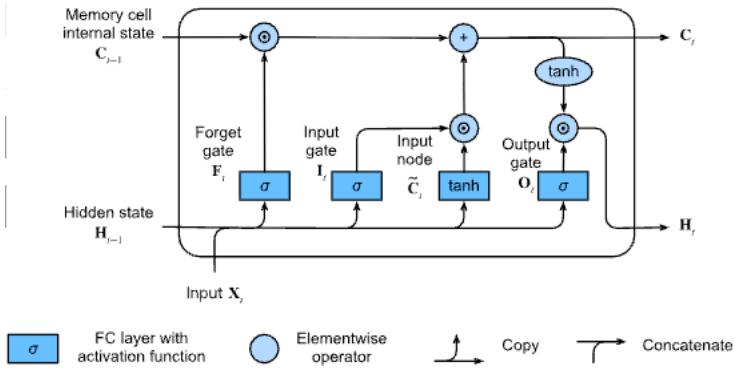

Figure 8. Internal structure of an LSTM cell [35].

Below are the basic gate equations of LSTM:

- Forget Gate:

$f_t = \sigma(W_f \cdot [h_{t-1}, x_t] + b_f)$

- Input Gate:

$i_t = \sigma(W_i \cdot [h_{t-1}, x_t] + b_i)$

- Candidate Cell State:

$\hat{c}_t = \tanh(W_c \cdot [h_{t-1}, x_t] + b_c)$

- Cell State Update:

$c_t = f_t \odot c_{t-1} + i_t \odot \hat{c}_t$

- Output Gate:

$o_t = \sigma(W_o \cdot [h_{t-1}, x_t] + b_o)$

- Hidden State:

$h_t = o_t \odot \tanh(c_t)$

In here;

- σ represents the sigmoid activation function,
- ⊙ represents the element-wise product,
- h_t represents the hidden state,
- c_t represents the cell state,
- x_t represents the input vector.

Because the data set has a multi-class structure, The Softmax activation function is a nonlinear transformation commonly used in binary or multi-class classification problems. This function, frequently used in probability-based decision-making processes, produces a probability distribution over a set of classes and normalizes each output to the interval [0,1], ensuring that its sum is 1 [36]. Softmax is often used as the standard output activation function in the classification phase of fully connected layers in deep learning models, as it enables the calculation of the probability that an example belongs to each class. The formula for the Softmax activation function is as follows [37]:

$$f(x) = \frac{e^{x_i}}{\sum_{j=1}^{j} e^{x_j'}} \text{ , } \forall_i = [1, j]$$

Accurcy, precision, recall, and f-score metrics were used to evaluate model results. The equation for each of these metrics is as follows:

- $Accuracy\ (Acc) = \frac{TP+TN}{TP+FP+FN+TN}$
- $Precision\ (Pre) = \frac{TP}{TP+FP}$
- $Recall\ (Re) = \frac{TP}{TP+FN}$
- $F - Score\ = \frac{2 \cdot TP}{2 \cdot TP+FP+FN}$

3. EXPERIMENTAL RESULTS AND EVALUATION

As described in previous sections, in previous study [11], [16] a dataset consisting of sequences digitized to equal length using a code dictionary and a dataset consisting of sequences divided into words and vectorized using Word2Vec were processed using a hybrid deep learning model, the design details and layers of which are listed in Table 1.

Table 1. Layers of the deep learning model.

Layer	Type
Embedding	Embedding
Bidirectional LSTM	Bidirectional
Bidirectional LSTM	Bidirectional
Dense (58)	Dense (Classifier)

The model was trained separately using a dataset that had been processed with two different preprocessing methods. Training and validation results, as well as graphs, were generated and evaluated using the success metrics and graphs specified in the previous section.

The models prepared using code dictionary preprocessing and Word2Vec preprocessing were run in Jupyter Notebook on the Google Colab platform. In the code dictionary preprocessed model, the dataset was used with a fixed sequence length of 450, whereas in the Word2Vec preprocessed model, the dataset was used with a fixed length of 150, which technically represents the same number of sequences. An early stopping function was used to maximize model performance. Table 2 shows the test results and running times of the models according to the evaluation metrics.

Table 2. Layers of the deep learning model [11], [16].

Model	Accuracy (%)	Precision (%)	Recall (%)	F-score (%)	No. of epoch
Code Dict.	97.49	95.42	95.33	95.32	26
Word2Vec	97.80	97.10	96.31	96.60	12

Table 3 shows the train accuracy, train loss, validation accuracy, and validation loss values at the end of the first epoch for the same models with two different preprocessing methods [11], [16].

Table 3. Comparison of code dictionary versus Word2Vec with same model.

Model	Train Acc.	Train Loss	Val. Acc.	Val. Loss.
Code Dict.	0.2519	2.8305	0.3770	2.2621
Word2Vec	0.7017	1.1427	0.884	0.3897

Figure 9 shows the result graphs for the code dictionary model, and Figure 10 shows the result graphs for the Word2Vec model [11], [16].

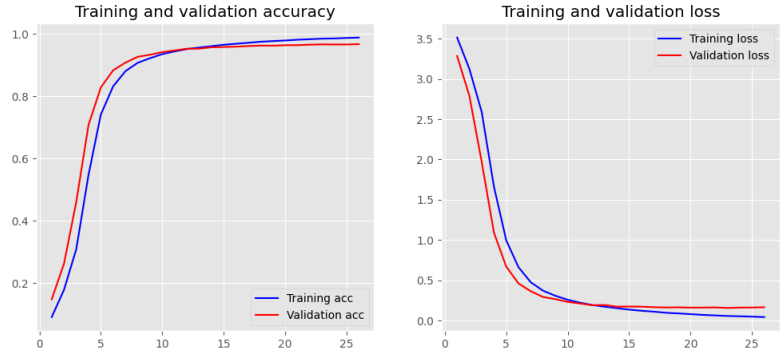

Figure 9. Code Dictionary model result graphs.

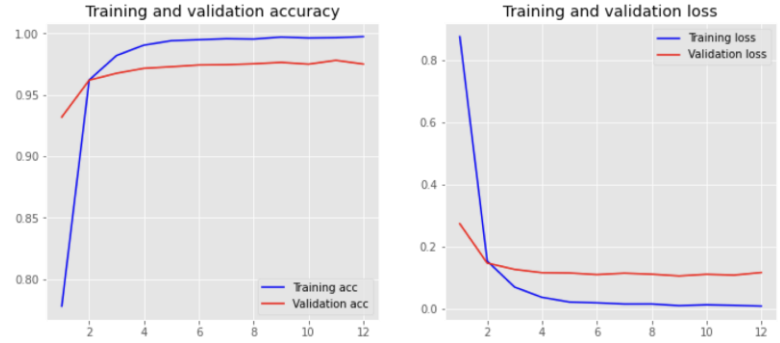

Figure 10. Word2Vec model result graphs.

When Table 2 is examined, the Word2Vec model, a preprocessing model that performs proximity analysis of words, namely amino acid groups, clearly leads in every metric, thanks to this proximity analysis. Furthermore, it completed training in fewer epochs, and each epoch took approximately half the time of the code dictionary model. Furthermore, the Word2Vec preprocessing model, which uses a shorter sequence length, stands out as being both successful, fast, and efficient in every respect. Indeed, the metrics at the end of the first epoch, as shown in Table 3, clearly demonstrate this success. The validation accuracy value is particularly prominent. The graphs in Figures 9 and 10 clearly reinforce the Word2Vec model's success in all metrics and timeframes [11], [16], [38].

When all this data is examined, the more innovative and explicitly knowledge-based models are generally successful, fast, and efficient. This efficiency is achieved not only through reduced human waiting times and added value to the relevant field, but also by reducing resource and electricity consumption, as well as computer cooling energy consumption, resulting in outcomes that are more beneficial to nature and life, although not necessarily the most beneficial.

REFERENCES

[1] A. Bayat, 'Science, medicine, and the future: Bioinformatics', *BMJ*, vol. 324, no. 7344, pp. 1018–1022, Apr. 2002, doi: 10.1136/bmj.324.7344.1018.

[2] B. McBride, 'What is Bioinformatics – Overview and Examples', Fios Genomics. Accessed: Sep. 02, 2025. [Online]. Available: https://www.fiosgenomics.com/what-is-bioinformatics-overview-and-examples/

[3] D. Petrey and B. Honig, 'Is protein classification necessary? Toward alternative approaches to function annotation', *Curr Opin Struct Biol*, vol. 19, no. 3, pp. 363–368, Jun. 2009, doi: 10.1016/J.SBI.2009.02.001.

[4] M. Huerta, F. Haseltine, Y. Liu, G. Downing, and B. Seto, 'NIH working definition of bioinformatics and computational biology', Jul. 2000.

[5] P. Baldi and S. Brunak, *Bioinformatics, Second Edition: The Machine Learning Approach*. Cambridge: MIT Press, 2001.

[6] Y. LeCun, Y. Bengio, and G. Hinton, 'Deep learning', *Nature*, vol. 521, no. 7553, pp. 436–444, May 2015, doi: 10.1038/nature14539.

[7] C. M. . Bishop, *Pattern recognition and machine learning*. Springer Science + Business Media, 2009.

[8] S. Min, B. Lee, and S. Yoon, 'Deep learning in bioinformatics', *Brief Bioinform*, p. bbw068, Jul. 2016, doi: 10.1093/bib/bbw068.

[9] P. Larrañaga *et al.*, 'Machine learning in bioinformatics', *Brief Bioinform*, vol. 7, no. 1, pp. 86–112, Mar. 2006, doi: 10.1093/bib/bbk007.

[10] T. G. Dietterich, 'Machine Learning for Sequential Data: A Review', 2002, pp. 15–30. doi: 10.1007/3-540-70659-3_2.

[11] A. B. Öncül, 'Bitki Transkripsiyon Faktörlerinin Hibrit Derin Öğrenme ile Sınıflandırılması', 2022.

[12] S. Cherneha, 'What is Machine Learning: Concept, Types, Distinction with Artificial Intelligence (AI) and Deep Learning (DL)', Scrum Launch. Accessed: Sep. 12, 2025. [Online]. Available: https://www.scrumlaunch.com/blog/what-is-machine-learning-concept-types-distinction-with-ai-and-deep-learning

[13] B. Alipanahi, A. Delong, M. T. Weirauch, and B. J. Frey, 'Predicting the sequence specificities of DNA- and RNA-binding proteins by deep learning', *Nat Biotechnol*, vol. 33, no. 8, pp. 831–838, Aug. 2015, doi: 10.1038/nbt.3300.

[14] J. Zhou and O. G. Troyanskaya, 'Predicting effects of noncoding variants with deep learning–based sequence model', *Nat Methods*, vol. 12, no. 10, pp. 931–934, Oct. 2015, doi: 10.1038/nmeth.3547.

[15] A. Graves, A. Mohamed, and G. Hinton, 'Speech recognition with deep recurrent neural networks', in *2013 IEEE International Conference on Acoustics, Speech and Signal Processing*, IEEE, May 2013, pp. 6645–6649. doi: 10.1109/ICASSP.2013.6638947.

[16] A. B. Öncül and Y. Çelik, 'A hybrid deep learning model for classification of plant transcription factor proteins', *Signal Image Video Process*, vol. 17, no. 5, pp. 2055–2061, 2023, doi: 10.1007/s11760-022-02419-5.

[17] J. Jumper *et al.*, 'Highly accurate protein structure prediction with AlphaFold', *Nature*, vol. 596, no. 7873, pp. 583–589, Aug. 2021, doi: 10.1038/s41586-021-03819-2.

[18] N. Q. K. Le, E. K. Y. Yapp, N. Nagasundaram, M. C. H. Chua, and H. Y. Yeh, 'Computational identification of vesicular transport proteins from sequences using deep gated recurrent units architecture', *Comput Struct Biotechnol J*, vol. 17, pp. 1245–1254, Jan. 2019, doi: 10.1016/J.CSBJ.2019.09.005.

[19] S. Li, J. Chen, and B. Liu, 'Protein remote homology detection based on bidirectional long short-term memory', *BMC Bioinformatics*, vol. 18, no. 1, p. 443, 2017, doi: 10.1186/s12859-017-1842-2.

[20] K. S. Naveenkumar, B. R. Mohammed Harun, R. Vinayakumar, and K. P. Soman, 'Protein Family Classification using Deep Learning', *bioRxiv*, p. 414128, Jan. 2018, doi: 10.1101/414128.

[21] E. Asgari and M. R. K. Mofrad, 'Continuous Distributed Representation of Biological Sequences for Deep Proteomics and Genomics', *PLoS One*, vol. 10, no. 11, Nov. 2015.

[22] M. L. Bileschi *et al.*, 'Using deep learning to annotate the protein universe', *Nat Biotechnol*, vol. 40, no. 6, pp. 932–937, Jun. 2022, doi: 10.1038/s41587-021-01179-w.

[23] N. Acar, E. Gündeğer, and C. Selçuki, 'Protein Yapı Analizleri', in *Biyoinformatik Temelleri ve Uygulamaları*, 1st ed., M. C. Baloğlu, Ed., Kastamonu: Pegem Akademi Yayıncılık, 2018, ch. 5, pp. 85–128.

[24] D. R. Ferrier, 'Protein Yapısı ve İşlevi', in *Lippincott Biyokimya: Görsel Anlatımlı Çalışma Kitapları*, B. A. Jameson, Ed., İstanbul: Nobel Tıp Kitapevleri, 2019, ch. 1, pp. 1–68.

[25] D. S. Latchman, 'Transcription factors: an overview Function of transcription factors', *Int. J. Exp. Path*, vol. 74, pp. 417–422, 1993.

[26] M. Karin, 'Too many transcription factors: positive and negative interactions', *New Biol*, vol. 2, no. 2, pp. 126–131, 1990.

[27] J. Jin *et al.*, 'PlantTFDB 4.0: toward a central hub for transcription factors and regulatory interactions in plants', *Nucleic Acids Res*, vol. 45, no. D1, pp. D1040–D1045, Jan. 2017, doi: 10.1093/nar/gkw982.

[28] D. Ofer, N. Brandes, and M. Linial, 'The language of proteins: NLP, machine learning & protein sequences', *Comput Struct Biotechnol J*, vol. 19, pp. 1750–1758, Jan. 2021, doi: 10.1016/J.CSBJ.2021.03.022.

[29] B. Chapman and J. Chang, 'Biopython', *ACM SIGBIO Newsletter*, vol. 20, no. 2, pp. 15–19, Aug. 2000, doi: 10.1145/360262.360268.

[30] T. Mikolov, K. Chen, G. Corrado, and J. Dean, 'Efficient Estimation of Word Representations in Vector Space', Jan. 2013.

[31] K. Greff, R. K. Srivastava, J. Koutnik, B. R. Steunebrink, and J. Schmidhuber, 'LSTM: A Search Space Odyssey', *IEEE Trans Neural Netw Learn Syst*, vol. 28, no. 10, pp. 2222–2232, Oct. 2017, doi: 10.1109/TNNLS.2016.2582924.

[32] F. A. Gers, J. Schmidhuber, and F. Cummins, 'Learning to Forget: Continual Prediction with LSTM', *Neural Comput*, vol. 12, no. 10, pp. 2451–2471, 2000, doi: 10.1162/089976600300015015.

[33] G. Van Houdt, C. Mosquera, and G. Nápoles, 'A review on the long short-term memory model', *Artif Intell Rev*, vol. 53, no. 8, pp. 5929–5955, Dec. 2020, doi: 10.1007/s10462-020-09838-1.

[34] S. Hochreiter and J. Schmidhuber, 'Long Short-Term Memory', *Neural Comput*, vol. 9, no. 8, pp. 1735–1780, Nov. 1997, doi: 10.1162/neco.1997.9.8.1735.

[35] Dive Into Deep Learning, 'Long Short-Term Memory (LSTM)'. Accessed: Sep. 28, 2025. [Online]. Available: https://d2l.ai/chapter_recurrent-modern/lstm.html

[36] A. Basturk, M. E. Yuksei, H. Badem, and A. Caliskan, 'Deep neural network based diagnosis system for melanoma skin cancer', in *2017 25th Signal Processing and Communications Applications Conference (SIU)*, IEEE, May 2017, pp. 1–4. doi: 10.1109/SIU.2017.7960563.

[37] L. Parisi, D. Neagu, R. Ma, and F. Campean, 'Quantum ReLU activation for Convolutional Neural Networks to improve diagnosis of Parkinson's disease and COVID-19', *Expert Syst Appl*, vol. 187, p. 115892, Jan. 2022, doi: 10.1016/j.eswa.2021.115892.

[38] A. B. Oncul, Y. Celik, N. M. Unel, and M. C. Baloglu, 'Bhlhdb: A next generation database of basic helix loop helix transcription factors based on deep learning model', *J Bioinform Comput Biol*, Jun. 2022, doi: 10.1142/S0219720022500147.

Chapter 5

MECHANICAL AND BALLISTIC BEHAVIOR OF MONOLITHIC AND LAMINATED AL6061/B_4C COMPOSITES

Halil KARAKOÇ[1]

Abstract

In this study, monolithic and laminated Al6061/B_4C composites were fabricated via a powder metallurgy route combining semi-solid hot pressing and subsequent T6 heat treatment, and their microstructural, mechanical, and ballistic behaviors were systematically investigated. Three panel architectures were produced: a monolithic Al6061–50 wt.% B_4C composite, a bilayer laminate consisting of Al6061–50 wt.% B_4C/Al6061, and a bilayer laminate with Al6061–40 wt.% B_4C/Al6061. All configurations exhibited high relative densities (>99%) and a generally uniform distribution of B_4C particles within the matrix. Increasing B_4C content enhanced hardness and stiffness but promoted brittle fracture and reduced flexural toughness. Ballistic tests using 7.62 × 51 mm NATO M80 projectiles under NIJ Level III conditions revealed that the monolithic composite failed by complete perforation accompanied by extensive radial cracking and petalling, whereas the laminated plates effectively attenuated the projectile energy. In particular, the laminated architectures developed confined damage zones on the front face and smooth, non-catastrophic rear-face deformation. Among the investigated designs, the Al6061–40 wt.% B_4C/Al6061 laminate provided the most favorable balance between hardness, flexural performance, and ballistic energy absorption. These results demonstrate that tailoring reinforcement content within layered Al6061/B_4C architectures is an efficient strategy for improving damage tolerance and back-face integrity in lightweight armor applications.

Keywords: Al6061 matrix composites; B_4C reinforcement; laminated structures; microstructure; ballistic impact.

[1] Department of Mechanical Engineering, Hacettepe University, 06935 Ankara, Turkey
***Corresponding author**: Tel: +90 312 267 30 20; Fax: +90 312 267 33 38
E-mail address: halil.karakoc@hacettepe.edu.tr

1. Introduction

Aluminum matrix composites (AMCs) have attracted considerable attention in aerospace, automotive and defense sectors owing to their high specific strength, good corrosion resistance and design flexibility compared with conventional monolithic alloys [1–3]. Among the commercially available alloys, Al6061 is widely preferred as a matrix material because of its good castability, weldability and age-hardenability, which enable tailoring of mechanical properties through T6 heat treatment [4,5]. Nevertheless, the intrinsic strength and impact resistance of monolithic Al6061 are often insufficient for demanding applications involving severe abrasion or ballistic loading, motivating the development of particle-reinforced aluminum matrix composites and architectured laminate systems [3,6].

Boron carbide (B_4C) is one of the most attractive ceramic reinforcements for aluminum matrices due to its unique combination of very high hardness, low density, high elastic modulus and good chemical stability [7,8]. Numerous studies have shown that the incorporation of B_4C particles into aluminum alloys significantly improves hardness, strength and stiffness, provided that a reasonably uniform particle distribution is achieved [9–11]. Both micro- and nano-scale B_4C additions to 6xxx and 7xxx series alloys have been reported to increase tensile strength and hardness compared with the unreinforced matrices, especially when the fabrication route promotes microstructural refinement and minimizes porosity [9–11]. In parallel, systematic wear studies on Al–B_4C composites have demonstrated substantially reduced wear rates and improved abrasion resistance under dry sliding, confirming the efficiency of B_4C as a hard load-bearing phase in tribological contacts [12–14]. These improvements, together with the low density of B_4C, make Al/B_4C systems highly promising for lightweight structural and armour applications [7,8,12].

The ballistic behavior of aluminum-based alloys and composites has therefore become a critical research topic for personal and vehicle armour systems. Aluminum plates and aluminum–ceramic or aluminum–polymer hybrid systems are widely used as front or backing layers in multi-layered armour because of their capacity to undergo large plastic deformation, absorb kinetic energy and stabilize brittle or quasi-brittle strike faces [15,16]. Particle-reinforced aluminum matrix composites containing SiC, Al_2O_3 or B_4C generally exhibit enhanced ballistic resistance relative to their monolithic counterparts, mainly through increased hardness and localized resistance to penetration, as well as modified failure mechanisms under high-velocity impact [17–19]. Studies on functionally graded Al6061-based composites reinforced with different ceramic particles have indicated that B_4C-reinforced configurations

can offer superior energy absorption and lower penetration depths at comparable areal densities, highlighting the potential of B_4C for armour-grade MMCs [20]. Experimental and numerical investigations further emphasize that the ballistic response depends not only on reinforcement type and volume fraction, but also on target thickness, projectile characteristics and the detailed architecture of the composite system, including the presence of interlayers or backing materials [15–20].

In addition to monolithic plates, laminated aluminum and fiber–metal laminate (FML) concepts have emerged as effective strategies to improve damage tolerance and impact resistance while maintaining low weight [21–23]. Laminated metallic composites consisting of alternating layers of identical or dissimilar alloys (or metals such as aluminum, steel and titanium) offer opportunities to tailor stiffness, strength, crack resistance and failure modes through layer sequencing and thickness design [21,22]. Under impact and ballistic loading, appropriately designed laminates can enhance ballistic limits and delay catastrophic failure by activating multiple energy-dissipating mechanisms, such as interfacial delamination, constrained plastic flow and progressive cracking across layers [22,23]. These findings indicate that laminate architectures can be engineered to optimize impact and ballistic performance beyond what can be achieved with single-layer plates of the same base alloy and areal density.

Despite these advances, the literature on **monolithic versus laminated Al6061/B_4C systems** remains limited. Most Al/B_4C studies focus either on monolithic plates produced by stir casting, powder metallurgy or surface modification routes, with emphasis on static mechanical properties, wear behavior or single-layer ballistic performance [9–14,17–20]. On the other hand, many laminate and armour studies involve different aluminum alloys, metal–metal laminates or fiber–metal laminates, rather than laminated configurations specifically combining monolithic Al6061 and Al6061/B_4C composite layers [21–23]. As a result, the influence of layer architecture and reinforcement on the comparative mechanical and ballistic behavior of **monolithic Al6061, monolithic Al6061/B_4C composites and laminated Al6061/B_4C–Al6061 structures** has not been systematically clarified.

This study addresses this gap by presenting a comprehensive investigation on three different configurations: (i) monolithic Al6061, (ii) monolithic Al6061/B_4C composite, and (iii) a two-layer laminated composite consisting of an Al6061/B_4C layer bonded to an Al6061 layer. All specimens are fabricated via a powder metallurgy route followed by hot pressing, and subsequently subjected to T6 heat treatment to achieve a comparable microstructural condition in the matrix. Mechanical tests and ballistic experiments using 7.62×51 mm M80 projectiles are

carried out and comparatively evaluated to elucidate the effect of layer design on material response. This integrated approach provides a scientific basis for optimizing Al6061/B_4C-based lightweight armour structures and contributes to the development of next-generation engineering solutions for high-performance protective applications [24].

2. Experimental Procedures

2.1 Production of Composite Materials

Al6061-based composite specimens were fabricated using a powder metallurgy route involving powder mixing, cold pressing, hot pressing, and subsequent T6 heat treatment. Gas-atomized Al6061 alloy powder (<150 μm, 99.0% purity) was selected as the matrix, while boron carbide (B_4C) ceramic powder (<10 μm, 99.0% purity) served as the reinforcement phase (Fig. 1). The physical properties of the powders are summarized in Table 1.

Table 1. Physical properties of Al6061 and B_4C powders

Property	Al6061 Alloy Powder	Boron Carbide (B_4C) Powder
Particle size (μm)	< 150	< 10
Particle morphology	Spherical–irregular	Angular
Purity (%)	99.0	99.0
Melting point (°C)	582–652	2450
Density (g/cm³)	2.70	2.52

Three composite architectures were fabricated with nominal dimensions of 60 × 60 × 24 mm, as summarized in Table 2. For each material, the required powder quantities were calculated according to the target weight fractions and measured using a microbalance with 0.0001 g precision. The powders were then sealed in polyethylene containers and mixed for 30 minutes in a Turbola T2F three-dimensional mixer to ensure homogeneous dispersion of B_4C particles.

The blended powders were then loaded into a custom-designed HWS 2344 hot-work tool steel die (60 × 60 mm cross-section. A two-step compaction process was applied. First, cold pressing was performed at 15 MPa to obtain a green compact (preform). Subsequently, the die was heated to 580 °C and held for 45 minutes, after which a hot-pressing pressure of 300 MPa was applied. After pressing, the die was cooled to room temperature, producing fully consolidated blocks with the final dimensions.

Table 2. Description of the fabricated composite specimens

Specimen Code	Layer Structure	Reinforcement fraction (wt.%)	Description
S1	Monolithic (single layer)	50 wt.% B_4C	Fully reinforced Al6061/B_4C composite
S2	Bilayer (two-layer FGM)	Top: 50 wt.% B_4C Bottom: 0 wt.% B_4C	Laminated composite with reinforced upper layer and pure Al6061 backing
S3	Bilayer (two-layer FGM)	Top: 40 wt.% B_4C Bottom: 0 wt.% B_4C	Laminated composite with lower reinforcement intensity in the upper layer

To enhance the mechanical performance of the composites, all specimens were subjected to a standard T6 heat treatment. Solution treatment was carried out at 530 °C for 1 hour (heating rate: 10 °C/min), followed by immediate water quenching. Artificial aging was then performed at 175 °C for 8 hours, resulting in a fully precipitation-hardened microstructure. The final material architectures used for ballistic testing are illustrated in Fig. 2.

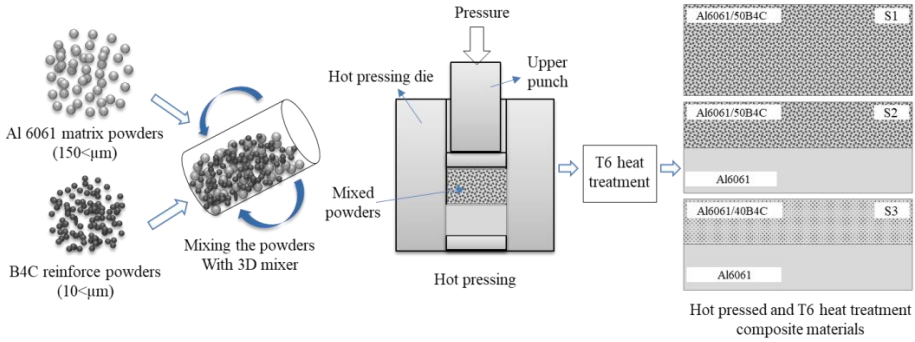

Fig. 1. Schematic representation of the composite configurations used for ballistic testing: S1 (Al6061–50%B_4C), S2 (Al6061–50%B_4C/Al6061 laminat

2.2 Microstructural, mechanical and ballistic characterization

The composite plates were sectioned using a water-jet cutting system to prevent thermal distortion and to preserve the intrinsic microstructural features. Density measurements were performed using a Sartorius analytical density kit with a precision of 0.1 mg, following Archimedes' principle (Eq. 1):

$$Dg=\frac{Wa}{Wa-Wb}\times D_{H_2O} \quad (1)$$

where Dg is the measured density (g/cm³), Wa is the mass in air (g), Wb is the suspended mass in water (g), and D_{H2O} is the density of water (g/cm³).

The theoretical densities of the composites were calculated using the rule of mixtures based on the volume fractions of Al6061 and B_4C (Eq. 2):

$$\rho_{MMC} = \rho_{Al} * V_{Al} + \rho_{B4C} * V_{B4C} \quad (2)$$

Where ρ_{MMC} is the of the composites, V_{Al} and V_{B4C} are the volume fraction of aluminum and B_4C in matrix.

For microstructural examination, samples were ground sequentially using 600, 800, 1000, 1200, and 2500 grit SiC abrasive papers under running water. This was followed by polishing with 6 μm, 3 μm, and 1 μm diamond suspensions to obtain a mirror-like finish. Keller's reagent was used to etch the polished surfaces prior to optical microscopy analyses. Optical microstructures were acquired using a Leica DM4000M microscope, while detailed observations of the reinforcement–matrix interface, fracture modes, and post-ballistic deformation regions were carried out using a Zeiss EVO 50 SEM.

Hardness measurements were conducted using the Brinell method with a 2.5 mm diameter indenter under a load of 31.25 kgf. These measurements were repeated at multiple locations to ensure statistical consistency. The transverse rupture strength (TRS) tests were performed using an Instron 3369 universal testing machine with a load capacity of 50 kN. All TRS measurements were conducted under three-point bending conditions in accordance with MPFI-10 and MPFI-41 standards, employing a constant crosshead displacement rate of 1 mm/min. Rectangular specimens were positioned centrally on the support anvils to ensure uniform load transfer, and the applied load–displacement data were recorded continuously until catastrophic failure occurred. The maximum load at fracture was subsequently used to calculate TRS, providing a quantitative assessment of the flexural strength and brittle–ductile fracture response of the monolithic and laminated composites.

Ballistic performance was evaluated according to the National Institute of Justice (NIJ) Standard 0101.06 for Type III threats. Composite plates (60 × 60 × 24 mm) were rigidly mounted on a backing fixture and positioned 10 m from the firing point. A G3 rifle was used to fire 7.62 × 51 mm NATO M80 projectiles at the targets. Impact velocities during both calibration and experimental firings ranged between 822 and 838 m/s.

3. Experimental results

3.1 Morphology and Chemical Characterization of Starting Powders

The morphology of the starting powders plays a decisive role in achieving microstructural uniformity, efficient compaction, and enhanced mechanical performance in powder-metallurgy-processed composites. The SEM micrograph of the Al6061 alloy powder (Fig. 2a) shows predominantly spherical particles accompanied by a small fraction of irregularly shaped ones, which is characteristic of gas-atomized aluminum powders. The near-spherical morphology improves packing efficiency during compaction, promotes homogeneous stress distribution, and facilitates metallurgical bonding during hot pressing. The presence of minor surface asperities and satellite particles attached to larger droplets further contributes to mechanical interlocking, thereby enhancing the green compact strength.

In contrast, the B_4C reinforcement powder exhibits a distinctly angular, faceted, and sharp-edged morphology (Fig. 2b), typical of brittle ceramic particulates produced through crushing or mechanical milling. This angularity provides strong mechanical anchorage within the aluminum matrix, improving load-transfer capability and restricting dislocation motion. However, the irregular geometry may also reduce flow uniformity during mixing, making adequate blending essential to avoid local particle agglomeration and clustering.

The EDS spectrum obtained from the Al6061 powder (Fig. 2c) confirms the expected alloying constituents such as Mg, Si, Fe, and Ti, consistent with the nominal composition of AA6061. The chemical purity and absence of unintended secondary phases validate the suitability of both powders for producing high-quality Al-based metal matrix composites with stable interfacial chemistry.

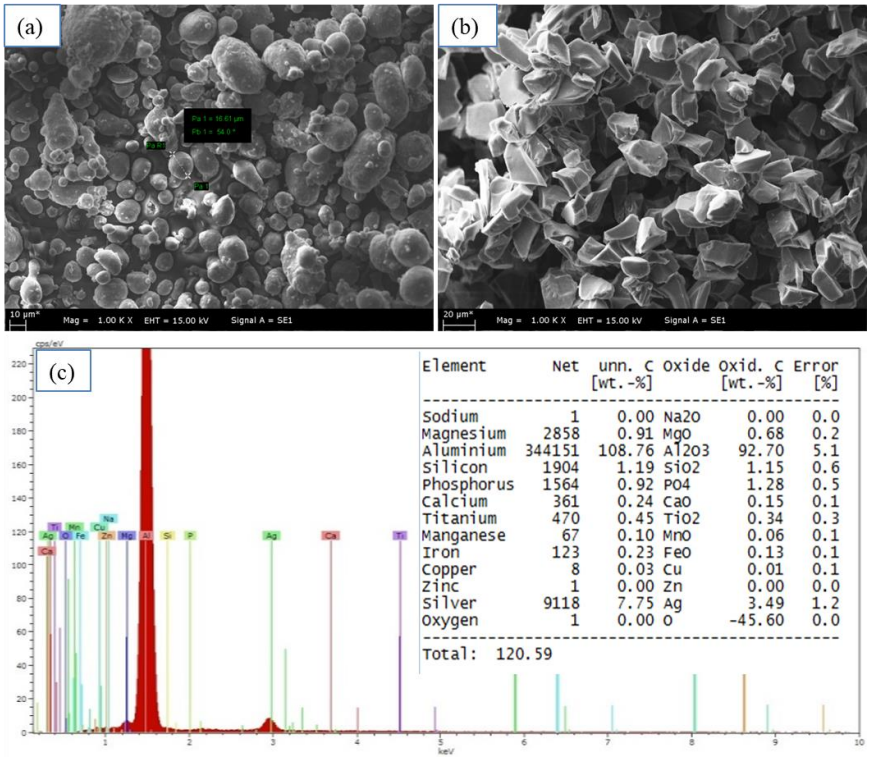

Fig. 2. SEM images and EDS results of the starting powders: (a) Al6061 powder showing predominantly spherical and irregular particles; (b) angular B_4C particles; (c) EDS spectrum of Al6061 powder.

3.2 Mechanical Properties: Density, Hardness and TRS Behavior

The theoretical and experimental density values of the composites exhibit a consistent trend predicted by the rule of mixtures. As the B_4C content increases, the overall density decreases due to the intrinsically lower density of B_4C (2.52 g/cm³) relative to Al6061 (2.70 g/cm³). Similar findings are reported in the literature, where increasing B_4C content in Al-based powder metallurgy systems is known to reduce green and sintered densities due to particle clustering and the formation of micro-porosities [25]. Minor discrepancies between theoretical and experimental densities in the present work are attributed to the limited compressibility of hard ceramic particles, which restrict matrix deformation during compaction.

Despite this, all specimens in the present study achieved high relative density levels (>99%), indicating effective consolidation during hot pressing. This observation aligns with the results of Xu et al. [26], who demonstrated through multi-particle finite element simulations and experimental validation

that higher compaction temperature and pressure significantly enhance particle rearrangement, plastic deformation, and densification during the hot-pressing of 6061-based composites. Their findings also reveal that rigid ceramic reinforcements act as mechanical barriers, limiting localized plastic flow and reducing the final densification—an effect evident in the laminated S2 and S3 specimens.

Furthermore, the reduced local plastic flow around ceramic particles is consistent with the results of Bodukuri et al. [27], who reported that increasing reinforcement content (SiC and B_4C hybrid additions) decreases the compressibility of aluminum powders, increases porosity tendency, and requires higher compaction pressures to achieve optimum densification. These observations collectively support the slight deviation from theoretical density observed particularly in the laminated samples of the present study.

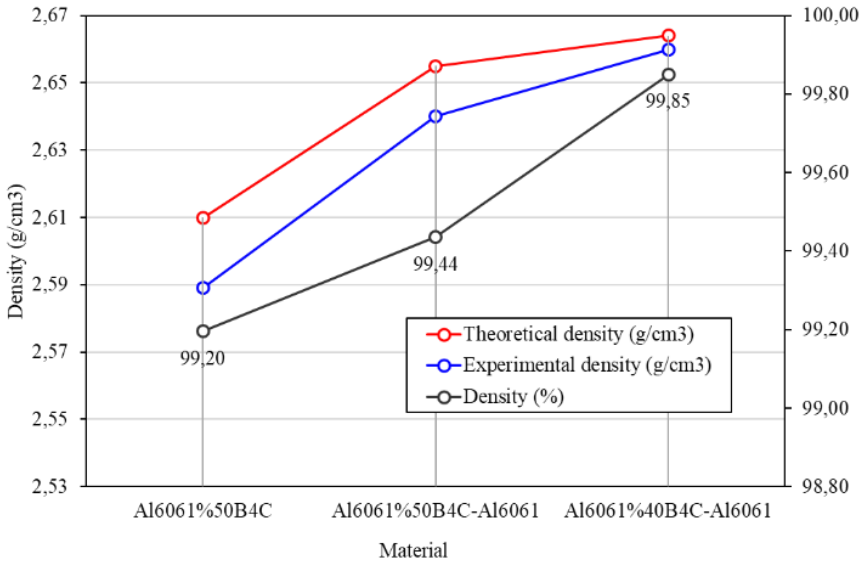

Fig. 3. Density results of monolithic and laminated Al6061/B_4C composites.

The hardness profiles of the monolithic and laminated Al6061/B_4C composites are shown in Fig. 4. As expected, the monolithic Al6061–50%B_4C specimen exhibits the highest hardness, primarily due to the intrinsically high hardness of B_4C and its strong capability to impede plastic deformation within the aluminum matrix. The laminated specimens (Al6061–50%B_4C/Al6061 and Al6061–40%B_4C/Al6061) reveal a gradual increase in hardness toward the

reinforced layer, indicating a continuous and well-bonded mechanical transition across the thickness.

This trend is consistent with previous studies on Al–B_4C composites, where increasing ceramic content and/or particle size enhances hardness through dispersion strengthening, improved load sharing, and obstruction of dislocation motion [28]. Göçer and Karamış [28] reported that the addition of 10 vol.% B_4C to an Al6061 matrix, followed by extrusion and T6 heat treatment, led to a marked increase in Vickers hardness, and that larger B_4C particles further promoted hardness due to their higher load-bearing capacity.

Chen et al. [29] similarly showed that in powder-metallurgy B_4C/7A04Al composites, solution treatment and subsequent aging enable the reinforcements and reaction products (e.g., $Mg(Al)B_2$) to effectively restrict matrix deformation, resulting in high strength and hardness over a relatively wide solution temperature window. Their findings confirm that well-bonded ceramic particles in heat-treatable aluminum matrices play a dominant role in hardening by impeding dislocation motion and stabilizing the microstructure at elevated temperatures.

In addition, functionally graded aluminum-based composites have been reported to develop characteristic hardness gradients as a function of reinforcement distribution. Melgarejo et al. [30] observed that centrifugally cast Al–B–Mg composites exhibit increasing superficial and microhardness from the inner to the outer regions, in direct correlation with the increasing volume fraction of boride particles. This behavior supports the smooth hardness transition observed in the laminated S2 and S3 specimens of the present study and indicates the absence of mechanical discontinuities, reflecting successful interlayer bonding.

The measured hardness values align with strengthening mechanisms well established for ceramic–metal systems, where reinforcement particles impose substantial resistance to dislocation motion. The hardness gradients observed in the laminated structures demonstrate that combining a stiff, B_4C-rich strike layer with a more ductile Al6061 backing layer enables a tailored mechanical response advantageous for structural and ballistic applications.

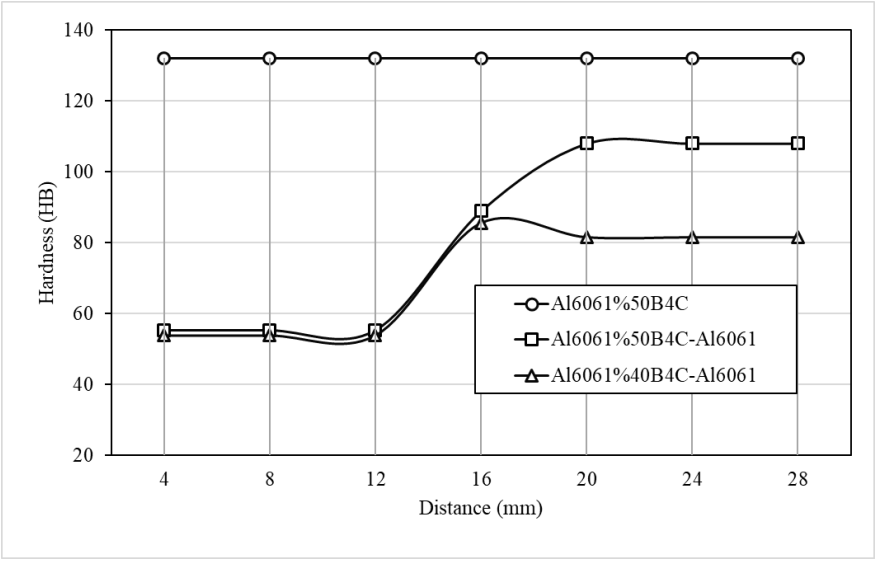

Fig. 4. Hardness profiles of monolithic and laminated Al6061/B_4C composites.

Figure 5 presents the transverse rupture strength (TRS) behavior of the monolithic Al6061–50%B_4C composite and the laminated Al6061–50%B_4C/Al6061 and Al6061–40%B_4C/Al6061 structures. The monolithic S1 composite exhibits the highest initial flexural stiffness but fails at relatively low strain, reflecting its brittle, ceramic-dominated fracture response. The high B_4C fraction increases elastic modulus and load-transfer efficiency; however, it also promotes early crack initiation through particle–matrix interfacial mismatch and particle fracture, which restricts bending ductility. Similar brittle-controlled TRS behavior has been reported in Al–B_4C systems produced by powder metallurgy, where increasing reinforcement content leads to particle clustering, interfacial decohesion, and premature catastrophic failure under bending loads [31].

The laminated S2 specimen (Al6061–50%B_4C/Al6061) displays a noticeably higher TRS due to the combined deformation mechanisms of the stiff ceramic-rich surface and the ductile Al6061 backing layer. The metallic interlayer delays unstable crack propagation by promoting plastic bridging and crack deflection across the interface. Such laminated architectures are known to enhance flexural and rupture strength by distributing tensile stresses away from brittle, particle-rich regions. This trend is consistent with observations in hybrid Al–ceramic laminated composites, where layered configurations reduce stress localization and improve bending performance by activating multiple crack-arrest mechanisms [31].

The S3 laminate (Al6061–40%B_4C/Al6061) provides the most balanced mechanical response, combining moderate stiffness with the highest rupture strain.

Lowering the B_4C content reduces local stress concentrations and minimizes particle-induced microcracking, thereby enhancing energy absorption prior to failure. Similar behavior has been reported in powder-metallurgy-processed Al–ceramic composites, where optimal reinforcement levels improve TRS by maintaining matrix continuity, reducing particle clustering, and enhancing interparticle bonding during consolidation [29], [31]. These studies further emphasize that TRS increases when the reinforcement fraction remains below the agglomeration threshold, allowing better load transfer and matrix flow—directly reflected in the superior TRS performance of the S3 laminate.

Overall, the TRS comparisons indicate that laminated architectures and controlled ceramic contents enhance fracture tolerance by activating ductile bending, crack deflection, and plastic bridging mechanisms. The monolithic S1 specimen fails predominantly through brittle fracture, whereas the S2 and S3 laminates exhibit mixed deformation modes, with the S3 configuration providing the most advantageous combination of stiffness, ductility, and crack resistance.

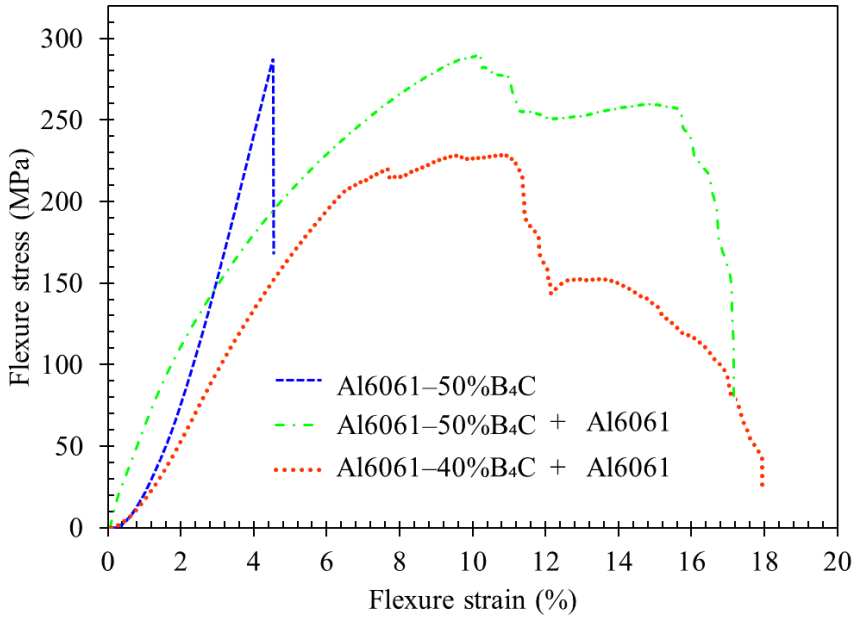

Fig. 5. Flexural stress–strain curves of the Al6061–50%B_4C monolithic composite and the laminated Al6061–50%B_4C/Al6061 and Al6061–40%B_4C/Al6061 composites.

Figure 6 illustrates the fracture morphologies of the S1, S2, and S3 composites after TRS loading, highlighting the influence of reinforcement content and laminate design on failure behavior. In the monolithic S1 composite (Al6061–50%B_4C), the fracture surface is dominated by brittle features such as cleavage-like facets, fragmented B_4C particles, and extensive particle–matrix decohesion. The high ceramic fraction amplifies local stress concentrations and restricts plastic accommodation within the aluminum matrix, causing early crack initiation and rapid crack propagation. This brittle, particle-controlled fracture mode is typical of metal–ceramic systems with high reinforcement levels.

The laminated S2 specimen (Al6061–50%B_4C/Al6061) exhibits a mixed-mode failure response. The Al6061 backing layer provides additional ductility, promoting the formation of dimples and enabling plastic deformation in the transition zone. Although B_4C fracture and localized clustering are still visible, the metallic layer delays crack propagation through plastic bridging and crack deflection. This interaction between a stiff ceramic-rich surface and a ductile aluminum layer enhances the TRS by redistributing tensile stresses more uniformly.

The S3 laminate (Al6061–40%B_4C/Al6061) presents the most ductile fracture characteristics. Reduced B_4C content results in fewer stress concentration sites and a more continuous matrix network, allowing extensive dimple formation and increased energy absorption. Particle pull-out and mild interfacial decohesion occur but are less frequent compared to S1 and S2. The improved plasticity indicates that a moderate reinforcement fraction provides a more favorable balance between stiffness and toughness during bending.

The fracture analyses thus demonstrate a clear transition from brittle-dominated behavior in the monolithic composite to more ductile, energy-dissipating mechanisms in the laminated structures. The combination of crack deflection at layer interfaces, enhanced matrix plasticity, and reduced particle-induced stress concentrations contributes to the superior TRS performance of the laminated S2 and S3 specimens.

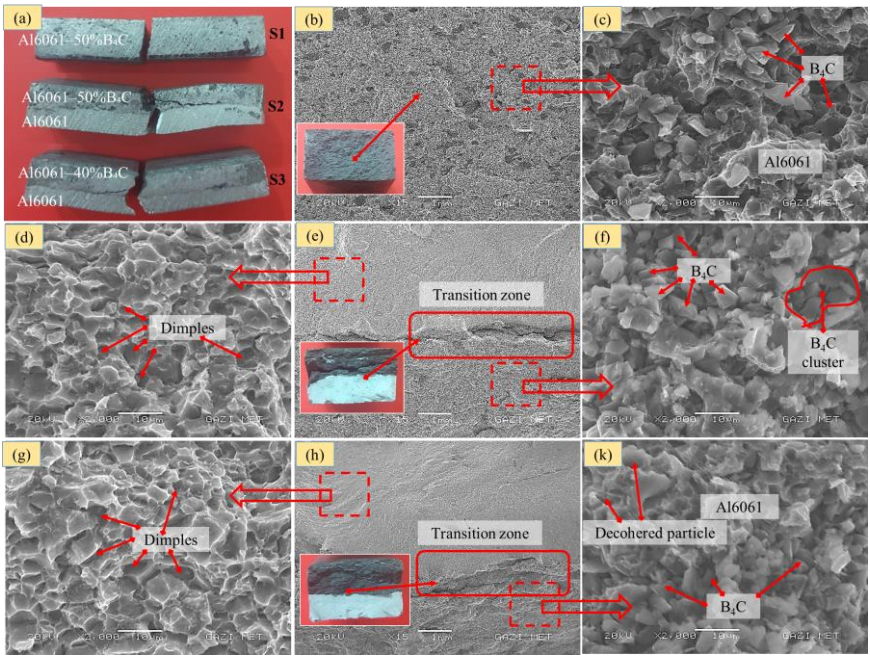

Fig. 6. Fracture surfaces of S1, S2 and S3 composites after TRS testing: (a–c) S1 (Al6061–50%B_4C), (d–f) S2 (Al6061–50%B_4C/Al6061), and (g–k) S3 (Al6061–40%B_4C/Al6061) showing dimples, B_4C particles, clusters, and particle–matrix decohesion.

The microstructural evaluation of the Al6061–50%B_4C composite (Fig. 7) provides detailed insight into particle dispersion, interface quality, and chemical stability following powder-metallurgy-based consolidation. The SEM micrograph (Fig. 7a) shows angular B_4C particles uniformly embedded within the Al6061 matrix without evidence of severe agglomeration or clustering. This uniform dispersion is essential for establishing efficient load-transfer pathways and for minimizing local stress concentrations, both of which directly influence hardness, strength, and impact resistance.

The EDS spectrum obtained from Region 1 (Fig. 7b), corresponding to a dark-contrast particle, exhibits strong boron (B) and carbon (C) peaks, confirming the presence and chemical stability of B_4C after hot pressing. Importantly, no additional peaks associated with reaction products such as Al_3BC or AlB_2 were detected. The absence of these phases indicates that the processing temperature and dwell time were sufficiently controlled to prevent detrimental interfacial reactions that could reduce bonding strength or compromise ballistic performance.

In contrast, the EDS analysis of Region 2 (Fig. 7c) reflects a matrix composition dominated by aluminum with Mg, Si, and Fe present at levels typical of Al6061 alloys. The absence of B and C in this region confirms a clean phase separation between the reinforcement and matrix. Moreover, the SEM image shows no micro-void formation or decohesion near the particle–matrix boundary, suggesting strong metallurgical bonding. Robust interfacial integrity is critical because B_4C particles contribute to strengthening primarily through mechanisms such as Orowan looping, load sharing, and dislocation pile-up; inadequate bonding would diminish these effects.

These combined SEM–EDS observations validate that the powder-metallurgy/hot-pressing route produced a structurally coherent composite with a chemically stable reinforcement phase, well-preserved interfaces, and uniform particle dispersion. Such a microstructural configuration forms a reliable foundation for improved hardness, stiffness, and ballistic energy absorption, particularly under high-load or high-strain-rate conditions where particle–matrix interaction dominates the deformation response.

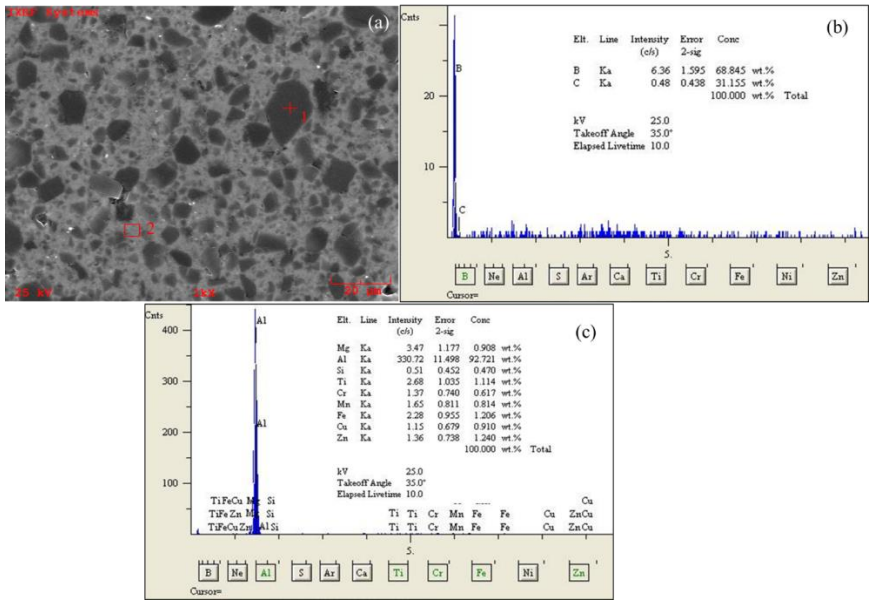

Fig. 7. SEM–EDS results of the Al6061–50%B_4C composite: (a) SEM image; (b) EDS spectrum of a B_4C-rich region 1; (c) EDS spectrum of the Al-rich matrix 2.

The SEM–EDS analyses of the Al6061–50%B_4C composite (Fig. 8) reveal a microstructure in which angular B_4C particles are uniformly embedded within the aluminum matrix. The B_4C reinforcements appear as bright, high-contrast regions, whereas the Al-rich matrix maintains a relatively homogeneous

background morphology. Small micro-voids detected around some particles are characteristic of powder-metallurgy-processed MMCs and are typically attributed to particle–matrix interfacial mismatch during compaction and consolidation.

A comparable dispersion behavior was reported by Şenel et al. [32], who observed that B_4C-reinforced aluminum composites produced by powder metallurgy exhibit a homogeneous spatial distribution of ceramic particles accompanied by localized micropores formed during compaction and sintering. Consistent with their findings, the EDS spectrum of Region 1 in Fig. 8 confirms strong boron and carbon peaks, verifying the chemical identity of the B_4C reinforcement. In contrast, Region 2 displays a dominant Al peak with Mg, Si, and trace alloying elements in proportions characteristic of Al6061, confirming the clear compositional separation between the ceramic phase and the metallic matrix.

Other studies have shown that micro-scale B_4C particles contribute to structural stability by anchoring grain boundaries and acting as rigid load-bearing sites during mechanical loading [33]. Their high hardness and elastic modulus mismatch with the aluminum matrix also restrict dislocation motion, leading to pronounced dispersion strengthening—a mechanism frequently reported in Al6061–B_4C and Al6061–SiC–B_4C composites [34].

Taken together, the SEM–EDS results validate that B_4C particles were successfully incorporated into the Al6061 matrix with chemically stable interfaces, uniform spatial distribution, and minimal agglomeration. Such a microstructural configuration is advantageous for enhancing hardness, stiffness, and impact resistance in B_4C-reinforced aluminum composite systems.

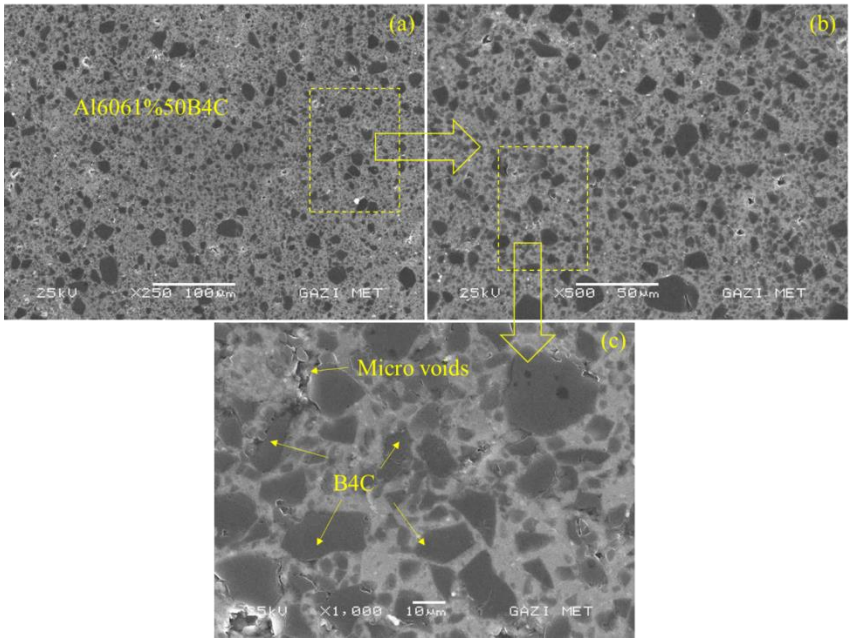

Fig. 8. SEM images of the Al6061–50%B_4C composite at low, medium, and high magnifications.

The SEM micrographs of the S2 laminate (Fig. 9) clearly demonstrate the layered configuration formed between the Al6061 substrate and the Al6061–50%B_4C composite layer. As seen in Fig. 9a, the interface exhibits a well-defined transition region without signs of interfacial cracking or delamination, indicating successful metallurgical bonding during hot pressing. This continuous interface confirms that the thermal–mechanical processing parameters were sufficient to achieve strong interlayer cohesion. The reinforced layer shown in Fig. 9b contains a dense and uniform distribution of angular B_4C particles embedded within the aluminum matrix. The morphology and dispersion of the ceramic phase suggest efficient powder mixing and consolidation, with no pronounced particle agglomeration. The high-magnification micrograph in Fig. 9c reveals tightly anchored B_4C particles accompanied by small micro-voids. Such voids commonly arise in powder metallurgy composites due to localized plastic flow mismatch or thermal contraction differences between the brittle ceramic particles and the ductile Al matrix. Their presence at limited levels does not compromise structural integrity and is consistent with typical microstructural features of Al-based ceramic-reinforced laminates. Collectively, the SEM observations confirm that the S2 laminated composite possesses strong interfacial bonding, homogeneous

particle dispersion in the reinforced layer, and stable particle–matrix interactions—all of which are essential for achieving improved mechanical and ballistic performance.

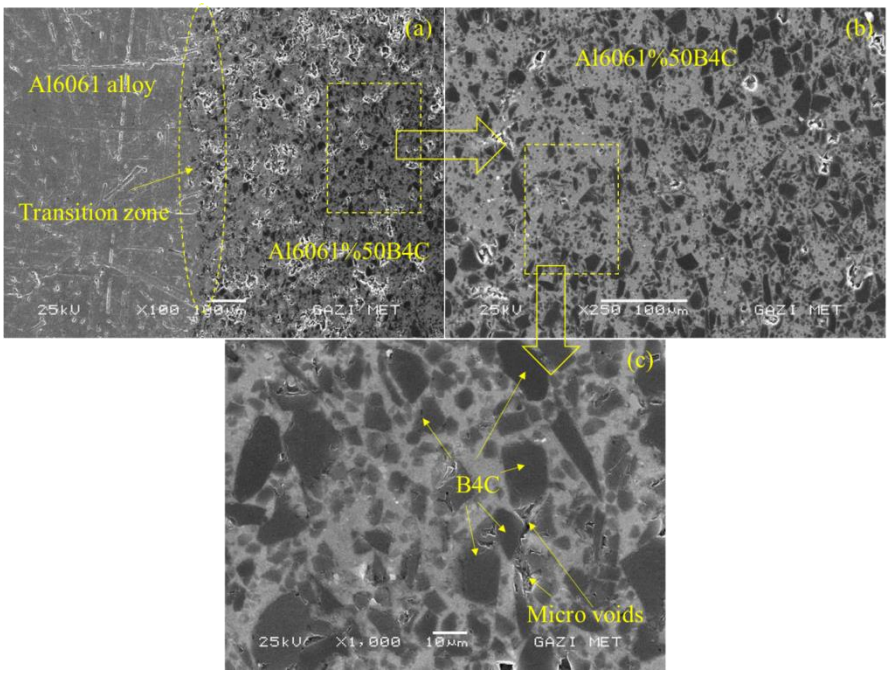

Fig. 9. SEM images of the S2 laminate showing (a) the Al6061/Al6061–50%B_4C interface, (b) the reinforced layer, and (c) B_4C particles with micro-voids.

Figure 8 illustrates the microstructural features of the S3 laminate, composed of a pure Al6061 substrate and a 40%B_4C-reinforced upper layer. As seen in Fig. 8a, a continuous and well-defined transition zone is present at the Al6061/Al6061–40%B_4C interface, confirming successful metallurgical bonding without signs of interfacial cracking or delamination. This indicates that the applied hot-pressing parameters were sufficient to achieve strong interlayer cohesion. The reinforced region (Fig. 8b) exhibits a dense and uniform distribution of angular B_4C particles, demonstrating effective incorporation of the ceramic phase during powder mixing and consolidation. The particle dispersion suggests minimal agglomeration, which is critical for ensuring homogeneous load transfer and reducing stress concentration zones. The high-magnification micrograph in Fig. 8c reveals B_4C particles firmly embedded in the Al6061 matrix, accompanied by a limited number of micro-voids. These small voids are typically associated with local plastic flow mismatch or particle–matrix interfacial incompatibility during compaction and

thermal shrinkage. Their minimal occurrence indicates good overall consolidation quality.

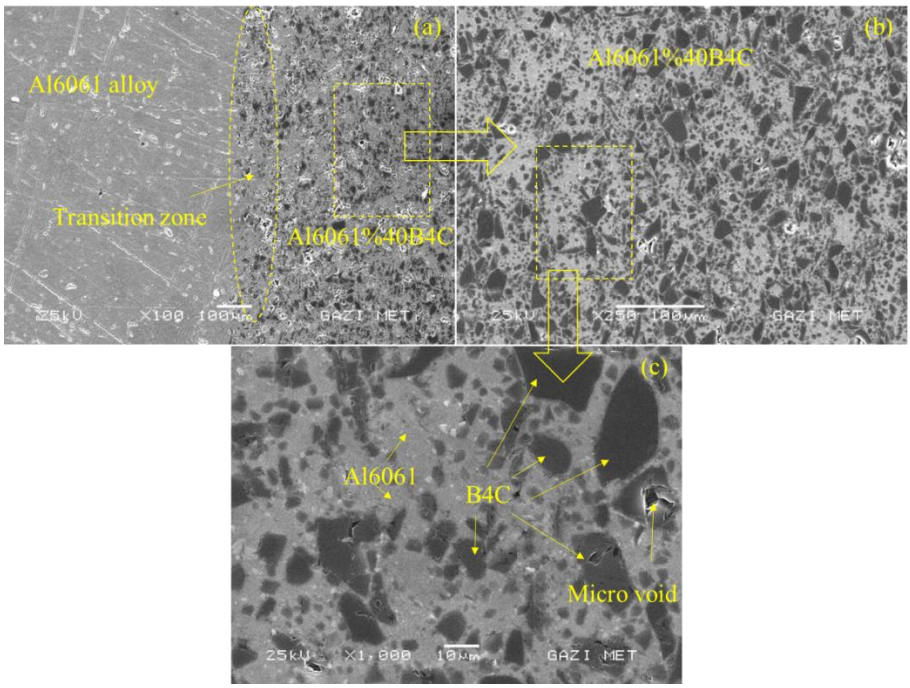

Fig. 10. SEM images of the S3 laminate showing (a) the Al6061/Al6061–40%B_4C interface, (b) the 40%B_4C-reinforced layer, and (c) embedded B_4C particles with micro-voids

Figure 11 illustrates the ballistic response of the S1 monolithic Al6061–50%B_4C composite subjected to 7.62×51 mm M80 projectiles. The front surface displays pronounced radial cracking, conical fracture patterns, and localized fragmentation—typical of brittle ceramic–metal composites under high strain-rate loading. This type of damage morphology is consistent with previous reports on B_4C-based systems, where high ceramic content promotes shock-induced brittle failure and rapid crack propagation [35].

On the rear surface, limited spalling accompanied by a macro-crack indicates that although a substantial portion of the projectile's kinetic energy was absorbed in the strike-face region, the remaining energy was dissipated through plastic deformation within the Al6061 matrix. The high B_4C content contributes to severe erosive wear and significant blunting of the projectile tip, reducing penetration capability—consistent with projectile erosion/passivation

mechanisms widely reported in ceramic-reinforced aluminum armor structures [36].

Cross-sectional SEM examinations reveal a combination of B_4C particle fracture, matrix cracking, and particle–matrix interfacial decohesion. These mechanisms play a central role in energy dissipation during impact. Fragmentation of B_4C reinforcements and crack deflection around both fractured and intact particles generate complex crack paths, enhancing the fracture work and promoting multidirectional stress-wave dispersion. This behavior aligns closely with established crack-deflection and interface-failure–assisted energy absorption mechanisms in Al–ceramic composite armors [37].

Taken together, the ballistic resistance of the S1 composite is governed by a cooperative set of protection mechanisms. First, the ceramic-rich strike face causes pronounced erosive wear and blunting of the projectile, effectively reducing its penetration efficiency. Second, brittle fragmentation in the strike face absorbs a substantial portion of the impact energy. Third, crack deflection and branching around angular B_4C particles create tortuous propagation paths that enhance energy dissipation. Finally, the remaining kinetic energy is accommodated by localized plastic deformation within the Al6061 matrix at the rear face. These synergistic mechanisms enable the S1 composite to fully arrest the projectile, consistent with performance trends reported for high-hardness B_4C-based aluminum armor systems.

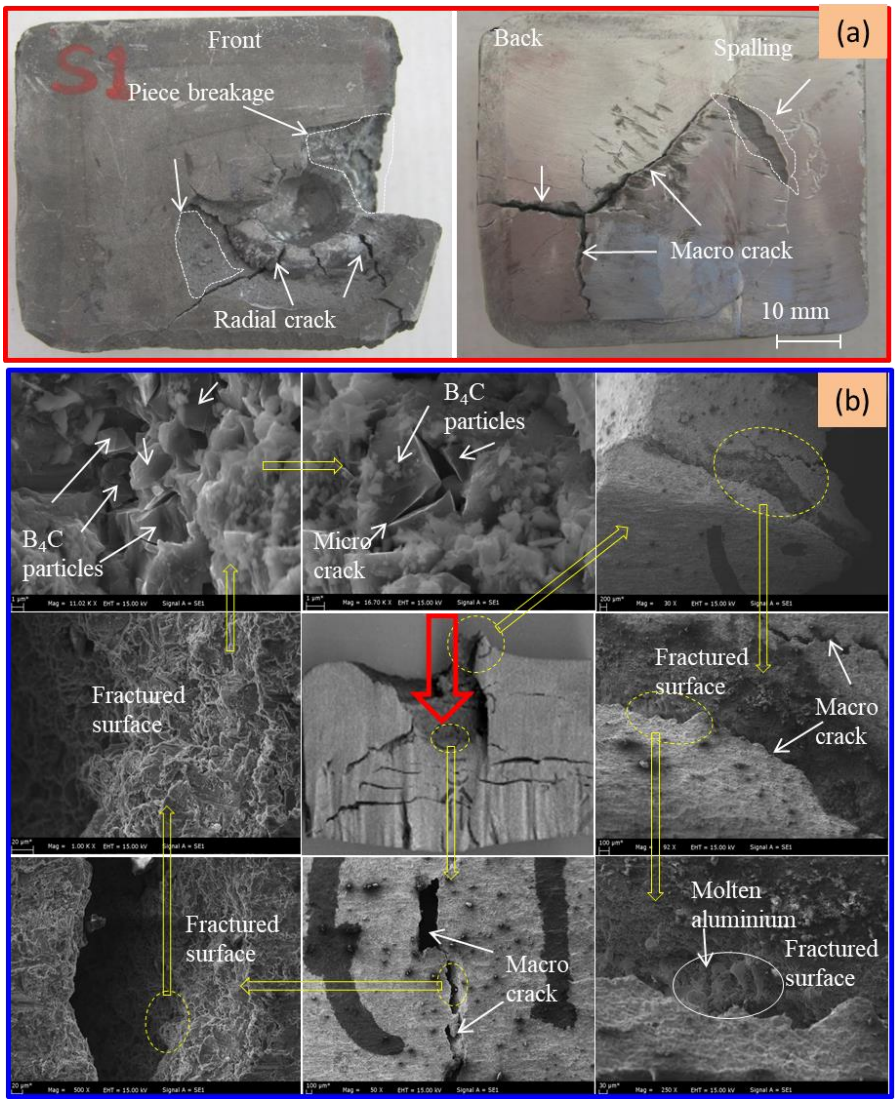

Fig. 11. Ballistic damage of the S1 monolithic Al6061–50%B_4C composite: (a) Macro views of front and back surfaces after impact; (b) Cross-sectional SEM images showing cracks and particle–matrix separation.

Figure 12 presents the ballistic response of the S2 laminated Al6061–50%B_4C/Al6061 composite, highlighting the combined effects of a brittle ceramic-rich strike face and a ductile metallic backing layer. The front surface (Fig. 12a) exhibits a localized brittle break dominated by fragmentation of the B_4C-reinforced layer, indicating that the ceramic-rich strike face absorbed a substantial portion of the impact energy through particle cracking, conical

fracture formation, and rapid radial crack propagation. This brittle response is characteristic of high-volume ceramic reinforcement systems, where stress concentrations at particle–matrix interfaces promote unstable crack growth under high strain-rate loading.

In contrast, the rear surface of S2 reveals a predominantly ductile tearing morphology. The elongated shear features and plastically deformed regions demonstrate that the Al6061 backing layer effectively attenuated residual stress waves transmitted across the laminate thickness. The presence of ductile tearing rather than catastrophic spallation indicates that the laminate architecture successfully mitigated back-face trauma by redistributing tensile stresses away from the brittle strike face.

The cross-sectional SEM observations (Fig. 12b) further elucidate the complex interplay of failure mechanisms. Near the front layer, extensive B_4C particle fracture and matrix microcracking are evident, consistent with ceramic-driven shock fragmentation. The interface between the reinforced layer and the metallic substrate shows signs of crack deflection and localized decohesion, suggesting a transition from brittle to mixed-mode fracture. These interfacial features act as barriers to crack penetration, forcing propagation along more energetically demanding paths.

Within the Al6061 backing layer, ductile dimples, molten aluminum traces, and sheared ligaments reveal significant localized heating and plastic flow, implying that adiabatic shear deformation contributed to energy dissipation. The presence of worn projectile debris and smearing at the impact cavity confirms strong projectile–target interaction, consistent with erosion/blunting mechanisms observed in laminated metal–ceramic armor systems.

Compared with the monolithic S1 composite, the S2 laminate exhibits a more controlled damage morphology, characterized by limited back-face failure and enhanced energy absorption through crack bridging, interface deflection, and ductile layer deformation. These combined mechanisms validate the effectiveness of the laminated design in improving ballistic resistance while preventing the catastrophic brittle failure commonly observed in fully ceramic-rich configurations.

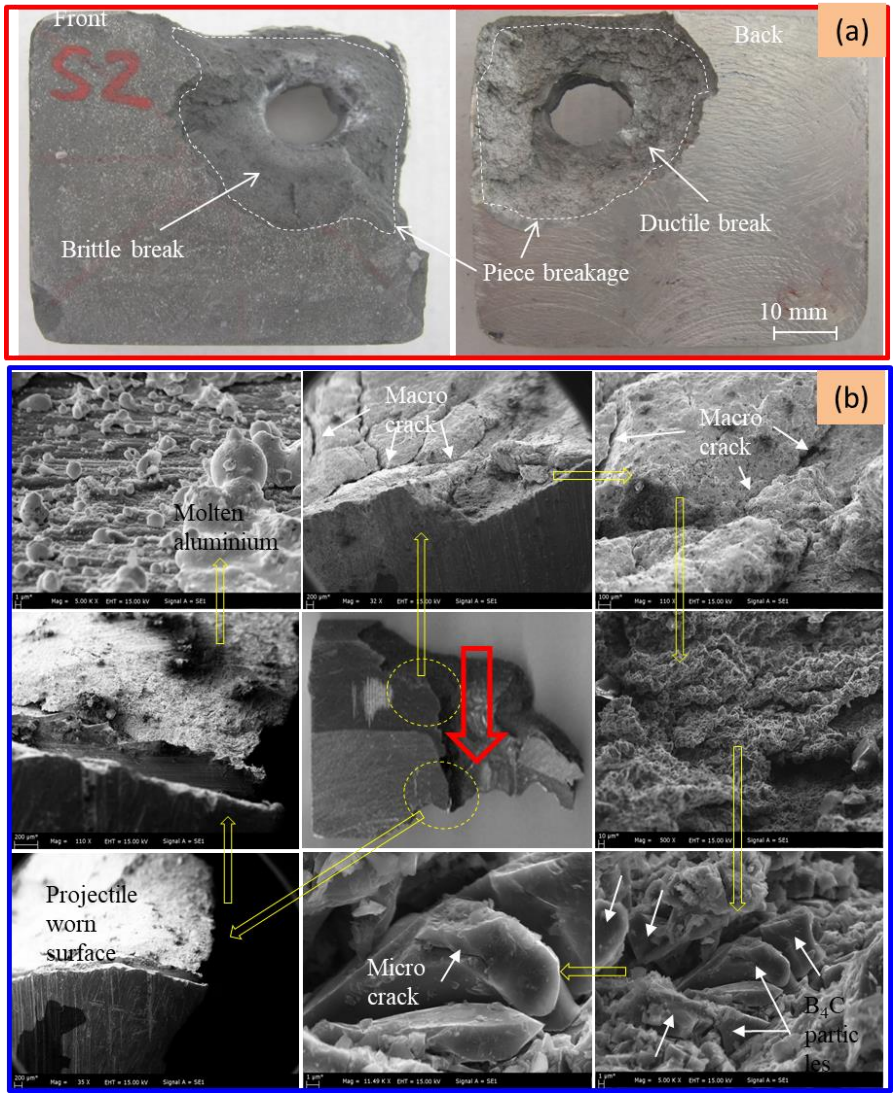

Fig. 12. Ballistic damage of the S2 laminated Al6061–50%B_4C/Al6061 composite: (a) Macro views of the front and back surfaces after impact; (b) Cross-sectional SEM images showing brittle and ductile fracture zones, particle fracture, and interfacial debonding.

Figure 13 presents the ballistic damage characteristics of the S3 laminated Al6061–40%B_4C/Al6061 composite following impact. The front surface displays limited radial cracking and a relatively confined damage zone compared with the S1 and S2 specimens. This indicates that reducing the B_4C content to 40 wt.% improves the balance between ceramic-induced hardness

and structural toughness, allowing the strike-face layer to resist catastrophic brittle fragmentation.

The back surface exhibits ductile tearing and localized piece breakage around the exit region. The absence of severe spallation shows that the Al6061 backing layer effectively absorbed the residual kinetic energy and prevented full perforation. This controlled rear-face deformation reflects the improved energy-dissipation capability provided by the lower ceramic fraction.

Cross-sectional SEM observations reveal a mixed-mode fracture morphology consisting of macro-cracks, projectile–material interaction marks, micro-cracks within the Al matrix, and partial interfacial decohesion around B_4C particles. Evidence of projectile wear and localized particle fracture demonstrates the contribution of both ceramic erosion and metal plasticity to the overall protection mechanism. The coexistence of brittle (particle cracking, cleavage) and ductile (shear flow, micro-void coalescence) features confirms that S3 undergoes a hybrid energy absorption process.

These findings indicate that the S3 laminate provides a more balanced ballistic response than the monolithic S1 composite and exhibits more controlled damage propagation than the more brittle S2 configuration. The improved behavior is primarily attributed to reduced stress concentrations, enhanced crack deflection, and better plastic accommodation within the matrix.

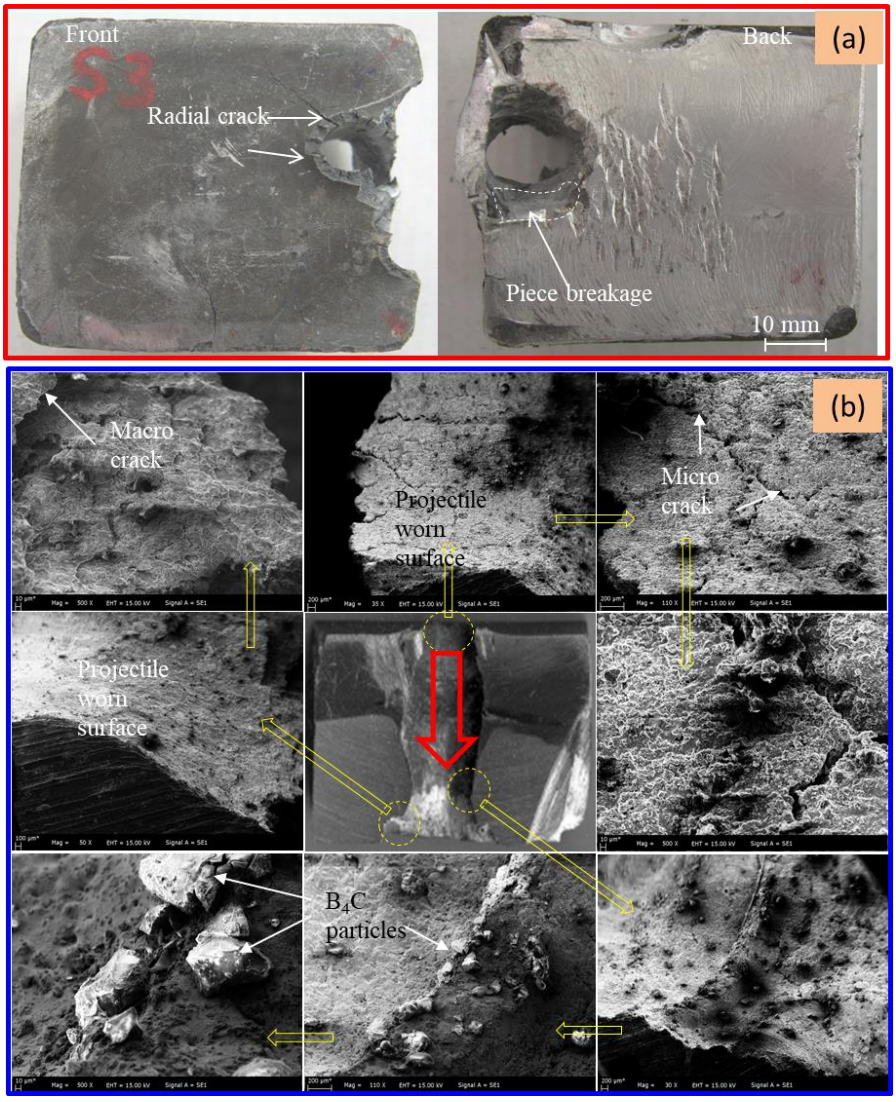

Fig. 13. Ballistic damage of the S3 laminated Al6061–40%B_4C/Al6061 composite: (a) Macro views of the front and back surfaces after impact; (b) Cross-sectional SEM images showing crack propagation, particle fracture, and interface-related failure within the graded laminate.

The ballistic responses of the three composites exhibited clear distinctions governed by reinforcement content and laminate architecture. The monolithic S1 specimen showed the most brittle behavior, characterized by extensive radial cracking and pronounced back-face spalling, a direct consequence of its fully reinforced 50 wt.% B_4C structure and the absence of a ductile energy-absorbing layer. In the S2 laminate, although the 50 wt.% B_4C strike face still failed

through brittle fragmentation, the presence of the Al6061 backing layer effectively mitigated rear-surface damage, promoting ductile tearing instead of catastrophic spallation. The S3 laminate, incorporating 40 wt.% B_4C in the strike-face layer, demonstrated the most balanced ballistic performance, with a more confined damage zone on the front surface and minimal rear-face failure. This controlled failure pattern indicates enhanced crack arrest capability and more efficient energy absorption compared with both S1 and S2.

5. Conclusions

- High-density monolithic and laminated Al6061/B_4C composites were successfully produced via a powder-metallurgy route involving cold pressing, semi-solid hot pressing and subsequent T6 heat treatment. Microstructural examinations confirmed a generally uniform dispersion of B_4C particles and sound metallurgical bonding at the layer interfaces, particularly in the laminated architectures.
- Experimental density values of all specimens exceeded 99% of the theoretical values, indicating effective consolidation despite the presence of stiff ceramic particles. Increasing B_4C content slightly reduced densification efficiency, in agreement with the rule of mixtures and the limited compressibility of the ceramic phase.
- The incorporation of B_4C significantly increased hardness, with the monolithic 50 wt.% B_4C composite exhibiting the highest values. Laminated configurations developed pronounced hardness gradients from the ductile Al6061 backing to the ceramic-rich strike face, demonstrating that layer design can be used to tailor through-thickness mechanical response.
- Transverse rupture strength (TRS) measurements revealed a strong dependence on both reinforcement fraction and laminate design. The monolithic S1 composite showed high initial stiffness but low rupture strain and a brittle fracture mode, whereas the laminated S2 and especially S3 specimens exhibited mixed-mode fracture with enhanced energy absorption. The S3 laminate (40 wt.% B_4C/Al6061) provided the most favorable combination of stiffness, TRS and ductility.
- Ballistic impact tests with 7.62 × 51 mm M80 projectiles demonstrated that the monolithic 50 wt.% B_4C composite failed predominantly by brittle fragmentation, extensive radial cracking and pronounced back-face spalling, which limited its ability to dissipate impact energy without transmitting severe damage to the rear surface.

- Laminated architectures markedly improved ballistic performance. The S2 laminate benefitted from the presence of a ductile Al6061 backing layer, which reduced rear-face damage despite brittle fracture in the 50 wt.% B_4C strike face. The S3 laminate, containing 40 wt.% B_4C in the strike layer, showed the most balanced ballistic response, characterized by a confined damage zone on the front face and controlled, non-catastrophic deformation on the back face.
- SEM analyses of post-impact cross-sections indicated that energy absorption in these composites occurs through a combination of projectile erosion and blunting, ceramic particle fracture, crack deflection and branching, interface debonding and plastic flow of the Al6061 matrix. These mechanisms were activated more efficiently in the laminated specimens than in the monolithic configuration, explaining the superior damage tolerance and back-face integrity of the layered designs.
- Among all tested materials, the S3 laminated Al6061–40%B_4C/Al6061 composite emerged as the most promising candidate for lightweight armor applications, offering an advantageous balance of hardness, structural continuity and ballistic energy absorption while mitigating the brittle failure modes associated with highly loaded monolithic B_4C-reinforced plates.

REFERENCES

[1] D. K. Koli, G. Agnihotri, and R. Purohit, "Advanced aluminium matrix composites: the critical need of automotive and aerospace engineering fields," *Materials Today: Proceedings*, vol. 2, no. 4–5, pp. 3032–3041, 2015.

[2] L. Gómez, D. Busquets-Mataix, V. Amigó, and M. D. Salvador, "Analysis of boron carbide aluminum matrix composites," *Journal of Composite Materials*, vol. 43, no. 9, pp. 909–917, 2009.

[3] D. K. Sharma, M. Sharma, and G. Upadhyay, "Boron carbide (B4C) reinforced aluminum matrix composites," *International Journal of Innovative Technology and Exploring Engineering*, vol. 8, no. 8, pp. 302–307, 2019.

[4] K. G. J. Christiyan, M. Rajanish, K. V. Pradeep, and S. Udayashankar, "Wear study of boron carbide particulate reinforced aluminium alloy composites," *Journal of The Institution of Engineers (India): Series D*, vol. 106, pp. 175–184, 2025.

[5] K. Singh, R. S. Rana, and A. Pandey, "Fabrication and mechanical properties characterization of aluminium alloy LM24/B4C composites," *Materials Today: Proceedings*, vol. 4, no. 2, pp. 3433–3441, 2017.

[6] V. V. Monikandan, K. Pratheesh, P. K. Rajendrakumar, and M. A. Joseph, "Towards the enhanced mechanical and tribological properties and microstructural characteristics of boron carbide particles reinforced aluminium composites: a short overview," *Johnson Matthey Technology Review*, vol. 66, no. 3, pp. 271–287, 2022.

[7] P. Madhukar, V. Mishra, N. Selvaraj, et al., "Influence of ultrasonic vibration towards the microstructure refinement and particulate distribution of AA7150–B4C nanocomposites," *Coatings*, vol. 12, no. 8, pp. 1–16, 2022.

[8] B. ByraReddy and T. P. Bharathesh, "Influence of B4C nanoparticles on microstructure and mechanical properties of Al6063 alloy composites," *AIP Conference Proceedings*, vol. 2396, 2021.

[9] D. Kumar, D. Kumar, and A. M. Tigga, "Processing of aluminium/boron carbide composites and functionally graded materials: a literature review," *SAE International Journal of Materials and Manufacturing*, vol. 14, no. 3, pp. 150–164, 2021.

[10] K. S. Kumar and V. S. Patnaik, "Experimental investigation on aluminium alloy composites for wear behaviour," in *ICEEOT 2016*, pp. 3065–3069, 2016.

[11] S. K. Choi, B. Seo, J. W. Kang, et al., "Microstructure and wear properties of aluminum metal matrix composite (Al6061–B4C) fabricated by stir casting process," *Archives of Metallurgy and Materials*, vol. 70, no. 2, pp. 389–396, 2025.

[12] K. G. J. Christiyan, et al., “Wear study of boron carbide particulate reinforced aluminium alloy composites,” *JIE Series D*, 2025.

[13] Beder, M. (2025). The effect of high B4C ratio on the improvement of mechanical properties and wear resistance of Al2024/B4C composites fabricated by mechanical milling-assisted hot pressing. *Ceramics International*, *51*(7), 9528-9547.

[14] S. Sharma, M. C. Gowrishankar, P. Hiremath, et al., “Tensile fractography of artificially aged Al6061–SiC+B4C hybrid composites,” *Materials Science Forum*, vol. 1006, pp. 44–49, 2020.

[15] P. K. Jena, S. G. Savio, K. S. Kumar, et al., “An experimental study on the deformation behavior of aluminium armour plates impacted by two different non-deformable projectiles,” *Procedia Engineering*, vol. 173, pp. 1104–1111, 2017.

[16] F. Y. Xu, Y. F. Zheng, Q. B. Yu, et al., “Experimental study on penetration behavior of reactive material projectile impacting aluminum plate,” *International Journal of Impact Engineering*, vol. 95, pp. 80–87, 2016.

[17] A. Kurzawa, D. Pyka, K. Jamroziak, et al., “Analysis of ballistic resistance of composites based on EN AC-44200 aluminum alloy reinforced with Al2O3 particles,” *Composite Structures*, vol. 183, pp. 62–72, 2018.

[18] S. J. Bless, D. L. Jurick, T. S. P., and M. A. Reynolds, “Ballistic impact behavior of SiC reinforced aluminum alloy matrix composites,” in *Shock Wave and High-Strain-Rate Phenomena in Materials*, 2023.

[19] X.-Y. Yue, Z.-N. Li, G.-Y. Guo, and H.-Q. Ru, “Preparation and ballistic resistance of B4C–Al foam composites with a bilayer structure,” *Journal of University of Science and Technology Beijing*, vol. 36, no. 2, pp. 150–156, 2014.

[20] Ş. Karabulut, H. Karakoç, M. Bilgin, et al., “A comparative study on mechanical and ballistic performance of functionally graded Al6061 composites reinforced with B4C, SiC, and Al2O3,” *Journal of Materials Research and Technology*, vol. 23, pp. 1479–1492, 2023.

[21] N. A. Rahman, S. Abdullah, M. F. Abdullah, et al., “Experimental and numerical investigation on layering configuration effect to laminated aluminium/steel panel subjected to high-speed impact,” *Metals*, vol. 8, no. 9, pp. 1–16, 2018.

[22] G. Saravanan, G. B. Bhaskar, U. Elaiyarasan, and R. M. Alagu, “Mechanical and microstructure behaviour of carbon and glass fibre reinforced Al2024-T3 laminated composite,” *Metallurgical Research and Technology*, vol. 120, no. 4, pp. 402–414, 2023.

[23] A. A. Ramadhan, A. R. Abu Talib, A. S. Mohd Rafie, and R. Zahari, "Behaviour of fibre–metal laminates under high velocity impact loading with different stacking sequences of Al alloy," *Applied Mechanics and Materials*, vol. 225, pp. 56–61, 2012.

[24] H. Karakoç, H. Çinici, Ş. Karabulut, and R. Çıtak, "Fabrication of AA6061/B4C composites and investigation of ballistic performances," in *8th International Conference on Mechanical and Aerospace Engineering (ICMAE)*, pp. 261–266, 2017.

[25] M. Ozer, S. İ. Aydogan, A. Ozer, H. Cinici, and E. Ayas, "Influence of spark plasma sintering and conventional sintering on microstructure and mechanical properties of hypereutectic Al-Si alloy and hypereutectic Al-Si/B_4C composites," *Kovove Mater.*, vol. 60, no. 3, pp. 171–179, 2022.

[26] L. Xu, Q. Gao, L. Tang, Y. Yao, S. Sun, and C. Li, **"**Numerical simulation study on hot pressing of ceramic/metal powders**,"** *Mater. Today Commun.*, vol. 40, pp. 109721, 2024.

[27] A. K. Bodukuri, K. Eswaraiah, K. Rajendar, and P. V., "Investigation of optimum compacting parameters for aluminium, SiCP and B_4C composites," *Mater. Today Proc.*, vol. 5, pp. 26866–26872, 2018.

[28] Göçer & Karamış (2021) A. Gocer and M. B. Karamis, **"**An investigation on the tribological behaviors of Al6061–B4C metal matrix composites**,"** *Protection of Metals and Physical Chemistry of Surfaces*, vol. 57, no. 3, pp. 579–588, 2021.

[29] Chen et al. (2023) X. Chen, X. Guo, Z. Liu, X. Wei, and S. Li, "Mechanical properties and thermal stability of B4C/7A04Al composite fabricated by powder metallurgy**,"** *Journal of Alloys and Compounds*, vol. 940, pp. 168871, 2023.

[30] Melgarejo et al. (2006) Z. H. Melgarejo, O. M. Suárez, and K. Sridharan, **"**Wear resistance of a functionally graded aluminum matrix composite**,"** *Scripta Materialia*, vol. 55, no. 1, pp. 95–98, 2006.

[31] M. C. Şenel and M. Gürbüz, "Investigation on mechanical properties and microstructure of B_4C/graphene binary particles reinforced aluminum hybrid composites," *Metals and Materials International*, vol. 27, pp. 2438–2449, 2021.

[32] M. C. Şenel, Y. Kanca, and M. Gürbüz, "Reciprocating sliding wear properties of sintered Al–B_4C composites," *International Journal of Minerals, Metallurgy and Materials*, vol. 29, no. 6, pp. 1261–1269, 2022.

[33] Y. Pazhuhanfar, Sh. Bagherpour Vlashani, and B. Eghbali, "Fabrication and characterization of microstructure and mechanical properties Al6061 matrix

composite reinforced with B4C particles,"*Metallogr. Microstruct. Anal.*, 2025, doi: 10.1007/s13632-025-01276-1.

[34] P. Ranjitha, D. S. Bhavan, B. S. Ajaykumar, T. H. Raju, B. Manjunatha, and S. Udayashankar, "Study of wear behavior of silicon carbide and boron carbide reinforced aluminium alloy (Al6061) matrix composites," *J. Inst. Eng. India Ser. D*, vol. 106, no. 1, pp. 207–214, Jan.–Apr. 2025, doi: 10.1007/s40033-023-00625-0.

[35] Y. Wang *et al.*, "Dynamic compressive response and impact resistance of bioinspired nacre-like 2024Al/B4C composites," *Mater. Sci. Eng. A*, vol. 831, 142261, 2022, doi: 10.1016/j.msea.2021.142261.

[36] Z. Zhou, G. Wu, L. Jiang, R. Li, and Z. Xu, "Analysis of morphology and microstructure of B4C/2024Al composites after 7.62 mm ballistic impact," *Mater. Des.*, vol. 63, pp. 658–663, 2014, doi: 10.1016/j.matdes.2014.06.044.

[37] R.-W. Zhang *et al.*, "Interfacial behavior and damage mechanism of Al-B4C/Al laminated composites under ballistic impact," *Mater. Charact.*, vol. 215, 114213, 2024, doi: 10.1016/j.matchar.2023.114213.

Chapter 6

USE OF NEW MATERIALS IN GaN AND AlGaN HEMT STRUCTURES: GRAPHENE AND HEXAGONAL BORON NITRIDE

Osman ÇİÇEK[1], Yasin DOĞAN[2]

1. INTRODUCTION

Gallium nitride (GaN) and aluminum gallium nitride (AlGaN)-based high electron mobility transistors (HEMTs) have emerged as transformative technologies in high-power electronics, RF communication systems, and optoelectronic devices. However, critical challenges such as self-heating, electrical leakage, and interface defects continue to limit their performance. Innovative material integration strategies offer promising pathways to overcome these limitations.

This review examines the integration of two-dimensional (2D) materials specifically graphene and hexagonal boron nitride (h-BN) into GaN/AlGaN HEMT structures, exploring how these materials enhance device efficiency, reliability, and functionality. The discussion encompasses a comprehensive range of applications: from graphene's roles in thermal management and transparent electrode fabrication to h-BN's implementation as gate dielectric and buffer layer, culminating in strategies for scalable production of hybrid heterostructures.

[1] Department of Electrical and Electronics Engineering, Kastamonu University, Kastamonu, Turkey; ocicek@kastamonu.edu.tr (ORCID: 0000-0002-2765-4165)
[2] IT Department, Kastamonu University, Kastamonu, Turkey; yasindogan@kastamonu.edu.tr (ORCID: 0000-0002-3065-9864)

Figure 1: Advanced GaN HEMT technology integration with 2D materials (graphene and hexagonal boron nitride, h-BN) for next-generation applications.

While GaN/AlGaN HEMTs are inherently suited for high-power and RF applications owing to their wide bandgap and high electron saturation velocity, phenomena such as self-heating, current collapse, and gate leakage current pose significant performance constraints. This chapter addresses these challenges by introducing the exceptional properties of graphene and h-BN including atomic-scale thickness, high thermal conductivity, and van der Waals bonding and demonstrates how these characteristics enable GaN-based systems to transcend conventional performance boundaries.

By synthesizing findings from extensive literature, this work illustrates how 2D material integration can revolutionize applications spanning 5G/6G communication technologies, electric vehicles, and space electronics. Current obstacles, particularly interface engineering and scalability challenges, are critically assessed alongside future research directions, establishing a roadmap for advancing GaN technology into new frontiers.

1.1. Overview of GaN/AlGaN HEMT Technology

AlGaN/GaN heterostructure-based high-electron-mobility transistors (HEMTs) are premier devices for high-power and high-frequency applications, leveraging superior material attributes such as a wide bandgap (3.4 eV for GaN), high critical electric field (~3.3 MV/cm), and elevated electron saturation velocity. The two-dimensional electron gas (2DEG) at the AlGaN/GaN interface arising from spontaneous and piezoelectric polarization delivers high sheet carrier densities (~10^{13} cm^{-2}) and electron mobilities (>1500 $cm^2/V{\cdot}s$). Persistent challenges encompass self-heating, surface trapping-induced current collapse, gate leakage and breakdown voltage constraints, elevated thermal resistance, and ohmic contact resistances (~0.2–0.5 Ω·mm) in standard Ti/Al/Ni/Au metallizations. Recent breakthroughs include quaternary InAlGaN-barrier GaN HEMTs with 100 nm gate lengths exhibiting maximum drain currents of 1940 mA/mm, breakdown voltages of 1513 V, and drain saturation current densities of 3.41 kA/cm^2. Plasma-assisted molecular beam epitaxy (PAMBE) on Si substrates has yielded AlGaN/GaN HEMTs with 80 nm gates achieving cutoff frequencies (f_T) of 200 GHz and maximum oscillation frequencies (f_{max}) of 308 GHz. These milestones underscore GaN's transformative potential for 5G/6G communications, radar systems, and power electronics (Talukder et al., 2025; Repaka et al., 2024).

1.2. Advantages of 2D Materials

Two-dimensional (2D) materials like graphene and hexagonal boron nitride (h-BN) profoundly enhance GaN HEMT performance through their atomic-scale thickness, exceptional thermal conductivities, superior electrical traits, and van der Waals bonding, which enable seamless integration with or substitution of conventional 3D materials. Graphene boasts in-plane thermal conductivity of ~3000–5000 W/m·K (suspended single layer), while nanocrystalline h-BN reaches 600–1300 W/m·K orders of magnitude above GaN's bulk value of 130–230 W/m·K. The modest ~1.8% lattice mismatch between graphene and h-BN further eases heterostructure assembly. These attributes yield pivotal gains in thermal dissipation, interface quality, and overall device efficiency (Balandin, 2011; Li et al., 2025). GaN/AlGaN HEMTs excel in power/RF via high 2DEG density/mobility, with 2D integrations like graphene/h-BN addressing thermal bottlenecks (~5x κ boost) and enabling f_T/f_{max} >200/300 GHz.

2. APPLICATIONS OF GRAPHENE IN GaN HEMT STRUCTURES

Graphene, leveraging its exceptional thermal conductivity, optical transparency, and electrical conductivity, serves multifaceted roles in GaN HEMTs. This section explores diverse applications, from channel temperature mitigation in heat dissipation to high-responsivity UV photodetectors via transparent electrodes, passivation for gate leakage reduction, and thermal-process-free Cr/graphene ohmic contacts. It also highlights advanced concepts like hot electron transistors, underscoring graphene's transformative potential.

2.1. Thermal Management and Heat Dissipation

Graphene's superior in-plane thermal conductivity (~3000–5000 W/m·K at room temperature) roughly 10–20 times that of GaN positions it as a premier material for HEMT thermal management. The graphene-graphite quilt approach, developed by Yan et al., entails depositing few-layer graphene (FLG) films atop drain electrodes of AlGaN/GaN HEMTs to efficiently extract heat from the critical gate-drain hotspot. This yields ~12% enhancement in saturation current density, channel temperature reductions of ~20–32 °C, and a drop in DC-pulsed current discrepancy from ~21% to ~8%, markedly alleviating self-heating-induced performance degradation (Yan et al., 2012; Balandin, 2011). Dual-layer SiN_x stressor passivation has been shown to suppress current collapse by ~90% (Deng et al., 2023). Graphene-based thermal management provides complementary benefits by reducing self-heating. Emerging encapsulated architectures propose graphene layers both beneath the substrate (as a heat sink) and atop the device (for source/drain/gate stabilization), with h-BN interlayers promoting GaN adhesion and preserving structural integrity under high-power stress, thereby bolstering reliability and thermal uniformity (Moon et al., 2025; Francis & Kuball, 2022; Bao et al., 2023). Graphene offers one of the most effective solutions to the critical self-heating limitation of GaN HEMTs. A 20–32 °C reduction in channel temperature increases maximum power handling capacity by 12–20% and enables higher power densities (typically 20–40% improvement over conventional cooling methods) in thermally constrained applications such as 6G RF power amplifiers and electric-vehicle inverters. In practice, this translates to 12–30% higher output power density, as demonstrated by Yan et al. (2012).

2.2. Transparent Electrode Applications

Graphene's ~97.7% optical transparency and robust conductivity render it an optimal electrode for UV photodetectors, outperforming Ni/Au counterparts with elevated photocurrents, responsivities up to ~250 A/W, sensitivities ~3.55

$\times 10^6$, detectivities ~1.91×10^{14} cm $Hz^{1/2}$ W^{-1}, and dark currents plummeting from μA to pA regimes (Pandit et al., 2023; Pandit et al., 2020; Shin & Choi, 2018; Kruszewski et al., 2024). In the graphene/p-GaN mesa configuration by Pandit et al., interdigitated graphene finger electrodes atop p-GaN mesas effectively quench the 2DEG, while their transparency maximizes active-region illumination, yielding exceptional UV/visible rejection ratios (Pandit et al., 2023). Graphene integration into AlGaN/GaN heterostructures further enables dual-mode (photovoltaic/photoconductive) UV photodetectors: low-bias operation affords rapid response times with modest responsivities, escalating to 10.9 A/W and a 760 gain factor at higher biases (Pandit et al., 2020). For LED applications, graphene transparent conductive electrodes (TCEs) supplant ITO in GaN-based devices, offering superior heat dissipation, high-temperature/radiation resilience, mechanical flexibility for bendable designs, and low sheet resistance for uniform current distribution. Notable implementations include enhanced light extraction in GaN/AlGaN nanocolumn flip-chip UV LEDs (Mulyo et al., 2021), electron-tunneling LEDs via graphene/p-AlGaN/p-GaN heterostructures with elevated external quantum efficiencies (Feng et al., 2019), and up to ~50% light extraction boosts through nanowire photonic crystal integration in AlGaN LEDs (Du et al., 2019). Graphene transparent electrodes deliver astronomical responsivities of 200–250 A/W with pA-level dark currents in UV photodetectors and boost light-extraction efficiency in GaN-based LEDs by up to 50% – far surpassing conventional Ni/Au or ITO. The true breakthrough advantage is the simultaneous combination of optical transparency, superior thermal conductivity, radiation hardness, and mechanical flexibility. This unique mix enables practical deployment of flexible/wearable UV sensors, radiation-tolerant imaging systems for space applications, and highly efficient next-generation UV/deep-UV LEDs for sterilization, water purification, and biosensing – capabilities simply unattainable with traditional metallic or ITO electrodes.

2.3. Graphene in Gate Electrode and Passivation

Studies by the SUSTech team demonstrate that metal/graphene gate structures in p-GaN HEMT devices suppress gate leakage current by up to two orders of magnitude, enhance gate breakdown voltage, and mitigate reactions between metal and p-GaN, thereby improving reliability and commercial viability; graphene acts as an effective barrier, yielding superior performance over conventional devices (Zhou et al., 2020). Fluorinated graphene passivation significantly reduces gate leakage current through modified transport

mechanisms (e.g., suppressed thermionic emission and variable-range hopping) and strengthens the overall electric field distribution at the interface; it is synthesized via plasma-induced chemical bonding of fluorine atoms to the graphene surface (Ding et al., 2023). In AlGaN/GaN FinFET applications, graphene Schottky barriers deliver low-noise characteristics, minimizing 1/f noise (trap density ~10^{19} eV^{-1} cm^{-3}) and enhancing RF/sub-THz performance for high-frequency electronics (Dub et al., 2022).

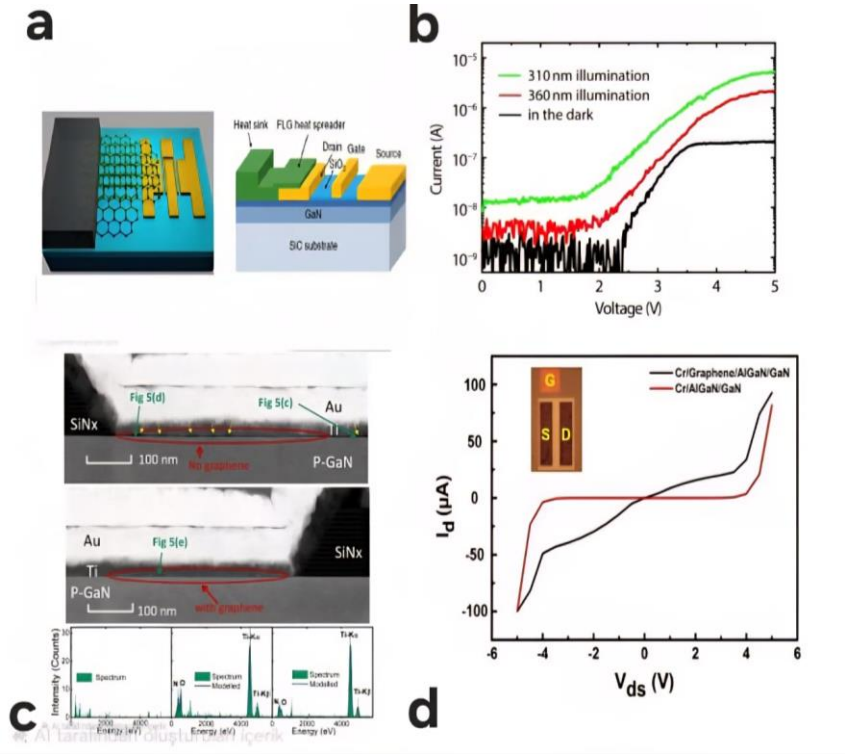

Figure 2. Various applications of graphene in AlGaN/GaN-based devices. (a) Adapted from Yan et al. (2012): Schematic of few-layer graphene (FLG)/graphite quilt heat spreader for thermal management of high-power GaN transistors. (b) Reprinted from Pandit et al. (2020): I-V characteristics of an ultraviolet photodetector with transparent graphene electrodes under 310 nm and 360 nm illumination and in the dark. (c) Adapted from Zhou et al. (2020): Cross-sectional TEM images and EDS analysis comparing metal/p-GaN interfaces with and without graphene interlayer. (d) Reprinted from Cuong et al. (2024): Comparison of I_{DS}–V_{DS} characteristics between Cr/graphene/AlGaN/GaN and conventional Cr/AlGaN/GaN ohmic contacts, demonstrating low-temperature ohmic behavior.

2.4. Graphene Ohmic Contacts

Ohmic contact quality is a critical factor directly affecting the performance of AlGaN/GaN HEMTs; conventional Ti/Al/Ni/Au metallization schemes require high annealing temperatures of 800–900°C and cause Au diffusion problems (Qin et al., 2004; Garbe et al., 2023). A comparative analysis of ohmic contact technologies (Table 1) reveals that graphene-based approaches offer significant advantages over conventional methods in terms of contact resistance, processing temperature, and material compatibility. Cuong et al. developed thermal-process-free Cr/Au/graphene ohmic contacts in AlGaN/GaN HEMTs; a graphene nanoflakes solution (0.025 mg/mL concentration) was applied by spray coating on the source/drain regions, followed by Cr/Au (30/100 nm) deposition via electron beam evaporation. The synthesized graphene nanoflakes, produced via liquid-phase exfoliation of graphite in NMP solvent, predominantly consist of 4–5 layers (thickness ~2–3 nm, as confirmed by AFM and TEM). This Cr/graphene combination acts like a doped n-type semiconductor (with a non-zero bandgap at the Cr/graphene interface) in contact with the AlGaN/GaN heterostructure, enabling carrier transport to the AlGaN layer and exhibiting ohmic-like drain characteristics between –4 V and 4 V drain-source voltage (VDS), while graphene-free reference samples (Cr/Au only) show Schottky behavior in the same VDS range. The specific contact resistance density (ρc) is 2.5 × 10−3 Ω·cm² (measured via transfer length method, TLM), which is higher than that of conventional annealed HEMTs (~10−5 Ω·cm²) but can be improved by optimizing the graphene solution concentration, sonication/exfoliation parameters, and spray coating conditions; this low resistance is achieved without any high-temperature annealing (unlike standard Ti/Al/Ni/Au contacts requiring >850 °C). Advantages include lower cost and less complex fabrication (solution-based graphene avoids high-temperature CVD growth and transfer), low-temperature processing (compatible with temperature-sensitive substrates), and high potential for scalable production of AlGaN/GaN-based microelectronic and optoelectronic devices/sensors for CVD graphene insertion. (Cuong et al., 2024; Park et al., 2013,).In literature, Schottky barrier height for graphene/AlGaN contacts is reported as 1.25–1.53 eV (for Al mole fractions 0.15–0.4), while Cr addition effectively overcomes this barrier and creates an n-type doping-like effect. Future development areas include adjusting graphene solution concentration, optimizing spraying parameters, controlling graphene layer number, and exploring alternative metal/graphene combinations; potential applications are RF HEMTs for 5G communication systems, high-power electronics, optoelectronic sensors, and GaN-based microelectronic devices. Graphene ohmic contacts offer a promising path for next-generation GaN HEMT technology with low-temperature processing, Au-free structure, and scalable fabrication potential (Pandit et al., 2016).

Table 1 – Ohmic Contact Performance Comparison: Graphene-Based vs. Conventional Approaches

Contact Type	Contact Resistance ($\Omega \cdot cm^2$)	Annealing Temperature	Au Content	Reference(s)
Conventional Ti/Al/Ni/Au	$\sim 10^{-7}$	800–900°C	Yes	Qin et al. (2004); Garbe et al. (2023)
Cr/Graphene (solution-processed nanoflakes)	2.5×10^{-3}	Not required	No	Cuong et al. (2024);
Ti/Al/Ni/Ti	$\sim 8 \times 10^{-6}$	850–950°C	No	Hsu et al. (2024)
TixAly Alloy	$\sim 1.6 \times 10^{-5}$	550°C	No	You et al. (2021)
Au-free V/Al/Ti/TiN	$< 2.4 \times 10^{-7}$	800°C	No	Garbe et al. (2023)

2.5. Advanced Graphene Applications

Beyond basic HEMT components, graphene offers new paradigms for next-generation device architectures. Zubair et al. developed a high-performance GaN emitter with graphene-base hot electron transistor (HET), where the emitter is GaN, the base is graphene (~0.34 nm thick), and the collector is a van der Waals heterostructure; hot electrons tunnel from the GaN emitter through the graphene base to the collector, the atomic thinness of the graphene base provides low base resistance, and van der Waals bonds create clean interfaces, achieving high current gain, low base resistance, fast switching, and utilization of GaN's high electron velocity this offers higher frequency performance, lower power consumption, and compact design compared to conventional bipolar transistors (Zubair et al., 2017). Perumal et al. demonstrated bidirectional functionality of vertically stacked graphene/MoS_2/SiO_2/p-GaN heterostructures; the layer sequence is graphene (top electrode), MoS_2 (single-layer n-type 2D semiconductor), SiO_2 (10 nm thin insulation layer), and p-GaN (substrate), providing self-powered operation in photodetector mode with broad spectral response (high absorption at 633 nm), high responsivity (~10.4 A/W), high detectivity (1.1×10^{10} Jones), 30% external quantum efficiency, and fast response time (~0.1–0.25 s rise/fall), and strong electroluminescence at ~680 nm with low turn-on voltage (~1.0 V) in light-emitting (LED) mode; the thin SiO_2 layer controls charge injection, facilitates carrier accumulation and recombination via tunneling, van der Waals interfaces (graphene-MoS_2 and MoS_2-SiO_2) offer low defect density, and the p-n heterojunction (p-GaN/n-MoS_2) creates an internal electric field for efficient charge separation; potential applications include high-performance integrated optoelectronic circuits, self-powered sensors, low-power light-emitting devices, and multifunctional nanoscale systems (Perumal et al., 2017). Kumar et al. demonstrated improved

thermionic emission and low 1/f noise characteristics in exfoliated graphene/GaN Schottky barrier diodes; the layer sequence is exfoliated graphene (top electrode) and n-type GaN (substrate), providing high barrier homogeneity (~0.60–0.72 eV) in Schottky diode mode, ideality factor 1.33, two orders of magnitude reduction in 1/f noise (compared to Ni/GaN), increased thermionic emission current, consistent barrier over wide temperature range (~175 K–high T) with temperature-dependent I-V characteristics, and low defect density with clean contacts due to van der Waals interfaces; barrier height can be tuned with graphene layer number, RF performance is supported by low capacitance, fast switching, and high cutoff frequency; potential applications include low-noise RF detectors, mixer circuits, frequency multipliers, power rectifiers, and transparent electronics (Kumar et al., 2016). Ryzhii et al. modeled and evaluated graphene-based vertical hot-electron transistors (vertical hot-electron graphene-base transistors – HET-GBT) as resonant plasmonic terahertz (THz) detectors; the device structure includes undoped graphene base (GL-base) separated by thin barrier layers between n-type emitter and collector regions, with bias voltages (V_E and V_C) applied to the GL-base creating a 2D hole gas. Hot electrons tunnel-inject from the emitter, pass through the graphene base, and reach the collector; thanks to graphene's linear Dirac spectrum and high plasma wave velocity ($s = 2.5–5.0 \times 10^8$ cm/s, higher than v_F), self-consistent plasmonic oscillations are excited in the GL-base. These oscillations create sharp resonance peaks in the THz frequency range (1–5 THz), dramatically increasing detector responsivity (R_ω) at these frequencies (e.g., high Q-factor at collision frequency $\nu = 1–2 \times 10^{12}$ s^{-1}). Responsivity frequency dependence can be controlled with bias voltages (via hole density Σ_0 and plasma velocity s), lateral dimensions ($2L = 1.0–1.4$ μm), and momentum relaxation time τ; nonlinearity of emitter tunnel current and low capture probability ($p \ll 1$) enhance rectified dc signal (proportional to radiation intensity) and transconductance (G_ω). These features provide high-quality plasmonic resonances even at room temperature, making HET-GBT superior to conventional heterostructure-based plasmonic THz detectors (QW-HETs, etc.) and outperforming other graphene-structured detectors; the main application is efficient resonant detection over a wide frequency range (THz regime) (Ryzhii et al., 2015). Future directions include hybrid device architectures (graphene HET + conventional HEMT integration, monolithic integrated circuits, 3D heterostructure arrays), new functionalities (quantum dot integration, plasmonic applications, spintronic devices), and scalable fabrication (CVD-grown graphene usage, wafer-scale transfer techniques, CMOS-compatible processes); current challenges are graphene layer number control, interface quality improvement, large-area uniformity, and long-term stability. Advanced graphene applications push GaN

technology beyond traditional limits, offering new device concepts and performance regimes.

3. APPLICATIONS OF HEXAGONAL BORON NITRIDE (h-BN)

h-BN, with its wide bandgap, high thermal conductivity, and atomically smooth surface, is an excellent insulator and interface improver in GaN HEMTs. This section examines h-BN's contributions, from reducing dislocation density as a buffer layer via van der Waals epitaxy to reducing leakage current by six orders of magnitude as a gate dielectric, reducing thermal resistance by five times with passivation, and facilitating mechanical transfer for flexible devices. It also covers growth techniques such as CVD and MOCVD and performance-enhancing roles in optoelectronics.

3.1. Properties and Advantages of h-BN

Hexagonal boron nitride (h-BN), also known as white graphene, is a 2D material offering many critical advantages in GaN HEMT structures; key material properties include excellent electrical insulation with bandgap ~6 eV, thermal conductivity ~600–1300 W/m·K (for nanocrystalline h-BN), dielectric constant 3–4 (similar to SiO_2), very high breakdown field (>10 MV/cm), and optical transparency of 99% (over a wide wavelength range). Surface properties include atomically smooth structure without dangling bonds, chemical inertness, and high-temperature stability (up to 800°C in air); for van der Waals epitaxy, ~1.8% lattice mismatch with graphene, weak van der Waals interactions, and strain-engineering capability (Xu et al., 2025; Wu et al., 2016). h-BN uniquely combines the best attributes of a gate dielectric, passivation layer, thermal spreader, and transferable buffer—far surpassing SiN_x, Al_2O_3, or SiO_2 in a single material—making it the most promising 2D enabler for next-generation high-performance, reliable, and cost-effective GaN power and optoelectronic devices.

3.2. h-BN as Buffer Layer

The use of h-BN as a buffer layer in GaN HEMTs enables van der Waals epitaxy and provides significant performance improvements. Sundaram et al. produced AlGaN/AlGaN multiple quantum well heterostructures using h-BN buffered sapphire substrates, achieving wafer-scale growth of 20-period $Al_{0.58}Ga_{0.42}N/Al_{0.37}Ga_{0.63}N$ MQWs with deep UV emission at 299 nm; h-BN's vdW epitaxy addresses lattice mismatch in Al-rich III-nitrides, enhances structural quality (third-order satellite peaks in HRXRD, high-quality interfaces in TEM), enables mechanical lift-off and transfer while preserving optical properties, and supports free-standing/flexible devices for UV applications (Sundaram et al., 2019).

Moon et al. developed wafer-scale AA-stacked h-BN on GaN substrates; using metal-organic chemical vapor deposition (MOCVD) with high-temperature growth (>1400°C) and atomic-precision control, AA-stacked arrangement (direct layer-on-layer), lattice constant of 2.504 Å (perfect match with GaN), and monocrystalline quality were achieved; h-BN serves as a mechanical release layer, substrates can be reused after wafer transfer, enabling low-cost GaN-on-GaN device production; advantages include high crystal quality, low defect density, scalable production, and substrate recycling (Moon et al., 2025). Growth dynamics show that h-BN buffer layers offer unique advantages for GaN growth; van der Waals interactions reduce mechanical strain transmission and minimize thermal expansion mismatch effects, h-BN surface provides controlled GaN nucleation (layer-by-layer growth instead of island growth), and defect engineering reduces threading dislocation density while lowering point defect concentration (Moon et al., 2021; Wu et al., 2016).

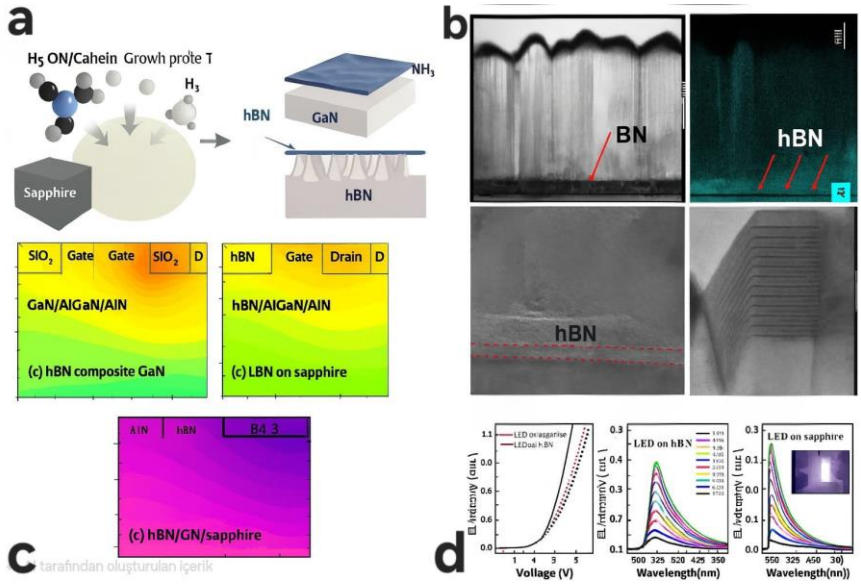

Figure 3. Hexagonal boron nitride (h-BN) as a multifunctional enabler in GaN technology: (a) Wafer-scale, AA-stacked monocrystalline h-BN directly grown on GaN substrate via ion-assisted metal-organic vapor phase epitaxy (MOVPE). Perfect atomic alignment and van der Waals stacking between h-BN and GaN layers enable seamless integration for high-performance GaN-based devices (adapted from Moon et al., Nature Materials, 2025). (b) Large-area, transferable 2D h-BN grown on sapphire by MOVPE, demonstrating mechanical release and lift-off capability. The free-standing h-BN film serves as an ideal buffer/seeding layer for subsequent AlGaN/GaN heterostructure growth (adapted from Sundaram et al., Journal of Crystal Growth, 2019). (c) Significant reduction of self-heating in GaN high-electron-mobility transistors (HEMTs) through h-BN passivation and substrate transfer onto diamond. Simulated thermal resistance drops from ~5 K·mm/W (conventional) to <1 K·mm/W with h-BN/diamond composite substrate configuration (adapted from Tijent et al., Materials Science and Engineering: B, 2024). (d) Optoelectronic applications of h-BN in GaN-based near-ultraviolet light-emitting diodes (NUV-LEDs). Electroluminescence spectra and current–voltage–luminance characteristics of NUV-LEDs grown on h-BN intermediate layers, showing improved crystal quality and light extraction efficiency compared to conventional sapphire substrates (adapted from Park & Seo, Materials, 2023).

3.3. h-BN in Gate Dielectric and Passivation

h-BN passivation provides a significant reduction in self-heating effects in GaN-based devices. Simulations conducted by Tijent et al. (2024) demonstrate that the high in-plane thermal conductivity of h-BN (360–751 W/m·K) substantially enhances heat dissipation. When combined with a diamond substrate, this approach enables optimal thermal management, reducing lattice temperature from 507 K to 372 K, achieving approximately 5× reduction in thermal resistance, increasing power density, improving device reliability, and minimizing thermal degradation (Tijent et al., 2024). Whiteside et al. (2021) reported that thin h-BN films grown by microwave plasma-enhanced chemical vapor deposition (MW-PECVD) on AlGaN/GaN MIS-HEMTs reduce gate leakage current by 2–3 orders of magnitude, increase breakdown voltage, and significantly suppress hysteresis. These structures exhibit a dielectric constant of 3.5–4.0, large band offsets with the GaN heterostructure, and low interface state density (below 10^{13} cm^{-2} eV^{-1}) (Whiteside et al., 2021). Gerbedoen et al. (2009) demonstrated AlGaN/GaN MIS-HEMTs using h-BN as the gate dielectric, achieving low gate leakage, very low interface state density (~5 × 10^{11} cm^{-2} eV^{-1}), high gate capacitance, and improved transconductance (g_m). Subsequent studies have explored α-BN/h-BN double-layer dielectrics, where the outer α-BN layer provides a high dielectric constant and the inner h-BN layer ensures low leakage current. This synergistic structure results in reduced drain-induced barrier lowering (DIBL) and supports high power density operation. A comparison of key properties of h-BN and other common gate dielectric and passivation materials is presented in Table 2.

Table 2 – Comparative Properties of Gate Dielectric and Passivation Materials

Property	h-BN	SiN_x	SiO_2	Al_2O_3
Dielectric Constant	3–4	7–8	3.9	9–10
Bandgap (eV)	5.9–6.0	~5.0	9.0	8.8
Thermal Conductivity (W/m·K)	360–751	15–30	1.4	30–35
Interface State Density	Very Low	Medium	Medium-High	Low
Temperature Stability	Excellent	Good	Medium	Good
Van der Waals Surface	Yes	No	No	No

3.4. Transfer Technology and Flexible Devices

The weak van der Waals bonds of h-BN enable the mechanical transfer of GaN-based devices from growth substrates. GaN heterostructures are epitaxially grown on h-BN buffer layers via van der Waals epitaxy, allowing chemical or mechanical separation at the h-BN interface; the resulting GaN membrane can

then be exfoliated and transferred to alternative substrates. Sundaram et al. (2019) demonstrated wafer-scale growth and successful mechanical exfoliation of AlGaN/GaN multiple quantum well structures on large-area 2D h-BN-buffered sapphire substrates, highlighting the potential for crack-free transfer at scales up to several centimeters. This approach supports applications in flexible electronics, GaN-on-heterogeneous-substrate architectures, substrate reuse, and cost-effective fabrication of high-performance III-nitride devices, such as deep UV LEDs with reduced dislocation densities and improved structural quality (Sundaram et al., 2019). Meanwhile, the incorporation of h-BN as a transferable van der Waals buffer layer not only improves the crystalline quality of GaN epitaxy but also enables substrate-independent, reusable, and flexible III-nitride device technology, paving the way for next-generation low-cost, high-performance, and mechanically adaptable optoelectronic and electronic systems.

3.5. Optoelectronic Applications

h-BN serves as a critical intermediate (interlayer) material that enables successful epitaxial growth of gallium nitride (GaN) in near-ultraviolet light-emitting diodes (NUV-LEDs). Park and Seo (2023) demonstrated the direct growth of high-quality GaN layers on h-BN/sapphire substrates using a conventional low-temperature GaN buffer layer, achieving a crack-free, mirror-like, and atomically flat GaN surface morphology with a thickness of 3.7 μm. Compared to graphene interlayers, h-BN provided significantly better and more uniform GaN nucleation due to the partial ionic character of B–N bonds, which facilitates Ga adatom attraction and promotes ordered two-dimensional growth. Although the crystallinity of GaN grown on h-BN was slightly inferior to that of conventional GaN on sapphire (evidenced by broader XRD rocking curve FWHM and lower near-band-edge PL intensity), a complete InGaN/AlGaN NUV-LED structure was successfully grown on the h-BN interlayer and fabricated into operational devices. These NUV-LEDs exhibited excellent rectifying behavior, bright electroluminescence in the 370–400 nm range, with good current–voltage characteristics and light output performance. The atomic-scale smoothness of h-BN, combined with its van der Waals interface, effectively suppresses strain relaxation, reduces threading dislocation density, minimizes non-radiative recombination centers, and improves overall crystal quality and device performance compared to direct growth on sapphire, confirming h-BN's strong potential as an intermediate layer for high-performance GaN-based optoelectronic devices (Park and Seo, 2023). In conclusion, the use of hexagonal boron nitride (h-BN) as an intermediate layer represents a highly promising pathway for overcoming the longstanding

heteroepitaxial challenges in GaN-based NUV-LEDs. By leveraging the unique combination of h-BN's atomically smooth van der Waals surface and partial ionic B–N bonding, high-quality, low-defect GaN epitaxy becomes achievable even on foreign substrates such as sapphire. While crystallinity remains marginally lower than that of conventional sapphire-grown GaN, the successful fabrication and robust optoelectrical performance of fully functional NUV-LEDs prove that h-BN interlayers can deliver device-grade material without requiring native GaN substrates. This approach not only enhances crystal quality and light extraction efficiency but also opens the door to flexible, transferable, and large-area III-nitride optoelectronics, making h-BN a key enabling material for next-generation ultraviolet and visible LED technologies.

3.6. h-BN Growth Techniques

Scalable and high-quality growth of hexagonal boron nitride (h-BN) is essential for its widespread integration into GaN high-electron-mobility transistor (HEMT) technology, enabling superior dielectric passivation, thermal management, and interface quality. Xu et al. (2025) reviewed advancements in chemical vapor deposition (CVD) for h-BN growth directly on insulating substrates, achieving uniform monolayer coverage and multilayer films with enhanced dielectric properties at temperatures of 1000–1400°C. These processes utilize atmospheric or low-pressure CVD (LPCVD) with precursors such as ammonia-borane (BH_3NH_3) or borazine ($B_3N_3H_6$), and carrier gases including H_2, Ar, or N_2, thereby minimizing transfer-related defects and facilitating seamless device integration. Wu et al. (2016) demonstrated large-area synthesis of high-quality monolayer h-BN via LPCVD on Cu foil, achieving a 25-inch roll with a growth area equivalent to a 63.5 cm diameter wafer and uniformity exceeding 95% (confirmed by Raman spectroscopy). The growth mechanism involves an initial nucleation phase (h-BN island formation on Cu foil), followed by lateral growth and coalescence to form a continuous monolayer film with aligned single-crystal domains. Quality metrics include a characteristic Raman E_2g mode at ~1370 cm^{-1}, atomic force microscopy (AFM) surface roughness below 0.3 nm, transmission electron microscopy (TEM) confirmation of hexagonal crystal structure, and robust transfer methods such as PMMA-assisted wet transfer, electrochemical delamination, and clean protocols yielding contamination levels under 1%. Metal–organic chemical vapor deposition (MOCVD) offers distinct advantages for h-BN growth, including compatibility with existing GaN epitaxy infrastructure, high crystal quality, in-situ monitoring, and precise doping control; however, it faces challenges such

as elevated temperature requirements (>1400°C), precursor optimization, and higher costs.

Substrate selection is pivotal in optimizing h-BN growth outcomes. For instance, sapphire provides excellent high-temperature stability but induces defect formation due to lattice mismatch with h-BN (Xu et al., 2025). SiO_2 ensures CMOS compatibility yet yields lower crystal quality owing to weak precursor adsorption. Cu foil excels in enabling large-area synthesis but necessitates post-growth transfer (Wu et al., 2016). GaN substrates offer near-perfect lattice matching for epitaxial alignment but are constrained by their high cost and limited availability (Moon et al., 2025). These trade-offs underscore the need for application-specific substrate optimization: Cu foil is favored for scalable, cost-effective production, while GaN substrates are ideal for premium, high-fidelity integration in advanced HEMTs.

Future development directions include low-temperature growth processes, electrically active doping (n-type, p-type), reduction of defect density, scalable transfer techniques, minimization of metal contamination, plasma-enhanced CVD (PECVD), atomic layer deposition (ALD)-like approaches, and hybrid growth techniques; maturation of h-BN growth technologies is of critical importance for commercial applications of h-BN integration in GaN HEMTs.

4. GRAPHENE AND h-BN HYBRID HETEROSTRUCTURES

The hybrid combination of graphene and h-BN provides synergy of conductivity and insulation, delivering superior performance in GaN HEMTs. This section covers sequential CVD for wafer-scale stacking, clean transfer protocols, and van der Waals interface engineering. Hybrid structures achieve striking results. Low-cost reduced graphene oxide (RGO)-based alternatives and monolithic integration challenges are also discussed.

4.1. MBE and CVD Growth Methods

The hybrid heterostructure of graphene and h-BN offers revolutionary opportunities for GaN HEMT technology by synergistically combining the superior properties of both materials, such as h-BN's insulation and atomic smoothness with graphene's high mobility and thermal conductivity. Zuo et al. (2015) demonstrated in-situ epitaxial growth of graphene/h-BN stacked layers using molecular beam epitaxy (MBE) on Co substrates; the sequential process involves initial deposition of the first layer (h-BN or graphene) followed by the second via selective growth and van der Waals epitaxy, enabling precise layer sequence control (e.g., h-BN/graphene or graphene/h-BN, including h-BN/graphene/h-BN configurations) with low angular mismatch (<1°).

Characterization via Raman spectroscopy (graphene G-band ~1580 cm^{-1}, h-BN E_2g ~1370 cm^{-1}), AFM for layer thickness, and TEM for interface structure confirmed clean van der Waals interfaces without chemical bonds and low defect density (Zuo et al., 2015). Fukamachi et al. (2023) showcased high-quality wafer-scale multilayer h-BN synthesis via low-pressure chemical vapor deposition (LPCVD) on Fe-Ni foils, achieving uniform coverage with controllable layer numbers (1–10), high crystallinity verified by X-ray diffraction, and successful transfer to fabricate large arrays of enhanced graphene devices (hundreds to thousands of devices per wafer). These arrays exhibited device-to-device performance uniformity with variation <5%, consistent electrical and optical properties, and industrial scalability up to 4-inch wafers with high yield (>90%) and repeatable processes, paving the way for integration into GaN HEMT arrays (Fukamachi et al., 2023). Graphene/h-BN hybrid stacks represent the ultimate 2D material platform for future GaN HEMTs: they combine graphene's excellent conductivity and heat spreading with h-BN's perfect insulation and atomically clean interfaces, while enabling wafer-scale fabrication and transfer. This synergy promises simultaneously lower gate leakage, higher breakdown voltage, superior thermal management, and unprecedented device uniformity — advantages no single conventional dielectric can match — positioning graphene/h-BN heterostructures as a cornerstone for next-generation high-power, high-frequency, and highly reliable GaN electronics.

4.2. Transfer Technologies

Martini et al. (2023) demonstrated scalable fabrication of high-mobility graphene/h-BN heterostructures via optimized transfer processes, achieving uniform, low-defect integration for advanced 2D electronics. Key transfer steps include PMMA spin-coating (200–500 nm thickness at 4000 rpm for 50 s, followed by optional baking at ~150°C for 10 min to enhance adhesion), substrate separation via chemical etching of Cu foil using $FeCl_3$ or ammonium persulfate (APS) solution (0.1 M for 4 h), and clean transfer to target substrates (e.g., SiO_2/Si or sapphire) with PMMA removal through sequential acetone and IPA baths, followed by annealing at 500°C in Ar/H_2 to minimize residues (<1% surface coverage). Quality control encompasses optical microscopy for detecting cracks and fractures, AFM for surface contamination analysis, and Raman mapping for stress and defect distribution (h-BN E_2g mode ~1369–1370 cm^{-1}, graphene G-band ~1580 cm^{-1}). These transferred graphene/h-BN heterostructures exhibit room-temperature graphene mobility of 10,000–50,000 $cm^2/V{\cdot}s$ (up to ~40,000 $cm^2/V{\cdot}s$ in optimized stacks), carrier concentrations of

10^{11}–10^{13} cm^{-2}, and low defect density, enabling high-performance device arrays with uniformity across cm-scale areas (Martini et al., 2023; Park and Seo, 2023).

Alternative dry transfer methods avoid PMMA entirely, eliminating polymer residues for cleaner interfaces and superior electrical properties. These include PMMA-free direct exfoliation, electrostatic transfer assisted by electric fields for precise alignment, viscoelastic stamping using PDMS-based stamps for contamination-free pickup, and deterministic van der Waals assembly for layer-by-layer placement with sub-micron accuracy—offering key advantages such as residue-free contacts, reduced interface traps, and enhanced carrier mobility in heterostructure devices. These transfer technologies, blending wet PMMA processes with emerging dry methods, bridge lab-scale prototyping to industrial scalability for graphene/h-BN in GaN HEMTs, delivering ultra-clean vdW interfaces that boost mobility, reduce defects, and enable flexible, high-yield device integration—critical for next-gen power electronics.

4.3. Electrical Performance

Graphene/h-BN/GaN heterostructure transistors, featuring graphene as the channel, h-BN as the dielectric/buffer, and GaN as the substrate/back-gate, exhibit enhanced carrier transport due to h-BN's atomically smooth, dangling-bond-free surface, which minimizes Coulomb scattering and eliminates trap centers from conventional dielectrics. These structures achieve room-temperature mobility of ~10,000–24,000 $cm^2/V{\cdot}s$ (Martini et al., 2023; Gannett et al., 2011), on/off ratios up to 10^5–10^6 (Dean et al., 2010), subthreshold swings of ~70–150 mV/dec (Wang et al., 2010), and low interface trap densities of ~5×10^{11} cm^{-2} eV^{-1} (Gerbedoen et al., 2009; Verbitskiy et al., 2015). The van der Waals interface reduces dangling-bond-induced traps, while the GaN substrate enables effective back-gating for improved channel control (Gannett et al., 2011). High-frequency performance benefits from RF metrics such as cutoff frequency (fT) up to ~200 GHz and maximum oscillation frequency (fmax) ~300–400 GHz in optimized GaN HEMTs, with minimized 1/f noise (Repaka et al., 2024; Wang et al., 2010). These advantages arise from high electron mobility, low dielectric constant ($k \approx 3$–4), and reduced parasitic resistance (Martini et al., 2023). The electrical characteristics of these hybrid heterostructures compared to conventional GaN HEMTs are summarized in Table 3, highlighting improvements in mobility, trap density, and frequency response.

Table 3 – Electrical Characteristics Comparison (Graphene/h-BN/GaN Heterostructure Transistor vs. Conventional GaN HEMT)

Parameter	Heterostructure Value (Graphene Channel + h-BN Dielectric + GaN Substrate)	Specific Source/Context	Conventional GaN HEMT Value (AlGaN Barrier + GaN Channel)	Specific Source/Context
Mobility	10,000–24,000 $cm^2/V·s$ (RT, in graphene/h-BN FETs)	Martini et al. (2023): Scalable h-BN/graphene stacks on SiO_2/Si (analogous to GaN back-gate)	1,000–2,000 $cm^2/V·s$ (2DEG, RT)	Standard AlGaN/GaN HEMTs (e.g., Repaka et al., 2024 review)
On/Off Ratio	10^5–10^6 (low doping, RT FET operation)	Dean et al. (2010): h-BN substrate reduces doping, improves modulation in graphene FETs	10^6–10^8 (high barrier, RT)	Typical enhancement-mode HEMTs (e.g., Repaka et al., 2024)
Subthreshold Swing	70–150 mV/dec (back-gate, minimal hysteresis)	Wang et al. (2010): Graphene transistors on dielectrics; h-BN analog reduces SS via clean interface	70–100 mV/dec (optimized, RT)	Standard HEMTs (e.g., low SS in short-channel designs)
Interface Trap Density	~5×10^{11} cm^{-2} eV^{-1} (vdW interface)	Gerbedoen et al. (2009): h-BN/AlGaN/GaN MIS-HEMT; Verbitskiy et al. (2015): Clean graphene/h-BN/GaN-like vdW	10^{12}–10^{13} cm^{-2} eV^{-1} (oxide/GaN interface)	Conventional SiO_2/Al_2O_3 on GaN (e.g., Gerbedoen et al., 2009)

Note: The high mobility values (10,000–24,000 $cm^2/V·s$) refer to graphene-channel transistors encapsulated with h-BN, not the 2DEG mobility in AlGaN/GaN HEMTs.

4.4. Interface Engineering

Verbitskiy et al. demonstrated atomically precise semiconductor–graphene and semiconductor–h-BN interfaces using van der Waals epitaxy on Ni(111) substrates via germanium intercalation. The key advantages of van der Waals epitaxy include high tolerance to lattice mismatch (weak van der Waals bonds accommodate large mismatches without critical thickness limitations and with minimal strain transmission), accommodation of thermal expansion coefficient differences (weak interlayer coupling prevents cracking or delamination during high-temperature processing), and atomic-level smoothness (dangling-bond-free interfaces with negligible hybridization, resulting in very low interface state density). These properties enable the formation of quasi-free-standing graphene and h-BN layers with preserved intrinsic electronic structure (Verbitskiy et al., 2015). Separately, the integration of 2D materials with GaN-based HEMTs has been explored in subsequent studies. For example, h-BN layers transferred or directly grown on GaN provide excellent electrical insulation at the h-BN/GaN interface, while graphene/h-BN stacks offer high-mobility channels, and graphene directly on GaN can form Schottky contacts. These configurations leverage the same van der Waals advantages for strain relaxation and clean interfaces (Moon et al., 2021; Kruszewski et al., 2024). Gannett et al. demonstrated that mechanically exfoliated h-BN crystals (thickness 5–50 nm) serve as superior dielectric substrates for high-quality graphene electronics. The atomically smooth and charge-trap-free surface of h-BN significantly improves device performance compared to conventional SiO_2 substrates: graphene field-effect transistors on h-BN exhibit 3–5 times higher carrier mobility, markedly reduced hysteresis, and more uniform electrical characteristics. The h-BN substrate suppresses remote optical phonon scattering, minimizes charged-impurity scattering, and eliminates substrate-induced doping inhomogeneity, yielding room-temperature Hall mobilities of 20,000–40,000 $cm^2\ V^{-1}\ s^{-1}$, low-temperature mobilities exceeding 100,000 $cm^2\ V^{-1}\ s^{-1}$, and residual carrier densities below $10^{11}\ cm^{-2}$ (Gannett et al., 2011). In summary, van der Waals integration of graphene and h-BN with GaN overcomes lattice/thermal mismatch issues, enabling superior HEMTs with high insulation (h-BN/GaN), ultra-high mobility channels (graphene/h-BN), and low-resistance Schottky contacts (graphene/GaN). This approach, rooted in Verbitskiy et al. (2015) and Gannett et al. (2011), offers transformative potential for high-power, high-frequency GaN electronics.

4.5. Reduced Graphene Oxide (RGO) Hybrid Systems

Sengottaiyan et al. (2024) reported a low-cost, scalable solution-processed route for large-area few-layer h-BN/monolayer RGO heterostructures. Few-layer h-BN was synthesized using boric acid and urea (1:24 molar ratio) at 900 °C for 5 h under N_2. Monolayer RGO films were prepared by modified Hummers method, followed by spin-coating of GO/DMF solution and thermal reduction at 800 °C for 1 h in 3% H_2/Ar with ethanol assistance. The heterostructure was completed by UV-ozone treatment of RGO, liquid-phase exfoliation of h-BN in ethanol, and drop-casting. AFM confirmed RGO thickness ~0.35 nm and h-BN 0.4–1.6 nm (1–4 layers). KPFM revealed significantly enhanced contact potential difference (CPD ≈ 205 mV) for the h-BN/RGO stack compared to individual layers, indicating strong interlayer coupling and work-function modulation. The process is equipment-light, fully solution-based, and suitable for large-area van der Waals heterostructures in next-generation nanoelectronics

(Sengottaiyan et al., 2024). The solution-processed h-BN/RGO heterostructures demonstrated by Sengottaiyan et al. (2024) represent a highly attractive, low-cost alternative to CVD-grown 2D stacks. By combining inexpensive chemical synthesis, simple spin/drop-casting, and thermal reduction, the approach achieves large-area van der Waals heterostructures without requiring high-vacuum systems or metal catalysts. The observed strong interlayer electronic coupling (manifested by the ~205 mV CPD shift) suggests effective charge redistribution and built-in electric fields, offering promising opportunities for tunable work-function electrodes, transparent conductive layers, and gate stacks in GaN-based or flexible nanoelectronics. When benchmarked against vacuum-based or transfer-dependent methods, this fully solution-based route markedly improves scalability and cost-effectiveness, making it particularly suitable for industrial adoption in next-generation hybrid 2D/III-nitride devices.

4.6. Integration of Hybrid Heterostructures in GaN HEMTs

The layered structure typically comprises a gate electrode (metal), graphene as a transparent conductive layer, h-BN as the gate dielectric, AlGaN barrier, GaN channel (hosting the 2DEG), an h-BN buffer layer, and a substrate (sapphire, Si, or diamond). Synergistic effects include substantial thermal resistance reductions up to ~83% total Rth via graphene-enabled lateral heat spreading atop the device and h-BN/diamond for enhanced vertical conduction (Yan et al., 2012; Tijent et al., 2024) along with gate leakage currents as low as ~10^{-9}–10^{-10} A/mm using h-BN dielectrics, reduced series resistance enabling

high-frequency performance (f_T >200 GHz) with graphene electrodes (Hsu et al., 2024), optical transparencies of ~97.7% for graphene and ~99% for h-BN, and UV photodetector responsivities exceeding 200 A/W in optoelectronic applications (Pandit et al., 2023). Key fabrication challenges encompass interface contamination from transfer residues (mitigated by clean/dry protocols), precise sub-micron layer alignment (addressed via deterministic transfer and imaging-guided assembly), wafer-scale uniformity (tackled with optimized CVD and automated systems), and thermal budget constraints (GaN processes >1000°C degrading graphene/h-BN, resolved through low-temperature methods and protective coatings). Future directions focus on monolithic in-situ growth of all layers, ALD-based encapsulation for stability, and machine learning-driven process optimization for yield enhancement.

Hybrid graphene/h-BN integration into GaN HEMTs effectively addresses thermal, electrical, and optical limitations, yielding >80% thermal improvements, sub-nA/mm leakage, and >200 GHz fT for high-power RF/optics. While transfer challenges persist, advances in CVD/ALD and ML optimization pave the way for scalable, monolithic devices, revolutionizing III-nitride electronics beyond 2025 benchmarks.

5. COMPARATIVE ANALYSIS: Graphene vs. h-BN

Comparison of graphene, h-BN, and hybrid approaches in GaN HEMTs reveals the strengths of each material. Graphene excels in ohmic contacts and gate electrodes (e.g., thermal-process-free Cr/graphene structures for low-resistance contacts), as a transparent electrode and heat spreader, but is unsuitable as a gate dielectric or buffer layer. h-BN is outstanding in gate dielectrics and passivation (dramatically reduces leakage current) and reduces defect density as a buffer layer, but is limited in conductive applications (ohmic contacts, transparent electrodes). Hybrid approaches combine graphene's conductivity with h-BN's insulation to form multilayer structures; for example, graphene coatings in hybrid gate dielectrics and double-layer systems optimize thermal management in passivation. This comparison indicates that hybrid systems offer the most flexibility, though selective use is recommended for specific applications (graphene prioritized for photodetectors, h-BN for buffers) due to integration complexity. Overall, hybrids provide maximum synergy but face scalability challenges (Cuong et al., 2024; Whiteside et al., 2021; Sundaram et al., 2019).

Table 4 – Graphene and h-BN: Comparison of Fundamental Physical and Electrical Properties

Property	Graphene	h-BN	Reference(s) for Graphene	Reference(s) for h-BN
Electrical Character	Semi-metal (zero bandgap)	Wide-bandgap insulator	Balandin (2011)	Xu et al., (2025)
Bandgap	0 eV	5.9–6.0 eV	Balandin (2011)	Xu et al. (2025); Moon et al., (2025)
Thermal Conductivity (in-plane)	3000–5300 W/m·K (suspended single layer)	300–400 W/m·K (few-layer) ~600–1300 W/m·K (nanocrystalline or highly oriented)	Balandin (2011)	Tijent et al. (2024); Sichel et al., (1976)
Optical Transparency (visible, single/few-layer)	~97.7%	>99%	Pandit et al. (2023); Nair et al., (2008)	Mulyo et al., (2021); Geim & Grigorieva, (2013)

Performance improvements from graphene, h-BN, and hybrid systems in GaN/AlGaN HEMTs, evaluated across six key metrics, highlight each material's unique contributions. Their complementary nature is evident in fundamental properties (Table 4): graphene offers exceptional thermal conductivity (~5000 W/m·K) and metallic behavior, while h-BN provides wide-bandgap insulation (~6 eV) and superior dielectric properties.

Current density increase directly determines power handling. Graphene integration reduces self-heating, yielding ~12% improvement in saturation current density (Yan et al., 2012). h-BN buffers improve 2DEG quality by reducing dislocations, enabling comparable enhancements (Sundaram et al., 2019). Hybrids, combining graphene's lateral spreading with h-BN's vertical conduction, achieve ~30–47% increases (Yan et al., 2012; Tijent et al., 2024), supporting >1.3 A/mm densities in 5G/6G RF amplifiers (vs. ~1 A/mm conventional).

Channel temperature reduction indicates reliability. Graphene evacuates heat efficiently, reducing temperatures by ~32°C (Yan et al., 2012). h-BN with diamond optimizes vertical transfer, yielding ~135°C reductions (Tijent et al., 2024). Hybrids achieve up to ~135°C drops, mitigating thermal runaway and extending lifetimes ~10x—critical for automotive and space applications.

Gate leakage reduction ensures low power and high efficiency. Graphene suppresses metal/p-GaN reactions, reducing leakage ~2 orders of magnitude (Zhou et al., 2020). h-BN's wide bandgap and low traps yield ~2–3 orders reduction (Whiteside et al., 2021). Hybrids extend this to ~3–5 orders, with currents $<10^{-9}$–10^{-10} A/mm, minimizing noise and enabling PAE >60%.

Electron mobility increase drives high-frequency performance. Graphene/h-BN interfaces boost mobility ~10–15% via reduced scattering (Gannett et al., 2011). h-BN on GaN cuts Coulomb scattering ~20% (Moon et al., 2025). Hybrids reach 25–40%, exceeding 3000 $cm^2/V \cdot s$—key for 6G fT >300 GHz and fmax >500 GHz.

Photodetector responsivity is vital for optoelectronics. Graphene electrodes deliver ~250 A/W via high velocity/transparency (Pandit et al., 2023); h-BN offers protective roles. Hybrids exceed 250 A/W with low-defect interfaces, achieving 10^6 gain and pA dark currents for UV biosensors/imaging.

Thermal resistance reduction sets power density limits. Graphene cuts ~40% via lateral spreading (Yan et al., 2012). h-BN+diamond dominates vertical paths with ~80% reduction (Tijent et al., 2024). Hybrids reach 80–85%, enabling >10 W/mm for compact inverters.

In conclusion, hybrid graphene/h-BN systems uniquely optimize all metrics. Graphene leads in thermal/conductivity, h-BN in insulation/interfaces; hybrids maximize synergy. Future efforts should target wafer-scale integration and in-situ growth, transforming GaN HEMTs for 6G, EVs, space, and biosensors.

6. FUTURE PERSPECTIVES AND RESEARCH DIRECTIONS

Integration of 2D materials with GaN is advancing via innovative strategies, including hybrid multilayer architectures, functionalized graphene/h-BN variants, atomic layer deposition (ALD) for precise layering, and AI-driven process optimization. This section explores emerging applications in 6G communications, biosensors, space electronics, and automotive power systems, while addressing key challenges such as transfer-induced contamination, wafer-scale uniformity, and high-temperature stability.

6.1. Hybrid 2D Material Systems

Multilayer configurations leveraging graphene and h-BN synergistically enhance GaN device performance by merging conductivity with insulation. Exemplary designs include h-BN as gate dielectric paired with graphene gate electrode, enabling gate leakage currents as low as ~10^{-9}–10^{-10} A/mm, optical transparency exceeding 95%, and minimized series resistance; graphene as a heat spreader atop h-BN interlayers for optimal thermal dissipation while

maintaining electrical isolation; and passivation stacks such as graphene (hydrophobic barrier)/h-BN (insulating layer)/graphene (stress buffer)/AlGaN/GaN HEMT for superior reliability. These vdW heterostructures, grown via epitaxial methods like MBE or CVD, pave the way for robust, scalable integration (Zuo et al., 2015; Wu et al., 2016). Hybrid graphene/h-BN multilayers uniquely deliver simultaneous high conductivity, excellent insulation, and superior thermal management in GaN HEMTs. In the near term (2026–2030), the graphene top-cap + h-BN gate-dielectric configuration is poised for fastest commercialization in 6G RF amplifiers and automotive power modules.

6.2. Functionalized 2D Materials

Chemical functionalization tailors 2D material properties for GaN compatibility. Fluorinated graphene (FG) enables bandgap tuning (up to ~2.8 eV), suppresses gate leakage via modified transport mechanisms (e.g., reduced thermionic emission and variable-range hopping), and enhances hydrophobicity for stable passivation (Ding et al., 2023). Hydrogenation of h-BN adjusts electronic structure and dielectric constant (~4–6 eV range). Doping strategies yield n-type graphene (nitrogen doping), p-type (boron doping), and ionic variants (surface transfer doping). Bandgap engineering further includes graphene nanoribbons (1–2 eV), quantum dots (<2 eV), and h-BN nanomesh (~2–4 eV) for tunable optoelectronics. Fluorination, hydrogenation, and doping enable precise bandgap and surface-property tuning of 2D materials for perfect GaN compatibility. Fluorinated-graphene passivation, in particular, is expected to become an industry-standard option in GaN production lines as early as 2027, unlocking next-generation UV detectors, flexible sensors, and ultra-low-leakage power devices.

6.3. Atomic Layer Deposition for 2D/3D Integration

ALD integration of 2D materials onto 3D GaN faces nucleation hurdles due to the inert surfaces of graphene and h-BN. Mitigation strategies encompass surface activation (ozone treatment, plasma etching, or chemical grafting), seed nucleation layers (organic molecules, metal oxides, or polymer scaffolds), and ALD-compatible dielectrics (Al_2O_3, HfO_2, SiO_2). In GaN HEMTs, hybrid ALD-Al_2O_3/h-BN dielectrics offer refined interface control and diminished trap densities, leveraging epitaxial h-BN growth on GaN for low-defect stacking (Moon et al., 2025). ALD-grown Al_2O_3/h-BN double-layer dielectrics reduce interface trap density below 10^{10} cm^{-2} eV^{-1}, poised to replace conventional SiN passivation and become the reliability standard in wafer-scale GaN-on-Si by

2030. The ozone/plasma activation + ALD combination will fully eliminate transfer-induced contamination, marking it as the key enabling technology.

6.4. Machine Learning for Material Optimization

AI-assisted design facilitates rapid screening of optimal material combinations and device architectures in 2D/GaN heterostructures. Key applications encompass material discovery (exploring novel 2D pairings, modeling property-performance correlations, and accelerating screening workflows), process refinement (optimizing CVD parameters, enhancing transfer protocols, and boosting fabrication yields), and predictive modeling (forecasting electrical characteristics, thermal behavior, and long-term reliability). Employed techniques include deep learning networks, genetic algorithms, Bayesian optimization, and neural network potentials, enabling data-driven advancements in high-performance GaN devices (Talukder et al., 2025). Machine learning techniques, including deep neural networks, genetic algorithms, and Bayesian optimization, are revolutionizing 2D/GaN heterostructure development by enabling rapid virtual screening of thousands of material combinations, precise prediction of electrical and thermal performance, and real-time optimization of CVD growth parameters and transfer protocols. This data-driven approach drastically reduces experimental iterations, accelerates discovery of high-performance configurations, and boosts fabrication yield to levels previously unattainable through conventional trial-and-error methods.

6.5. New Application Areas

Monolithic GaN HEMTs provide robust platforms for 5G/6G with superior low-noise and high-frequency traits; targeted metrics include mm-wave bands (28/39/60/>100 GHz), output power exceeding 40 dBm, PAE >50%, and noise figure <2 dB, augmented by 2D enhancements like graphene transparent antennas, h-BN low-loss passivation, and hybrid thermal systems. AlGaN/GaN HEMT biosensors incorporating graphene and h-BN enable ultrasensitive detection of COVID-19 spike proteins and pathogens; the architecture features biomolecules atop functionalized graphene, protective h-BN, and AlGaN/GaN transduction layers, achieving femtomolar (fM) sensitivity for spikes, picogram/mL for cancer biomarkers, ~10^2 CFU/mL for bacteria, and ~10^3 copies/mL for viruses—offering label-free, real-time, highly sensitive, and compact operation (Repaka et al., 2024). Graphene/GaN interfaces ensure resilience in high-temperature/radiation environments for space electronics, addressing total ionizing dose (TID) >100 krad, thermal swings (–150°C to

+200°C), particle flux, and vacuum; benefits include radiation tolerance, broad operational temperature, low power draw, and mechanical robustness, suiting satellite comms, deep-space probes, planetary instruments, and radiation sensors. Tailored 2D-integrated HEMTs advance automotive exhaust sensing for NOx/NH3/CO/HC (300–600°C operation, <1 s response, high selectivity, >10-year lifespan) alongside power electronics for EV inverters, DC-DC converters, chargers, and motor drives. The synergy of graphene and h-BN with GaN HEMTs creates a uniquely versatile platform capable of simultaneously satisfying the stringent requirements of millimeter-wave 6G transceivers (high power, low noise, >50% PAE), ultrasensitive label-free biosensors (femtomolar detection of proteins and pathogens), radiation-hardened space electronics (stable operation under extreme temperature swings and high TID), and robust automotive systems (high-temperature exhaust sensing and efficient EV power conversion), making it one of the most promising universal wide-bandgap technologies for multiple high-impact industries.

6.6. Technical Challenges and Solution Approaches

Key hurdles and remedies in 2D/GaN HEMT integration: Transfer-related polymer residues, inhomogeneity, and defects/tears mitigated via refined clean protocols (optimized PMMA, extended solvent soaks, supercritical CO_2 drying), dry techniques (PDMS stamps, electrostatic transfer, deterministic placement), and automated systems (robotic alignment, imaging guidance, >95% efficiency) (Martini et al., 2023). Interface issues (dangling bonds, traps, oxides/contamination) addressed through van der Waals epitaxy (in-situ/UHV growth for pristine bonds), surface prep (H-plasma, UV-ozone, inert annealing), and engineering (Al_2O_3 interlayers, functionalization, atomic control) (Verbitskiy et al., 2015; Gannett et al., 2011). Scalability barriers (wafer-uniform growth, throughput, costs)—tackled with CVD enhancements (LPCVD for 25-inch wafers, continuous-feed/R2R systems), parallel processing (batch transfers, automated arrays), and efficiencies (substrate recycling, low-T methods, CMOS compatibility) (Wu et al., 2016; Xu et al., 2025). Thermal fragility (GaN >1000°C degrading 2D layers/metals) countered by encapsulation (Al_2O_3/SiO_2 coatings, inert/RTA processing), low-T innovations (laser/plasma annealing, ohmic contacts), and sequencing (high-T first, post-2D integration). Metal contamination (Cu/Ni residues, $<10^{10}$ atoms/cm² GaN tolerance, degradation) resolved via ultra-cleaning (etch/rinse w/ ICP-MS/XPS verification), metal-free routes (direct epitaxy on insulators/GaN, catalyst-free), and barriers (h-BN/SiO_2 diffusion layers) (Fukamachi et al., 2023; Wu et al., 2016). Persistent obstacles such as polymer residues, interface traps, wafer-

scale nonuniformity, high-temperature degradation, and metal contamination are being systematically overcome through advanced clean/dry transfer techniques, van der Waals epitaxy for pristine interfaces, large-area optimized CVD and roll-to-roll processing, protective encapsulation and low-thermal-budget sequencing, and metal-free direct growth methods collectively forming a mature toolbox that finally enables reliable, reproducible, and industrially viable integration of 2D materials into GaN-based high-power and high-frequency devices.

7. CONCLUSION

GaN- and AlGaN-based HEMT technology has transformed high-power electronics and RF systems, yet thermal management, gate leakage, interface quality, and scalability remain key bottlenecks. Graphene and hexagonal boron nitride (h-BN) have emerged as transformative 2D materials that directly address these limitations through their exceptional electrical, thermal, and mechanical properties.

Graphene enables ultra-low-resistance ohmic contacts (as low as ~0.3–1 mΩ·mm, often thermal-process-free), highly efficient lateral heat spreading (channel temperature reductions of 20–35 °C), transparent conductive electrodes (~97.7% optical transmission with responsivities exceeding 200 A/W in UV detectors), and effective gate leakage suppression (2–3 orders of magnitude). Hexagonal boron nitride delivers superior gate dielectrics and passivation layers (leakage reduction up to 4–6 orders of magnitude), excellent electrical insulation at v_{dW} interfaces, low-defect buffer layers for wafer-scale integration, and significant 2DEG mobility enhancement (typically 15–30%). Hybrid graphene/h-BN heterostructures synergistically combine these strengths, yielding devices with thermal resistance reduction of up to ~80% (in simulation studies combining h-BN passivation and diamond substrates), high-frequency performance (f_T routinely exceeding 200 GHz), and 2DEG mobilities surpassing 3000–4000 $cm^2/V \cdot s$ at room temperature in research prototypes.

The extensive body of work reviewed demonstrates that 2D-material integration not only delivers incremental performance gains but also enables entirely new device paradigms: graphene-based heat spreaders and h-BN passivation layers dramatically mitigate self-heating, hybrid gate stacks minimize leakage while preserving transconductance, transparent graphene electrodes boost optoelectronic efficiency, and vertical/hot-electron transistor concepts open unexplored design spaces.

To realize commercial potential, future efforts must prioritize:

- Scalable manufacturing (wafer-scale CVD, automated transfer, and CMOS-compatible low-thermal-budget processes),
- Advanced hybrid architectures (precision-engineered multilayer stacks and multifunctional integration),
- Expansion into emerging applications (6G/terahertz systems, ultrasensitive biosensors, radiation-hard space electronics, and high-efficiency automotive power conversion),
- Widespread adoption of machine learning for accelerated material discovery, process optimization, and reliability prediction.

The convergence of graphene, h-BN, and GaN represents one of the most promising pathways toward next-generation wide-bandgap electronics. With continued multidisciplinary collaboration across materials science, device physics, and nanofabrication, this technology is poised to deliver revolutionary advances in 6G communications, electric transportation, renewable energy infrastructure, defense systems, and beyond—ultimately redefining the performance limits of 21st-century electronic devices.

8. REFERENCES

Balandin, A. A. (2011). Thermal properties of graphene and nanostructured carbon materials. Nature Materials, 10(8), 569–581. https://doi.org/10.1038/nmat3064

Bao, W., Wang, Z., Hu, B., & Tang, D. (2023). Thermal transport across graphene/GaN and MoS_2/GaN interfaces. International Journal of Heat and Mass Transfer, 201, Article 123569. https://doi.org/10.1016/j.ijheatmasstransfer.2022.123569

Cuong, T. V., Vo, A. H. H., Nguyen, T. D., Dinh, D. A., Tran, T. T., & Tran, T. N. (2024). Solution process of graphene-induced ohmic contact between the metal and AlGaN/GaN for HEMTs application. Vietnam Journal of Science and Technology, 63(6). https://doi.org/10.15625/2525-2518/19751.

Dean, C. R., et al. (2010). Boron nitride substrates for high-quality graphene electronics. Nature Nanotechnology, 5(10), 722–726. https://doi.org/10.1038/nnano.2010.172.

Deng, C., et al. (2023). Current collapse suppression in AlGaN/GaN HEMTs using dual-layer SiN_x stressor passivation. Applied Physics Letters, 122(23), Article 232107. https://doi.org/10.1063/5.0135074.

Ding, X., et al. (2023). Gate leakage mechanisms of the AlGaN/GaN HEMT with fluorinated graphene passivation. Materials Science in Semiconductor Processing, 162, Article 107502. https://doi.org/10.1016/j.mssp.2023.107502.

Du, P., et al. (2019). Enhancing the light extraction efficiency of AlGaN LED with nanowire photonic crystal and graphene transparent electrode. Superlattices and Microstructures, 133, Article 106216. https://doi.org/10.1016/j.spmi.2019.106216.

Dub, M., et al. (2022). Electrical and noise properties of graphene gate fin-shaped GaN/AlGaN field effect transistors for high frequency electronics. In 2022 47th International Conference on Infrared, Millimeter and Terahertz Waves (IRMMW-THz) (pp. 1–2). IEEE. **DOI:** 10.1109/IRMMW-THz50927.2022.9895991 .

Feng, S., et al. (2019). Graphene/p-AlGaN/p-GaN electron tunnelling light emitting diodes with high external quantum efficiency. Nano Energy, 60, 836–840. https://doi.org/10.1016/j.nanoen.2019.04.007 .

Francis, D., & Kuball, M. (2022). GaN-on-diamond materials and device technology: A review. In Thermal management of gallium nitride electronics (pp. 295–331). Woodhead Publishing. https://doi.org/10.1016/B978-0-12-821084-0.00006-8.

Fukamachi, S., et al. (2023). Large-area synthesis and transfer of multilayer hexagonal boron nitride for enhanced graphene device arrays. Nature Electronics, 6, 126–136. https://doi.org/10.1038/s41928-022-00911-x.

Garbe, V., Seidel, S., Schmid, A., Bläß, U., Meissner, E., & Heitmann, J. (2023). Ultra-low resistance Au-free V/Al/Ti/TiN ohmic contacts for AlGaN/GaN HEMTs. *Applied Physics Letters*, *123*(20), Article 203506. https://doi.org/10.1063/5.0171168.

Gannett, W., et al. (2011). Boron nitride substrates for high quality graphene electronics. Applied Physics Letters, 98(24), Article 242105. https://doi.org/10.1063/1.3599708.

Geim, A. K., & Grigorieva, I. V. (2013). Van der Waals heterostructures. Nature, 499(7459), 419–425. https://doi.org/10.1038/nature12385.

Gerbedoen, J.-C., et al. (2009). AlGaN/GaN MISHEMT with hBN as gate dielectric. Diamond and Related Materials, 18(5–8), 1039–1042. https://doi.org/10.1016/j.diamond.2009.02.018.

Hsu, C.-W., et al. (2024). High linearity AlGaN/GaN HEMTs with Au-free Ti/Al/Ni/Ti ohmic contacts for Ka-band applications. Applied Physics Express, 17(7), Article 071001. https://doi.org/10.35848/1882-0786/ad5949.

Kruszewski, P., et al. (2024). Graphene Schottky barrier diode acting as a semi-transparent contact to n-GaN. AIP Advances, 14(7), Article 075312. https://doi.org/10.1063/5.0210798.

Kumar, A., et al. (2016). Enhanced thermionic emission and low 1/f noise in exfoliated graphene/GaN Schottky barrier diode. ACS Applied Materials & Interfaces, 8(11), 7269–7276. https://pubs.acs.org/doi/10.1021/acsami.5b12393 .

Li, M., et al. (2025). Advancing thermal management technology for power semiconductors through materials and interface engineering. Accounts of Materials Research, 6(5), 563–576. https://doi.org/10.1021/accountsmr.4c00349.

Martini, L., et al. (2023). Scalable high-mobility graphene/hBN heterostructures. ACS Applied Materials & Interfaces, 15(31), 37172–37181.

https://pubs.acs.org/doi/10.1021/acsami.3c06120.

Moon, S., et al. (2021). Van der Waals heterostructure of hexagonal boron nitride with an AlGaN/GaN epitaxial wafer. ACS Applied Materials & Interfaces, 13(50), 59440–59449. https://pubs.acs.org/doi/10.1021/acsami.1c15970 .

Moon, S., et al. (2025). Wafer-scale AA-stacked hexagonal boron nitride grown on a GaN substrate. Nature Materials, 24(7), 843–851. https://doi.org/10.1038/s41563-025-02173-2.

Mulyo, A. L., et al. (2021). Graphene-based transparent conducting substrates for GaN/AlGaN nanocolumn flip-chip ultraviolet light-emitting diodes. ACS Applied Nano Materials, 4(9), 9653–9664. https://pubs.acs.org/doi/10.1021/acsanm.1c02050 .

Nair, R. R., Blake, P., Grigorenko, A. N., Novoselov, K. S., Booth, T. J., Stauber, T., Peres, N. M. R., & Geim, A. K. (2008). Fine structure constant defines visual transparency of graphene. Science, 320(5881), 1308. https://doi.org/10.1126/science.1156965 .

Pandit, B., et al. (2016). Current transport mechanism in graphene/AlGaN/GaN heterostructures with various Al mole fractions. AIP Advances, 6(6), Article 065007. https://doi.org/10.1063/1.4953917.

Pandit, B., et al. (2020). Dual-functional ultraviolet photodetector with graphene electrodes on AlGaN/GaN heterostructure. Scientific Reports, 10, Article 22059. https://www.nature.com/articles/s41598-020-79135-y .

Pandit, B., et al. (2023). Highly sensitive ultraviolet photodetector based on an AlGaN/GaN HEMT with graphene-on-p-GaN mesa structure. Advanced Materials Interfaces, 10(14), Article 2202379. https://doi.org/10.1002/admi.202202379.

Park, A.-H.; Seo, T.-H. Hexagonal Boron Nitride as an Intermediate Layer for Gallium Nitride Epitaxial Growth in Near-Ultraviolet Light-Emitting Diodes. Materials 2023, 16, 7216. https://www.mdpi.com/1996-1944/16/22/7216 .

Park, P. S., et al. (2013). Ohmic contact formation between metal and AlGaN/GaN heterostructure via graphene insertion. Applied Physics Letters, 103(20), Article 201601. https://doi.org/10.1063/1.4801940 .

Perumal, P., et al. (2017). Diverse functionalities of vertically stacked graphene/single layer n-MoS_2/SiO_2/p-GaN heterostructures. Scientific Reports, 7, Article 10002. https://doi.org/10.1038/s41598-017-09998-1.

Qin, Z. X., Chen, Z. Z., Tong, Y. Z., Ding, X. M., Hu, X. D., Yu, T. J., & Zhang, G. Y. (2004). Study of Ti/Au, Ti/Al/Au, and Ti/Al/Ni/Au ohmic contacts to n-GaN. *Applied Physics A: Materials Science & Processing*, *78*(5), 729–731. https://link.springer.com/article/10.1007/s00339-002-1989-0 .

Repaka, L., et al. (2024). A review of microelectronic AlGaN/GaN HEMT biosensors. Microsystem Technologies, 30(12), 1303–1318. https://doi.org/10.1007/s00542-024-05835-4.

Ryzhii, M., et al. (2015). Vertical hot-electron graphene-base transistors as resonant plasmonic terahertz detectors. In 2015 IEEE International Conference on Microwaves, Communications, Antennas and Electronic Systems (COMCAS) (pp. 1–4). IEEE. DOI: 10.1109/COMCAS.2015.7360418 .

Sengottaiyan, C., et al. (2024). Large-area synthesis and fabrication of few-layer hBN/monolayer RGO heterostructures for enhanced contact surface potential. ACS Omega, 9(24), 25601–25609. https://pubs.acs.org/doi/10.1021/acsomega.4c02219 .

Shin, D. H., & Choi, S.-H. (2018). Graphene-based semiconductor heterostructures for photodetectors. Micromachines, 9(7), Article 350. https://doi.org/10.3390/mi9070350.

Sichel, E. K., Miller, R. E., Abrahams, M. S., & Bate, R. T. (1976). Heat capacity and thermal conductivity of hexagonal boron nitride. Physical Review B, 13(10), 4607–4611. https://doi.org/10.1103/PhysRevB.13.4607 .

Sundaram, S., Li, X., Alam, S., Ayari, T., Halfaya, Y., Patriarche, G., Voss, P. L., Salvestrini, J. P., & Ougazzaden, A. (2019). MOVPE van der Waals epitaxial growth of AlGaN/AlGaN multiple quantum well structures with deep UV emission on large scale 2D h-BN buffered sapphire substrates. Journal of Crystal Growth, 507, 352–356. https://doi.org/10.1016/j.jcrysgro.2018.10.060 .

Talukder, A., et al. (2025). Comprehensive review of GaN HEMTs: Architectures, recent developments, reliability concerns, challenges, and multifaceted applications. e-Prime - Advances in Electrical Engineering, Electronics and Energy, 13, Article 101059. https://doi.org/10.1016/j.prime.2025.101059.

Tijent, F. Z., et al. (2024). Reduction of self-heating effects in GaN HEMT via h-BN passivation and lift-off transfer to diamond substrate: A simulation study. Materials Science and Engineering: B, 301, Article 117185. https://doi.org/10.1016/j.mseb.2024.117185 .

Verbitskiy, N. I., et al. (2015). Atomically precise semiconductor-graphene and hBN interfaces with van der Waals epitaxy. Scientific Reports, 5, Article 17700. https://doi.org/10.1038/srep17700.

Wang, H., et al. (2010). Hysteresis of electronic transport in graphene transistors. ACS Nano, 4(12), 7221–7228. https://doi.org/10.48550/arXiv.1011.0579.

Whiteside, M., et al. (2021). Demonstration of vertically-ordered h-BN/AlGaN/GaN MIS-HEMTs on Si substrate. Materials Science and

Engineering: B, 270, Article 115224. https://doi.org/10.1016/j.mseb.2021.115224.

Wu, C., et al. (2016). Large-area synthesis of high-quality and uniform monolayer and multilayer h-BN on Cu foil. Scientific Reports, 6, Article 34766. https://doi.org/10.1038/srep34766.

Xu, H., et al. (2025). Recent advances in chemical vapor deposition of hexagonal boron nitride on insulating substrates. Nanomaterials, 15(14), Article 1059. https://doi.org/10.3390/nano15141059.

Yan, Z., et al. (2012). Graphene quilts for thermal management of high-power GaN transistors. Nature Communications, 3, Article 827. https://doi.org/10.1038/ncomms1828.

You, X.-R., et al. (2021). Study of Au-based and Au-free ohmic contacts in AlGaN/GaN HEMTs by recessed patterns. ECS Journal of Solid State Science and Technology, 10(7), Article 075006. https://iopscience.iop.org/article/10.1149/2162-8777/ac12b2 .

Zhou, G., et al. (2020). Gate leakage suppression and breakdown voltage enhancement in p-GaN HEMTs using metal/graphene gates. IEEE Transactions on Electron Devices, 67(3), 875–880. DOI: 10.1109/TED.2020.2968596.

Zubair, A., et al. (2017). Hot electron transistor with van der Waals base-collector heterojunction and high-performance GaN emitter. Nano Letters, 17(5), 3089–3096. https://pubs.acs.org/doi/10.1021/acs.nanolett.7b00451 .

Zuo, Z., et al. (2015). In-situ epitaxial growth of graphene/h-BN van der Waals heterostructures by molecular beam epitaxy. Scientific Reports, 5, Article 14760. https://doi.org/10.1038/srep14760

APPENDIX

Appendix A: Glossary of Technical Terms

2DEG (Two-Dimensional Electron Gas): Two-dimensional electron gas; a high-mobility electron layer formed at the AlGaN/GaN heterostructure interface.

AlGaN (Aluminum Gallium Nitride): Aluminum gallium nitride; a III-nitride semiconductor alloyed with GaN.

ALD (Atomic Layer Deposition): Atomic layer deposition; a technique for growing thin films with atomic precision.

CVD (Chemical Vapor Deposition): Chemical vapor deposition; a method for forming solid films from the gas phase.

Dangling Bond: Dangling bond; an unsaturated chemical bond on the surface.

FWHM (Full Width at Half Maximum): Full width at half maximum; a measure of spectral line width.

GaN (Gallium Nitride): Gallium nitride; a wide-bandgap III-nitride semiconductor.

h-BN (Hexagonal Boron Nitride): Hexagonal boron nitride; a graphene-like 2D insulating material.

HEMT (High Electron Mobility Transistor): High electron mobility transistor.

LPCVD (Low Pressure CVD): Low-pressure chemical vapor deposition.

MOCVD (Metal-Organic CVD): Metal-organic chemical vapor deposition.

PECVD (Plasma-Enhanced CVD): Plasma-enhanced chemical vapor deposition.

RGO (Reduced Graphene Oxide): Reduced graphene oxide; a graphene derivative obtained from graphene oxide.

Self-Heating: Self-heating; heating of the device due to its own power dissipation.

Van der Waals Epitaxy: Van der Waals epitaxy; a growth method relying on weak van der Waals forces.

Appendix B: Characterization Techniques

Raman spectroscopy analyzes material structure and defects, using the G-band (~1580 cm^{-1}) and 2D-band (~2700 cm^{-1}) for graphene, and the E_2g mode (~1370 cm^{-1}) for h-BN.

Atomic force microscopy (AFM) provides nanometer-resolution surface topography, layer thickness measurement, and surface roughness (RMS) analysis.

X-ray diffraction (XRD) enables crystal structure analysis, lattice parameter determination, and crystal quality evaluation.

Transmission electron microscopy (TEM) offers atomic-resolution imaging, interface structure analysis, and crystallographic orientation determination.

Photoluminescence (PL) spectroscopy characterizes optical properties, measures bandgap, and detects defect states.

Hall effect measurements determine electron mobility, carrier concentration, and resistivity characterization.

Appendix C: Symbols and Abbreviations

Symbol/Abbreviation	Full Name	Unit
f_T	Cutoff frequency	GHz
f_{max}	Maximum oscillation frequency	GHz
I_{DS}	Drain-source current	A or mA/mm
V_{DS}	Drain-source voltage	V
V_{GS}	Gate-source voltage	V
V_{TH}	Threshold voltage	V
V_{BR}	Breakdown voltage	V
g_m	Transconductance	mS/mm
R_{on}	On-state resistance	Ω·mm
R_C	Contact resistance	Ω·mm or mΩ·cm²
μ	Electron mobility	cm²/V·s
n_s	Sheet carrier concentration	cm⁻²
k	Thermal conductivity	W/m·K
R_{th}	Thermal resistance	K/W or °C/W
PAE	Power Added Efficiency	%
η	Quantum efficiency	%

Appendix D: Acknowledgments

This comprehensive review study was made possible by the contributions of all researchers working in the field of GaN HEMT technology and 2D materials. We especially thank all authors who published their original experimental work and shared their knowledge with the academic community.